

**DESIGN AND PERFORMANCE ANALYSIS OF A REVERSIBLE AXIAL  
FLOW FAN**

**A THESIS SUBMITTED TO  
THE GRADUATE SCHOOL OF NATURAL AND APPLIED SCIENCES  
OF  
MIDDLE EAST TECHNICAL UNIVERSITY**

**BY  
TOLGA KÖKTÜRK**

**IN PARTIAL FULFILLMENT OF THE REQUIREMENTS FOR  
THE DEGREE OF MASTER OF SCIENCE**

**IN  
MECHANICAL ENGINEERING**

**JUNE 2005**

Approval of the Graduate School of Natural and Applied Sciences

---

Prof.Dr. Canan ÖZGEN

Director

I certify that this thesis satisfies all the requirements as a thesis for the degree of Master of Science.

---

Prof.Dr. Kemal İDER

Head of Department

This is to certify that we have read this thesis and that in our opinion it is fully adequate, in scope and quality, as a thesis for the degree of Master of Science.

---

Prof.Dr. O.Cahit ERALP

Supervisor

Examining Committee Members

Prof.Dr. Demir BAYKA

(METU,ME)

---

Prof.Dr. O.Cahit ERALP

(METU,ME)

---

Prof.Dr. Kahraman ALBAYRAK

(METU,ME)

---

Instr. Dr. Tahsin ÇETİNKAYA

(METU,ME)

---

M.S. Onur KONURALP

(Layne Bowler)

---

**I hereby declare that all information in this document has been obtained and presented in accordance with academic rules and ethical conduct. I also declare that, as required by these rules and conduct, I have fully cited and referenced all material and results that are not original to this work.**

Tolga KÖKTÜRK

Signature :

## **ABSTRACT**

### **DESIGN AND PERFORMANCE ANALYSIS OF A REVERSIBLE AXIAL FLOW FAN**

Köktürk, Tolga

M.S., Department of Mechanical Engineering

Supervisor: Prof.Dr. O.Cahit ERALP

June 2005, 143 pages

Reversible axial flow fans are used as emergency ventilation fans to discharge the smoke generated on the probable fires occurring in the underground transportation systems and mines as quickly as possible, without causing any harm to people exposed to it. The fans which are placed in different configurations according to the location of fire must be able to work bi-directionally, namely reversible. Due to this fact, the blade profiles of the fan must possess the same aerodynamic performance while working on either discharge or suction condition of the fan, dictated by direction of the rotation.

This manuscript consists of the computation of the aerodynamic performances of symmetrical blade profiles of fully reversible axial fans by computational fluid mechanics (CFD) methods, developing a methodology for the design of reversible axial fans and analysis of the designed fan with CFD methods. The aerodynamic performances of the blade cascades are evaluated using FLUENT 6.0 software for different Reynolds numbers, solidities and angle of attacks of the cascade. The

results of these computations are embedded into the developed methodology. Performance analysis of the reversible axial flow fan, which is designed with the developed methodology, is done with CFD techniques.

Keywords: Reversible Axial Flow Fan, Computational Fluid Dynamics, aerodynamic performance of blade cascades.

## ÖZ

### TERSİNİR EKSENEL FANLARIN TASARIMI VE PERFORMANS ANALİZİ

Köktürk, Tolga

Yüksek Lisans, Makina Mühendisliği Bölümü

Tez Yöneticisi : Prof.Dr. O.Cahit ERALP

Haziran 2005, 143 sayfa

Tersinir eksenel fanlar, acil durum havalandırma fanları olarak yeraltı toplu taşıma sistemlerinde, madenlerde meydana gelebilecek olası yangınlarda oluşacak dumanı en kısa sürede, insanlara zarar vermeden tahliye edebilmek için kullanılır. Çeşitli konfigürasyonlarda yerleştirilen fanlar duman pozisyonuna göre iki taraflı (tersinir) çalışabilmelidir. Bunun için fanların kanat kesitleri fanın dönüş yönüne göre emme veya basma çalışma durumunda aynı aerodinamik özellikleri göstermelidir.

Bu çalışma, tam tersinir çalışabilen acil durum havalandırma fanları için kullanılabilen tam simetrik, elips kanat profillerinin aerodinamik özelliklerinin hesaplamalı akışkanlar dinamiği ile çözümlenmesi, tersinir eksenel fanların tasarımı üzerine bir metot geliştirilmesi ve geliştirilen metoda göre tasarlanan fanın hesaplamalı akışkanlar dinamiği kullanarak analizi üzerinedir. Kanat profillerinin aerodinamik performansı için çeşitli Reynolds sayıları, kanat sıklıkları ve hücum açılarında yerleştirilmiş kanat dizini üzerinde FLUENT yazılımı kullanılarak çözüm elde edilmektedir. Tam simetrik elips profiller için yapılan bu çözümün sonuçları

tersinir eksenel fanların aerodinamik tasarımında geliştirilen metot içerisinde kullanılmaktadır. Geliştirilen metot ile belirli bir çalışma noktası için tasarlanan tersinir eksenel fanın performans analizi hesaplamalı akışkanlar dinamiği ile yapılmıştır.

Anahtar Kelimeler: Tersinir Eksenel Fan, Hesaplamalı Akışkanlar Dinamiği, kanat dizinlerinin aerodinamik performansı.

*To my family and people who love me*

## **ACKNOWLEDGMENTS**

The author wishes to express his deepest gratitude to his supervisor, Prof. Dr. O. Cahit ERALP, for his guidance, advice, criticism, encouragement and insight throughout the research.

The author also would like to thank his precious family for their endless love, dear friends, Nur Seda Köktürk, Çağrı Murat Karapıçak and Yoldaş Ataseven for their invaluable support, Serkan Kayılı, Eren Musluoğlu, Ekin Özgirgin Bingöl, Ertuğrul Şencan and Gençer Koç for their valuable suggestions and comments.

The assistance of Emre Öztürk is gratefully acknowledged for his technical support on FLUENT 6.0.

## TABLE OF CONTENTS

ABSTRACT .....	iv
ÖZ .....	vi
ACKNOWLEDGMENTS .....	ix
TABLE OF CONTENTS .....	x
LIST OF TABLES .....	xiii
LIST OF FIGURES .....	xv
LIST OF SYMBOLS .....	xviii
CHAPTERS	
1. INTRODUCTION.....	1
1.1. General .....	1
1.2. The Background and Literature Survey .....	2
1.2.1. Computational Fluid Dynamics .....	2
1.2.1.1. Mathematical Model .....	3
1.2.1.2. Discretization Method.....	4
1.2.1.3. Coordinate System .....	4
1.2.1.4. Numerical Grid .....	4
1.2.1.5. Finite Approximations .....	6
1.2.1.6. Solution Method.....	6
1.2.1.7. Convergence Criteria .....	7
1.2.2. Turbulence Modeling.....	7
1.2.2.1. Methodology and Governing Terminology .....	7
1.2.2.2. The Turbulence Intensity and Turbulence Kinetic Energy .....	10
1.2.2.3. One-Equation Models .....	13
1.2.2.3.1. Spalart-Allmaras One Equation Model.....	14
1.2.2.4. Two-Equation Models.....	16

1.2.2.4.1.	Standard k- $\epsilon$ Model .....	17
1.2.2.4.2.	RNG (Renormalization Group) k- $\epsilon$ Model .....	19
1.2.3.	CFD Analysis of Airfoils and Blade Cascades .....	22
1.2.4.	CFD Analysis of Turbomachinery .....	28
1.2.5.	Axial Flow Fans .....	33
1.2.5.1.	Axial Flow Fan Types .....	34
1.2.5.2.	Performance of Axial Flow Fans .....	38
1.3.	Overview of the FLUENT CFD Program .....	40
1.3.1.	Introduction .....	40
1.3.2.	Program Structure .....	41
1.3.3.	Program and Modeling Capabilities .....	42
1.3.4.	Boundary Conditions .....	43
1.3.4.1.	Flow Inlet/Exit Boundary Conditions .....	44
1.3.4.2.	Wall Boundary Conditions .....	45
1.3.4.3.	Symmetry Boundary Conditions .....	45
1.3.4.4.	Periodic Boundary Conditions .....	45
1.3.5.	Numerical Schemes .....	47
1.3.6.	Solution Adaptive Grid .....	48
2.	AERODYNAMIC PERFORMANCE ANALYSIS OF BLADE CASCADES ....	51
2.1.	The Blade Profile .....	51
2.2.	Calculation of Aerodynamic Parameters .....	52
2.3.	Computational Mesh and Boundary Conditions .....	55
2.4.	Solution of the Blade Cascades .....	62
3.	AERODYNAMIC DESIGN OF THE REVERSIBLE AXIAL FLOW FAN .....	74
3.1.	Introduction .....	74
3.2.	Selection of Outer Diameter .....	75
3.3.	Design Basis and Assumptions .....	77
3.4.	Design Procedure .....	78
3.5.	Sample Design .....	84
4.	PERFORMANCE ANALYSIS OF THE REVERSIBLE AXIAL FAN .....	89
4.1.	Introduction .....	89
4.2.	Computational Mesh .....	90

4.3.	Boundary Conditions .....	91
4.4.	Solution of the Aerodynamic Performance of the Fan.....	95
4.4.1.	Turbulence Model and Solution Controls .....	95
4.4.2.	Iteration Results .....	97
4.4.2.1.	Iteration Results for Design Rotational Speed.....	98
4.4.2.2.	Iteration Results for the Increased Rotational Speed .....	113
4.4.2.2.1.	Fan Similitude Analysis .....	113
4.4.2.2.2.	The Comparison of the Results .....	115
5.	DISCUSSION OF THE RESULTS AND CONCLUSION .....	118
5.1.	General .....	118
5.2.	Aerodynamic Performance of Blade Cascades .....	118
5.3.	Reversible Axial Fan Design .....	119
5.4.	Performance Analysis of the Reversible Axial Fan .....	120
5.5.	Recommendations for Future Work.....	121
	REFERENCES.....	122
	APPENDICES	
A.	DESIGN FOR HUB AND TIP RADII .....	126
A.1.	Hub Radius Design ( $\sigma=1$ ) .....	126
A.2.	Tip Radius Design ( $\sigma=0.2$ ).....	129
B.	RESULTS FOR BLADE PERFORMANCE ANALYSIS .....	133
B.1.	Solidity $\sigma=0.1$ .....	133
B.2.	Solidity $\sigma=0.2$ .....	135
B.3.	Solidity $\sigma=0.5$ .....	136
B.4.	Solidity $\sigma=1$ .....	138
B.5.	Solidity $\sigma=1.5$ .....	140
B.6.	Solidity $\sigma=2$ .....	141

## LIST OF TABLES

Table 2.1:	Aerodynamic coefficients in X-Y directions and their reduction to mean velocity direction .....	70
Table 3.1:	Blading Efficiencies for Different Solidities.....	87
Table 3.2:	Design Summary .....	87
Table 4.1:	Computed Performance Points for the Fan (N=1000 rpm).....	98
Table 4.2:	Data for increased rotational speed analysis .....	116
Table B1.1:	Aerodynamic Performance for V=10m/s, $\sigma=0.1$ .....	133
Table B1.2:	Aerodynamic Performance for V=30m/s, $\sigma=0.1$ .....	133
Table B1.3:	Aerodynamic Performance for V=50m/s, $\sigma=0.1$ .....	134
Table B1.4:	Aerodynamic Performance for V=70m/s, $\sigma=0.1$ .....	134
Table B1.5:	Aerodynamic Performance for V=100m/s, $\sigma=0.1$ .....	134
Table B2.1:	Aerodynamic Performance for V=10m/s, $\sigma=0.2$ .....	135
Table B2.2:	Aerodynamic Performance for V=30m/s, $\sigma=0.2$ .....	135
Table B2.3:	Aerodynamic Performance for V=50m/s, $\sigma=0.2$ .....	135
Table B2.4:	Aerodynamic Performance for V=70m/s, $\sigma=0.2$ .....	136
Table B2.5:	Aerodynamic Performance for V=100m/s, $\sigma=0.2$ .....	136
Table B3.1:	Aerodynamic Performance for V=10m/s, $\sigma=0.5$ .....	136
Table B3.2:	Aerodynamic Performance for V=30m/s, $\sigma=0.5$ .....	137
Table B3.3:	Aerodynamic Performance for V=50m/s, $\sigma=0.5$ .....	137
Table B3.4:	Aerodynamic Performance for V=70m/s, $\sigma=0.5$ .....	137
Table B3.5:	Aerodynamic Performance for V=100m/s, $\sigma=0.5$ .....	138
Table B4.1:	Aerodynamic Performance for V=10m/s, $\sigma=1$ .....	138
Table B4.2:	Aerodynamic Performance for V=30m/s, $\sigma=1$ .....	138
Table B4.3:	Aerodynamic Performance for V=50m/s, $\sigma=1$ .....	139
Table B4.4:	Aerodynamic Performance for V=70m/s, $\sigma=1$ .....	139

Table B4.5:	Aerodynamic Performance for $V=100\text{m/s}$ , $\sigma=1$ .....	139
Table B5.1:	Aerodynamic Performance for $V=10\text{m/s}$ , $\sigma=1.5$ .....	140
Table B5.2:	Aerodynamic Performance for $V=30\text{m/s}$ , $\sigma=1.5$ .....	140
Table B5.3:	Aerodynamic Performance for $V=50\text{m/s}$ , $\sigma=1.5$ .....	140
Table B5.4:	Aerodynamic Performance for $V=70\text{m/s}$ , $\sigma=1.5$ .....	141
Table B5.5:	Aerodynamic Performance for $V=100\text{m/s}$ , $\sigma=1.5$ .....	141
Table B6.1:	Aerodynamic Performance for $V=10\text{m/s}$ , $\sigma=2$ .....	141
Table B6.2:	Aerodynamic Performance for $V=30\text{m/s}$ , $\sigma=2$ .....	142
Table B6.3:	Aerodynamic Performance for $V=50\text{m/s}$ , $\sigma=2$ .....	142
Table B6.4:	Aerodynamic Performance for $V=70\text{m/s}$ , $\sigma=2$ .....	142
Table B6.5:	Aerodynamic Performance for $V=100\text{m/s}$ , $\sigma=2$ .....	143

## LIST OF FIGURES

Figure 1.1:	An example of structured grid for 2D solution of temperature distribution in a room [2].	5
Figure 1.2:	Unstructured grid generated around a RAE 2822 airfoil [10].	6
Figure 1.3:	Propeller fan with direct drive.	35
Figure 1.4:	Propeller fan with belt drive.	35
Figure 1.5:	Tube-axial fan	36
Figure 1.6:	Vaneaxial fan	37
Figure 1.7:	Two-stage axial flow fan.	38
Figure 1.8:	Static Pressure vs. Volume flowrate of an axial fan [24].	39
Figure 1.9:	Effect of different flow conditions on axial fan performance [26].	39
Figure 1.10:	Basic Program Structure [2].	41
Figure 1.11:	Rotationally periodic boundary conditions, swirling flow in a cylindrical vessel [2].	46
Figure 1.12:	Translationally periodic boundary conditions [2].	47
Figure 2.1:	Linear blade cascade and velocity triangles.	52
Figure 2.2:	The forces on a stationary blade cascade	53
Figure 2.3:	Computational mesh around the elliptical blade profile for $\sigma = 0.5$ solidity and $25^\circ$ angle of attack.	55
Figure 2.4:	The boundary conditions (B.C.'s) of the computation.	56
Figure 2.5:	Velocity inlet B.C. panel in Fluent 6.0.	57
Figure 2.6:	Pressure outlet B.C. in Fluent 6.0.	57
Figure 2.7:	Periodic interfaces, periodic zone and three periodic repeat of the solution domain.	58
Figure 2.8 (a):	The solution domain for $\sigma = 0.1$ , $i=10^\circ$	59
Figure 2.8 (b):	The solution domain for $\sigma = 0.2$ , $i=10^\circ$	60

Figure 2.8 (c):	The solution domain for $\sigma = 1, i=10^\circ$ .....	60
Figure 2.8 (d):	The solution domain for $\sigma = 1.5, i=10^\circ$ .....	61
Figure 2.8 (e):	The solution domain for $\sigma = 2, i=10^\circ$ .....	61
Figure 2.9:	Convergence history graph for $\sigma= 1.5, i = 10^\circ$ for 30m/s velocity. ...	63
Figure 2.10:	The coordinate axes and the measuring section one chord length away from the cascade. ....	64
Figure 2.11:	Velocities in x direction at one chord downstream. ....	64
Figure 2.12:	Total pressure distribution ( $\sigma = 0.5, i = 20^\circ, V = 70 \text{ m/s}$ ).....	65
Figure 2.13:	Contours of stream function ( $\sigma = 0.5, i = 20^\circ, V = 70 \text{ m/s}$ ).....	65
Figure 2.14:	Velocity vectors of the overall field ( $\sigma = 1.5, i=30^\circ, V=70 \text{ m/s}$ ).....	66
Figure 2.15:	Detail of velocity vectors at leading edge ( $\sigma = 1.5, i=30^\circ, V=70 \text{ m/s}$ ).66	
Figure 2.16:	Velocity vectors of the overall field ( $\sigma = 0.1, i=30^\circ, V=70 \text{ m/s}$ ).....	67
Figure 2.17:	Detail of velocity vectors at leading edge ( $\sigma = 0.1, i=30^\circ, V=70 \text{ m/s}$ ).67	
Figure 2.18:	Static pressure distribution on the blades with $\sigma = 1.5$ .....	68
Figure 2.19:	Static pressure distribution on the blades with $\sigma = 0.1$ .....	69
Figure 2.20:	Lift coefficient vs. angle of attack at different solidities ( $V=70\text{m/s}$ ). ..	71
Figure 2.21:	Drag coefficient vs. angle of attack at different solidities ( $V=70 \text{ m/s}$ ).72	
Figure 2.22:	L/D vs. angle of attack at different solidities ( $V=70 \text{ m/s}$ ). ....	73
Figure 3.1:	Optimum curves with minimal hub ratios for different methods of installation for impellers with low characteristics [26]. ....	76
Figure 3.2:	Fan configuration giving definitions of diameters and reference planes.....	77
Figure 3.3:	Flow triangles on the rotor.....	81
Figure 3.4:	Schematic view of the blade settings at three radial positions.....	88
Figure 4.1:	Computational mesh of the solution domain.....	90
Figure 4.2:	Computational mesh with seven periodic repeats.....	91
Figure 4.3:	Fan Boundary Conditions (1).....	92
Figure 4.4:	Fan Boundary Conditions (2).....	92
Figure 4.5:	Pressure inlet boundary condition panel.....	93
Figure 4.6:	Pressure outlet boundary condition panel.....	94
Figure 4.7:	Boundary condition panel for the fluid zone.....	95
Figure 4.8:	Viscous Model Form in FLUENT. ....	96

Figure 4.9:	Solution Control Panel .....	97
Figure 4.10:	Fan Performance Curve (N=1000 rpm) .....	99
Figure 4.11(a):	Total pressure contours on the suction side of the blade .....	100
Figure 4.11(b):	Total pressure contours on the pressure side of the blade.....	101
Figure 4.12:	Total pressures at the outlet section along radial direction.....	101
Figure 4.13:	The total pressures along meridional direction at the mid height from hub to casing.....	102
Figure 4.14:	Circumferentially averaged total pressures in the domain.....	102
Figure 4.15:	Planes that cut the blades in flow and tangential directions.....	103
Figure 4.16:	Contours of X direction velocity in Plane 1 .....	104
Figure 4.17:	Several operating points.....	105
Figure 4.18(a):	Pathlines at mid-span for operating point (A).....	105
Figure 4.18(b):	Pathlines at mid-span for operating point (B).....	106
Figure 4.18(c):	Pathlines at mid-span for operating point (C).....	106
Figure 4.18(d):	Pathlines at mid-span for operating point (D).....	107
Figure 4.18(e):	Pathlines at mid-span for operating point (E) .....	107
Figure 4.18(f):	Pathlines at mid-span for operating point (F) .....	108
Figure 4.19(a):	Path lines on the hub at design point (B) .....	109
Figure 4.19(b):	Path lines on the hub at operating point (D) .....	109
Figure 4.19(c):	Path lines on the hub at operating point (F).....	110
Figure 4.20:	Vortex formation at the tip of the blade for operating point (D). ....	110
Figure 4.21:	Smooth airflow at the design point (B).....	111
Figure 4.22:	Contours of velocity magnitude at operating point (B) .....	111
Figure 4.23:	Contours of velocity magnitude at operating point (F).....	112
Figure 4.24:	Velocity vectors at operating point (B).....	112
Figure 4.25:	Velocity vectors at operating point (F). .....	113
Figure 4.26:	Fan performance curves for increased rotational speed.....	116

## LIST OF SYMBOLS

$\rho$	: Density ( $\text{kg/m}^3$ )
$p$	: Pressure (Pa)
$\mu$	: Dynamic viscosity (Pa.s)
$g$	: Gravitational acceleration ( $\text{m/s}^2$ )
$u$	: Velocity, rotational speed (m/s)
$S_{ij}$	: Strain rate tensor ( $\text{s}^{-1}$ )
$\tau_{ij}$	: Reynolds stress tensor (Pa)
$\varepsilon_{ij}$	: Turbulence kinetic energy dissipation
$k$	: Turbulence kinetic energy ( $\text{m}^2/\text{s}^2$ )
$\nu$	: Kinematic viscosity ( $\text{m}^2/\text{s}$ )
$\nu_T$	: Kinematic eddy viscosity ( $\text{m}^2/\text{s}$ )
$\Omega_{ij}$	: Rotation tensor ( $\text{s}^{-1}$ )
$G$	: Generation term
$S$	: Source term
$Pr$	: Prandtl number
$Pr_t$	: Turbulent Prandtl number
$Re$	: Reynolds number
$\alpha_{k,\varepsilon}$	: Inverse effective Prandtl number
$V$	: Absolute velocity (m/s)
$W$	: Relative velocity (m/s)
$\beta$	: Relative fluid angle ( $^\circ$ )
$\beta_k$	: Relative blade angle ( $^\circ$ )
$\zeta$	: Stagger Angle ( $^\circ$ )
$c$	: Blade chord (m)
$s$	: Blade spacing (m)

$t$	: Blade thickness (mm)
$\delta$	: Deviation angle ( $^{\circ}$ )
$i$	: Incidence angle ( $^{\circ}$ )
$\sigma$	: Solidity
$L$	: Lift force (N)
$D$	: Drag force (N)
$C_L$	: Lift coefficient
$C_D$	: Total drag coefficient
$C_{DP}$	: Profile drag coefficient
$C_{DS}$	: Secondary loss coefficient
$C_{DA}$	: Annulus drag coefficient
$A_p$	: Projected wing area ( $m^2$ )
$Q$	: Volumetric flowrate ( $m^3/s$ )
$H$	: Head (m)
$N$	: Rotational speed (rpm)
$P$	: Power (W)
$N_s$	: Specific speed
$N_D$	: Specific Diameter
$\Psi_{th}$	: Theoretical head rise coefficient
$\Psi_R$	: Rotor loss coefficient
$D$	: Diameter
$\psi$	: Blade loading coefficient
$\phi$	: Flow coefficient
$\varepsilon$	: Swirl coefficient
$\eta_{BL}$	: Blade Efficiency
$\eta$	: Hydraulic efficiency

### Subscripts

$a$	: Axial component
$\theta$	: Tangential component
$1$	: Rotor inlet

- 2 : Rotor outlet
- $\infty$  : Mean velocity component

## CHAPTER 1

### INTRODUCTION

#### 1.1. General

The first precaution that should be taken on probable fire incidences in underground transportation systems and mines is to discharge the generated smoke without giving harm to people who are exposed to it. To achieve this goal, fans that are placed on specific locations in the underground tunnels direct the smoke to exhaust shafts of the tunnels according to the location of the fire and the evacuation routes of the passengers. What is important in the selection and design of these fans in these applications is that the fans must possess the same performance in supply and exhaust working modes and supply the required air velocity/flowrate to guide the smoke to proper directions. That is why the fans to be used in emergency ventilation applications should be axial and reversible.

Reversible fans are capable of working with the same performance when their direction of rotation is reversed. In such an application, the blade profiles of the fan must be fully symmetrical. Reversing the direction of rotation, leading edge of the blade behaves as trailing edge, and trailing edge behaves as the leading edge. Similarly, the pressure sides of the blades become the suction sides and the suction sides become the pressure sides. To satisfy the condition, the blade must have no camber. For this specific application, elliptical profiles are used.

The aerodynamic performances of blade cascades of elliptical profiles are obtained via computational fluid dynamics techniques for different Reynolds numbers, blade

solidities and angles of attack. The cascades of infinite number of blades are modeled in Gambit 2.0, a program that enables the user to form the problem and mesh the domain for the solution, and solved for their aerodynamic performances with FLUENT 6.0, software for CFD applications.

These aerodynamic performance parameters are used in the design phase of the fan. In the adapted design for the reversible axial flow fans, the flow at the inlet section of the fan is assumed to have no radial velocity component and the head rise is constant in radial direction (free vortex design). Due to the free vortex design condition, no pressure difference occurs across the streamlines at the exit of the fan in radial direction, so the streamlines are only composed of axial and tangential components. Being aware of the fact, the aerodynamic performances of the blade cascades are computed in two-dimensional solution domain. Because the blades of the axial turbomachines behave as infinitely long linear blade cascades, the aerodynamic performance solution is performed on a cascade having infinite number of blades. The solutions for single blade analysis are not performed because the interactions between the blades are the determining factors for the aerodynamic performance of the fans; cascade solution is thought to be a better choice.

The design parameters of the fan are taken from typical fans that are used as the emergency ventilation fans in underground transportation systems. The performed design is modeled in Gambit 2.0 and solved in FLUENT 6.0, for the consistence of the design point with the analysis.

## **1.2. The Background and Literature Survey**

### **1.2.1. Computational Fluid Dynamics**

In the cases where the experimental techniques for the problems are not appropriate to be applied, the engineers use the CFD tools to obtain information about the fluid flow problems and the flow parameters like pressure, velocity and temperature. If the

engineer cannot perform experiments, then he has to solve the basic equations to solve the phenomena, i.e. conservation equations of mass and momentum for pressure and velocity, energy equation for the temperature. The solution of these unknown variables needs an order to be followed, which the area of CFD plays its role. Computational Fluid Dynamics (CFD) deals with the numerical solution of a set of differential equations defining a fluid flow and related phenomena to obtain specific information of the flow field. Although the area is still developing and new techniques are emerging, satisfactory results are obtained to engineering problems. From the beginning till the end, a description of the phases that are followed in the solution of required unknowns via CFD is given by reference [1] which will be discussed here briefly.

#### 1.2.1.1. Mathematical Model

The starting point of any numerical method is the mathematical model, i.e. the set of partial differential equations and boundary conditions. The sets of equations are chosen for target application (inviscid, incompressible, turbulent, two or three dimensional) i.e. the continuity equation and the Navier-Stokes equations are needed to obtain the pressure and velocity around the flow field. For incompressible flow, the related equations are as follows:

Using tensor notation in Cartesian coordinates, continuity equation is

$$\frac{\partial u_i}{\partial x_i} = S_m \dots\dots\dots(1)$$

$S_m$  is source term and is set to 0 if there is no mass added to the continuous phase from dispersed second phase (e.g., due to vaporization of liquid droplets) or any source defined by the user.

Conservation of momentum (Navier-Stokes Equations) for incompressible flow is

$$\rho \frac{\partial u_i}{\partial t} + \rho \frac{\partial (u_j u_i)}{\partial x_j} = -\frac{\partial p}{\partial x_i} + \frac{\partial}{\partial x_j} (2\mu s_{ij}) + \rho g_i + F_i \dots\dots\dots(2)$$

where  $F_i$  is external body force and  $s_{ij}$  is the stress tensor which is given by

$$s_{ij} = \frac{1}{2} \left( \frac{\partial u_i}{\partial x_j} + \frac{\partial u_j}{\partial x_i} \right) \dots\dots\dots(3)$$

**1.2.1.2. Discretization Method**

The second step is to approximate the differential equations by a system of algebraic equations for the variables at some set of discrete locations in space and time. Most important discretization methods are finite difference (FD), finite volume (FV) and finite element (FE) methods all of which yield the same solution if the computational domain is very fine.

**1.2.1.3. Coordinate System**

Because the conservation equations can be written in many different forms, depending on the coordinate system, one must select his coordinate system, Cartesian, cylindrical, spherical, curvilinear systems, which may be fixed or moving.

**1.2.1.4. Numerical Grid**

The discrete locations at which the variables are to be calculated are defined by the numerical grid which is essentially a discrete representation of the geometric domain on which the problem is to be solved. It divides the solution domain into a finite number of subdomains (elements, control volumes etc.). Most common options are as follows:

- Structured (regular) Grid: This is the simplest grid structure, since it is logically equivalent to a Cartesian grid. Each point has four nearest neighbors in two dimension and six in three dimensions. An example of the grid structure is given in Figure 1.1. The neighbor connectivity simplifies programming and the matrix of the algebraic equation system has a regular structure. The disadvantage of structured grids is that, they can be used only for geometrically simple solution domains. Another disadvantage is that it may be difficult to control the distribution of the grid points: concentration of points in one region for reasons of accuracy produces unnecessarily small spacing in other parts of the solution domain and waste of resources.

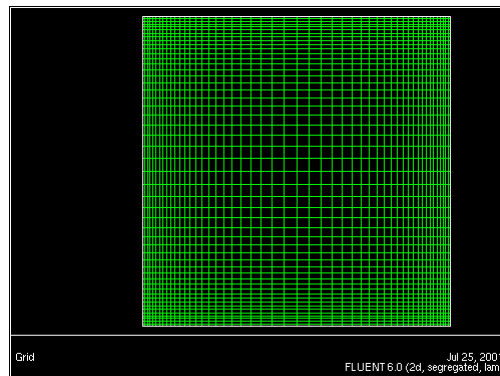


**Figure 1.1:** An example of structured grid for 2D solution of temperature distribution in a room [2].

- Unstructured Grid: For very complex geometries, the most flexible type of grid is one that can fit arbitrary solution domain boundary. In principle, such grids are applicable to any discretization scheme, but they are best adapted to the finite volume and finite element approaches. The elements or control volumes may have any shape; nor is there a restriction on the number of neighbor elements or nodes. In practice, grids made of triangles or quadrilaterals in 2d, and tetrahedral or hexahedral in 3d are most often used. An example of unstructured grid is given in Figure 1.2.

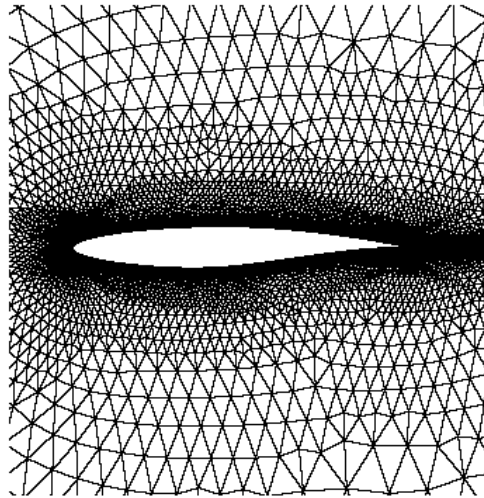


**Figure 1.2:** Unstructured grid generated around a RAE 2822 airfoil [10].

#### **1.2.1.5. Finite Approximations**

Following the choice of grid type, one has to select the approximations to be used in discretization process. In a finite difference method, approximations for the derivatives at the grid points have to be selected. In a finite volume method, one has to select the methods of approximating surface and volume integrals. In a finite element method, one has to choose the functions and weighting functions.

#### **1.2.1.6. Solution Method**

Discretization yields a large system of non-linear algebraic equations. The method of solution depends on the problem. Steady problems are usually solved by iteration schemes. These methods use successive linearization of the equations and the resulting linear systems are almost always solved by iterative techniques.

### 1.2.1.7. Convergence Criteria

Finally, one needs to set the convergence criteria for the iterative method. When using iterative solvers, it is important to know when to quit. The most common procedure is based on the difference between two successive iterates or residuals; the procedure is stopped when this difference, measured by some norm, is less than a pre-selected value. Many iterative solvers require calculation of the residual. The norm of residual prior to the first iteration provides a reference for checking the convergence of iterations (usually by three or four orders of magnitude).

## 1.2.2. Turbulence Modeling

### 1.2.2.1. Methodology and Governing Terminology

Because the aim of the manuscript is to analyze the aerodynamic characteristics of the blade sections and check the appropriateness of the developed design methodology for the axial flow fans, it is better to give brief information on the turbulence and the turbulence models that will be adapted to the analysis.

By definition, *“Turbulent fluid motion is an irregular condition of flow in which the various quantities show a random variation with time and space coordinates, so that statistically distinct average values can be discerned”* [3]. Because the turbulence consists of random fluctuations of the various properties, statistical approaches are used to express mean and fluctuating parts. Chen, C.J, and Jaw, S.Y. [4] summarized that from an engineering point of view, what an engineer would like to know is the mean effect of turbulence quantities and not so much the instantaneous fluctuation quantities. Thus, a more practical engineering approach to describe turbulent flow is to model the averaged turbulence quantities. When taking the ensemble average of the instantaneous Navier-Stokes equations, additional terms known as the Reynolds stress  $\overline{u_i u_j}$  appear in the averaged Navier-Stokes equations,

which makes the number of unknowns larger than the available equations. To close the problem, the Reynolds stresses have to be modeled, and additional differential equations related to turbulence characteristics may have to be introduced.

Summarizing the study of Wilcox, D.J. [5], the Reynolds-Averaged equations are

$$\frac{\partial U_i}{\partial x_i} = 0 \dots\dots\dots(4)$$

$$\rho \frac{\partial U_i}{\partial t} + \rho \frac{\partial}{\partial x_j} (U_j U_i + \overline{u_j' u_i'}) = -\frac{\partial P}{\partial x_i} + \frac{\partial}{\partial x_j} (2\mu S_{ji}) \dots\dots\dots(5)$$

where  $\mu$  is the dynamic viscosity,  $U$  is the mean velocity component,  $u'$  is the fluctuating velocity component which is related to instantaneous velocity ( $u_i$ ) as

$$u_i = U_i + u_i' \dots\dots\dots(6)$$

$S_{ij}$  is the strain rate tensor and is given by equation (3)

Aside from replacement of instantaneous variables by mean values, the only difference between the time averaged and instantaneous equations (equations (2) and (5)), except the body forces, is the appearance of the correlation  $\overline{u_i' u_j'}$ . This is a time-averaged rate of momentum transfer due to the turbulence. Herein lies the **fundamental problem of turbulence** [5]. In order to compute all mean flow properties of the turbulent flow under consideration, we need a prescription for computing  $\overline{u_i' u_j'}$ .

Here, the concept of specific Reynolds stress tensor is introduced as follows

$$\tau_{ij} = -\overline{u_i' u_j'} \dots\dots\dots(7)$$

$\tau_{ij}$  is a symmetric tensor, thus has six independent components. Hence, six unknown quantities are produced as a result of Reynolds averaging. Along with pressure and

three velocity components for general three-dimensional flows, total number of unknowns becomes ten but four equations are present (conservation of mass and momentum in three directions). The requirement for additional stress components are obtained from taking moments of Navier-Stokes (N-S) equations, that is multiplying N-S equation by a fluctuating property and time average the product. Using the procedure, a differential equation for the Reynolds-stress tensor is derived. The procedure will not be given but the resulting Reynolds stress equation for incompressible flow will be introduced:

$$\frac{\partial \tau_{ij}}{\partial t} + U_k \frac{\partial \tau_{ij}}{\partial x_k} = -\tau_{ik} \frac{\partial U_j}{\partial x_k} - \tau_{jk} \frac{\partial U_i}{\partial x_k} + \varepsilon_{ij} + \frac{\partial}{\partial x_k} \left( \nu \frac{\partial \tau_{ij}}{\partial x_k} + C_{ijk} \right) \dots \dots \dots (8)$$

where

$$\varepsilon_{ij} = 2\nu \overline{\frac{\partial u_i'}{\partial x_k} \frac{\partial u_j'}{\partial x_k}} \dots \dots \dots (9)$$

and

$$\rho C_{ijk} = \rho \overline{u_i' u_j' u_k'} + \overline{p' u_i'} \delta_{jk} + \overline{p' u_j'} \delta_{ik} \dots \dots \dots (10)$$

Note that p' is the fluctuating component of pressure.

This procedure also produces new unknowns like  $\overline{u_i' u_j' u_k'}$  and  $(\partial u_i' / \partial x_k)(\partial u_j' / \partial x_k)$ , illustrating the closure problem of turbulence. Because of the non-linearity of N-S equation, as higher and higher moments are taken, new unknowns are generated at each level. There is no way that the number of unknowns and equations can be balanced. The function of turbulence modeling is to establish proper approximations for the unknown correlations in terms of known flow properties so that a sufficient number of equations exists, in other words, to close the system of equations.

Depending on the number of partial differential equations used to describe the turbulent transport quantities, the turbulence models can be classified into four different levels. Jaw, S.Y. and Chen C.J. summarized these levels as follows [4]:

1. The zero equation model, such as mixing length models of Prandtl and Von Karman, uses only the partial differential equation for the mean velocity field. No partial differential equation is used for turbulent transport quantities.
2. The one-equation model, such as Kolmogorov (1942) or Prandtl (1945) uses one partial differential equation to model a turbulence quantity, typically turbulent kinetic energy.
3. The two-equation model, such as k- $\epsilon$  or k- $\omega$  models, uses two partial differential equations to model turbulence quantities, like turbulent kinetic energy and dissipation of turbulent kinetic energy.
4. The second order closure model, also known as the second-moment closure or Reynolds stress closure model, differs from the two-equation model by modeling all turbulent transport quantities, including all components of the turbulent stress tensor,  $\overline{u_i' u_j'}$ , with partial differential equations.

In this part, one equation and two equation models will be described briefly but special attention will be paid on Spalart-Allmaras model in one-equation models and RNG (Renormalization Group) k- $\epsilon$  in two-equation models due to their implementation in the thesis. Before the discussion of these models, it is essential to introduce the Turbulence Kinetic Energy Equation which one equation and two equation models are based on.

#### **1.2.2.2. The Turbulence Intensity and Turbulence Kinetic Energy**

To have an estimate of the velocity scales for the eddies created in turbulent flows, turbulence intensity and turbulence kinetic energy concepts should be introduced.

One of the most important measures of any turbulent flow is how intense the turbulent fluctuations are. This is quantified in terms of specific Reynolds stress components  $\overline{u'^2}$ ,  $\overline{v'^2}$ ,  $\overline{w'^2}$ . These three normal Reynolds stresses can also be regarded as the kinetic energy per unit mass of the fluctuating velocity field in the three coordinate directions. If three normal Reynolds stresses are summed and multiplied by  $1/2$ , **turbulence kinetic energy** ( $k$ ), which is kinetic energy of the turbulent fluctuations per unit mass, is obtained [5]. Thus, by definition,

$$k = \frac{1}{2}(\overline{u'^2} + \overline{v'^2} + \overline{w'^2}) = \frac{1}{2}\overline{u_i' u_i'} \dots\dots\dots(11)$$

It is desirable to note that trace of Reynolds stress tensor gives

$$\tau_{ii} = -2k \dots\dots\dots(12)$$

Like obtaining a differential equation describing the behavior of Reynolds stress tensor (Eq(8)), a similar equation can be obtained for turbulence kinetic energy:

$$\frac{\partial k}{\partial t} + U_j \frac{\partial k}{\partial x_j} = \tau_{ij} \frac{\partial U_i}{\partial x_j} - \varepsilon + \frac{\partial}{\partial x_j} \left( \nu \frac{\partial k}{\partial x_j} - \frac{1}{2} \overline{u_i' u_i' u_j'} - \frac{1}{\rho} \overline{p' u_j'} \right) \dots\dots\dots(13)$$

This equation is known as transport equation for turbulence kinetic energy.  $\varepsilon$  is known as dissipation per unit mass. The sum of the two terms on the left hand side, i.e. the unsteady term and the convection, is the familiar substantial derivative of  $k$  that gives the rate of change of  $k$  following a fluid particle. The first term on the right hand side is known as **production** and represents the rate at which kinetic energy is transferred from the mean flow to the turbulence. **Dissipation** is the rate at which turbulence kinetic energy is converted into thermal energy. The term involving  $\nu(\partial k / \partial x_j)$  is called **molecular diffusion** and represents the diffusion of turbulence energy caused by the fluid's natural molecular transport process. The triple velocity correlation term is referred as **turbulent transport** and regarded as the rate at which

turbulence energy is transported through the fluid by turbulent fluctuations. The last term on the right hand side is **pressure diffusion**.

The unsteady term, convection and molecular diffusion are exact while production, dissipation, turbulent transport and pressure diffusion involve unknown correlations. To close the equation,  $\tau_{ij}$ , dissipation, turbulent transport and pressure diffusion should be specified.

- Reynolds-Stress Tensor: For one and two equation models, it is assumed that Boussinesq approximation is valid and it relates Reynolds stresses to mean velocity gradients, which is

$$\tau_{ij} = 2\nu_T S_{ij} - \frac{2}{3} k \delta_{ij} \dots\dots\dots(14)$$

where  $\nu_T$  is kinematic eddy viscosity and dimensional arguments show that

$$\nu_T = const \times k^{\frac{1}{2}} \times \ell \dots\dots\dots(15)$$

where  $\ell$  is the turbulent length scale, ( $\ell$ ) which is a measure of length where small scaled fluctuations take place in a turbulent flow.

- Turbulent Transport and Pressure Diffusion: Generally, in the absence of definitive experimental data, the pressure-diffusion term is grouped with turbulent transport term and is assumed as

$$\frac{1}{2} \overline{u_i' u_i' u_j'} + \frac{1}{\rho} \overline{p' u_j'} = - \frac{\nu_T}{\sigma_k} \frac{\partial k}{\partial x_j} \dots\dots\dots(16)$$

where  $\sigma_k$  is the closure coefficient.

- Dissipation: The manner in which the dissipation term is determined is not unique amongst turbulence energy equation models. One common way is to

relate the dissipation term to turbulence kinetic energy and a turbulence length scale. The dimensional arguments [6] show that

$$\varepsilon \propto k^{\frac{3}{2}} / \ell \dots\dots\dots(17)$$

When the Eq (13) and (16) are combined, the modeled version of the turbulence kinetic energy equation is obtained in the form which all turbulence energy equation models make use of.

$$\frac{\partial k}{\partial t} + U_j \frac{\partial k}{\partial x_j} = \tau_{ij} \frac{\partial U_i}{\partial x_j} - \varepsilon + \frac{\partial}{\partial x_j} \left[ (\nu + \nu_T / \sigma_k) \frac{\partial k}{\partial x_j} \right] \dots\dots\dots(18)$$

**1.2.2.3. One-Equation Models**

One-equation models involve an equation that relates Reynolds stresses to a turbulence quantity, most generally the turbulence kinetic energy and eddy viscosity. In the models using transport equation for turbulence kinetic energy, the equation (18) is solved along with a prescription of the turbulent length scale and consequently dissipation term. Prandtl introduced a closure coefficient to Eq (17). That is,

$$\varepsilon = C_D k^{\frac{3}{2}} / \ell \dots\dots\dots(19)$$

where  $C_D$  is the closure coefficient. So Prandtl's one-equation model becomes

$$\frac{\partial k}{\partial t} + U_j \frac{\partial k}{\partial x_j} = \tau_{ij} \frac{\partial U_i}{\partial x_j} - C_D \frac{k^{\frac{3}{2}}}{\ell} + \frac{\partial}{\partial x_j} \left[ (\nu + \nu_T / \sigma_k) \frac{\partial k}{\partial x_j} \right] \dots\dots\dots(20)$$

where

$$\nu_T = k^{\frac{1}{2}} \times \ell = C_D k^2 / \varepsilon \dots\dots\dots(21)$$

Note that the constant in Eq (15) is set to one in Eq (21).

After Prandtl, several researchers like Emmons, Glushko applied the model to several flows with closure coefficients  $\sigma_k$ ,  $C_D$  and length scale  $\ell$  set to appropriate values.

In one-equation models, using turbulence kinetic energy is not the unique method to evaluate Reynolds stresses. Another approach is to model a transport equation for kinematic eddy viscosity. Baldwin and Barth (1990), Spalart and Allmaras (1992) developed such models for the evaluation of Reynolds stress tensor. Here, Spalart-Allmaras One Equation model will be introduced because of its implementation in this study.

### 1.2.2.3.1. Spalart-Allmaras One Equation Model

In turbulence models that employ the Boussinesq approach, the central issue is how the eddy viscosity is computed. The model proposed by Spalart and Allmaras solves a transport equation for a quantity that is a modified form of the turbulent kinematic viscosity. The model was designed specifically for aerospace applications involving wall-bounded flows and has been shown to give good results for boundary layers subjected to adverse pressure gradients [2]. This is why the model is selected in the study for the aerodynamic analysis of the blade cascades.

The eddy viscosity equation is given by

$$\frac{\partial \bar{\nu}}{\partial t} + U_j \frac{\partial \bar{\nu}}{\partial x_j} = c_{b1} \bar{S} \bar{\nu} - c_{w1} f_w \left( \frac{\bar{\nu}}{d} \right)^2 + \frac{1}{\sigma} \frac{\partial}{\partial x_k} \left[ (\nu + \bar{\nu}) \frac{\partial \bar{\nu}}{\partial x_k} \right] + \frac{c_{b2}}{\sigma} \frac{\partial \bar{\nu}}{\partial x_k} \frac{\partial \bar{\nu}}{\partial x_k} \dots \dots \dots (22)$$

In Eq. (22), the first term on the right hand side is the production of turbulent viscosity and the second term is the destruction of turbulent viscosity that occurs in

the near wall region due to wall blocking and viscous damping. Note that since the turbulent kinetic energy ( $k$ ) is not calculated in Spalart-Allmaras model, the last term in Eq. (14) is ignored when estimating Reynolds stresses.

The kinematic eddy viscosity ( $\nu_T$ ) is computed from

$$\nu_T = \hat{\nu} \cdot f_{v1} \dots\dots\dots(23)$$

The other closure coefficients and auxiliary relations of the kinematic eddy viscosity equation are as follows:

$$c_{b1} = 0.1355, \quad c_{b2} = 0.622, \quad c_{v1} = 7.1, \quad \sigma = 2/3 \dots\dots\dots(24)$$

$$c_{w1} = \frac{c_{b1}}{\kappa^2} + \frac{(1+c_{b2})}{\sigma}, \quad c_{w2} = 0.3, \quad c_{w3} = 2, \quad \kappa = 2 \dots\dots\dots(25)$$

$$f_{v1} = \frac{\chi^3}{\chi^3 + C_{v1}^3}, \quad f_{v2} = 1 - \frac{\chi}{1 + \chi f_{v1}}, \quad f_w = g \left[ \frac{1 + c_{w3}^6}{g^6 + c_{w3}^6} \right]^{\frac{1}{6}} \dots\dots\dots(26)$$

$$\chi = \frac{\hat{\nu}}{\nu}, \quad g = r + c_{w2}(r^6 - r), \quad r = \frac{\hat{\nu}}{\bar{S} \kappa^2 d^2} \dots\dots\dots(27)$$

$$\hat{S} = S + \frac{\hat{\nu}}{\kappa^2 d^2} f_{v2}, \quad S = \sqrt{2\Omega_{ij}\Omega_{ij}} \dots\dots\dots(28)$$

Here,  $\Omega_{ij}$  is the rotation tensor and is defined as

$$\Omega_{ij} = \frac{1}{2} \left( \frac{\partial U_i}{\partial x_j} - \frac{\partial U_j}{\partial x_i} \right) \dots\dots\dots(29)$$

In the equations,  $d$  is the distance from the closest wall and  $S$  is a scalar measure of deformation tensor, based on the magnitude of vorticity. The model also includes a modification to take the effect of mean strain on turbulent production into account. That is,

$$S = |\Omega_{ij}| + C_{prod} \min(0, |S_{ij}| - |\Omega_{ij}|) \dots \dots \dots (30)$$

$$C_{prod} = 2, \quad |\Omega_{ij}| = \sqrt{2\Omega_{ij}\Omega_{ij}}, \quad |S_{ij}| = \sqrt{2S_{ij}S_{ij}} \dots \dots \dots (31)$$

where  $S_{ij}$  is the mean strain rate tensor and is given by Eq (3).

So, including both the rotation and strain tensors reduces the production of eddy viscosity and consequently reduces the eddy viscosity itself in regions where the measure of vorticity exceeds that of strain rate. One such example can be found in vortical flows, i.e., flow near the core of a vortex subjected to a pure rotation where turbulence is known to be suppressed [2]. Including both the rotation and strain tensors more correctly accounts for the effects of rotation on turbulence. The option including the rotation tensor only tends to overpredict the production of eddy viscosity and hence overpredicts the eddy viscosity itself in certain circumstances.

#### 1.2.2.4. Two-Equation Models

Two equation models of turbulence provide not only computation for turbulence kinetic energy,  $k$ , but also for the turbulence length scale or the equivalent. Consequently, two-equation models can be used to predict properties of a given turbulent flow with no prior knowledge of the turbulent structure, making them as the highlight of the turbulence research during past two decades.

The starting point for virtually all two-equation models is the Boussinesq approximation (Eq 14), and the turbulence kinetic energy equation in the form given by Eq(18). The choice of selecting the second transport equation varies among the

two-equation turbulence models. Most popular of these models are k-ε and k-ω models which model turbulence dissipation rate (ε) and specific dissipation rate (ω), respectively. These models also accommodate different forms inside them allowing them to be more applicable to some flows of various complexities. The k-ε models have three most popularly used forms with changing closure coefficients or the closure functions, namely the Standard k-ε, RNG (Renormalization Group) k-ε, and Realizable k-ε. Similarly, k-ω models have different forms, like Standard and SST (Shear Stress Transport) k-ω models. In this work, Standard k-ε and RNG k-ε models will be introduced as in reference [2]. Although Standard k-ε is not implemented in the work, it will be presented here because it is the basis for the RNG k-ε model, which is the implemented model.

#### 1.2.2.4.1. Standard k-ε Model

As it is mentioned before, the three forms of k-ε models have similar forms for transport equations of k and ε. These models differ in how the turbulent viscosity is calculated, the turbulent Prandtl numbers governing the turbulent diffusion of k and ε and the generation and the destruction terms in ε equation. The Standard k-ε model is as follows:

Transport equation for turbulence kinetic energy

$$\frac{\partial k}{\partial t} + U_j \frac{\partial k}{\partial x_j} = G_k + G_b - \varepsilon + \frac{\partial}{\partial x_j} \left[ (\nu + \nu_T / \sigma_k) \frac{\partial k}{\partial x_j} \right] \dots\dots\dots(32)$$

$G_k$  is the generation of turbulent kinetic energy due to mean velocity gradients and is defined as

$$G_k = -\overline{u_i' u_j'} \frac{\partial u_j}{\partial x_i} \dots\dots\dots(33)$$

To evaluate in a manner consistent with Boussinesq hypothesis,

$$G_k = \nu_T S^2 \dots\dots\dots(34)$$

where S is the modulus of mean rate of strain tensor and is defined as in Eq (31).  
 $G_b$  is the generation of turbulence kinetic energy due to buoyancy and is given by

$$G_b = \beta g_i \frac{\nu_T}{Pr_t} \frac{\partial T}{\partial x_i} \dots\dots\dots(35)$$

where  $Pr_t$  is turbulent Prandtl number and  $g_i$  is the component of gravitational acceleration in the  $i^{th}$  direction and  $\beta$  is the coefficient of thermal expansion. For the standard model, the value of  $Pr_t$  is 0.85 and  $\beta$  is given by

$$\beta = -\frac{1}{\rho} \left( \frac{\partial \rho}{\partial T} \right)_p \dots\dots\dots(36)$$

The transport equation for turbulence dissipation rate ( $\epsilon$ )

$$\frac{\partial \epsilon}{\partial t} + U_i \frac{\partial \epsilon}{\partial x_i} = \frac{\partial}{\partial x_j} \left[ \left( \nu + \frac{\nu_T}{\sigma_\epsilon} \right) \frac{\partial \epsilon}{\partial x_j} \right] + C_{1\epsilon} \frac{\epsilon}{k} (G_k + C_{3\epsilon} G_b) - C_{2\epsilon} \frac{\epsilon^2}{k} \dots\dots\dots(37)$$

The eddy viscosity is computed by combining k and  $\epsilon$  as follows

$$\nu_T = C_\mu \frac{k^2}{\epsilon} \dots\dots\dots(38)$$

and the model constants are

$$C_{1\epsilon}=1.44, \quad C_{2\epsilon}=1.92, \quad C_\mu=0.09, \quad \sigma_k=1.0, \quad \sigma_\epsilon=1.3 \dots\dots\dots(39)$$

The constant  $C_{3\epsilon}$  is the degree to which  $\epsilon$  is affected by buoyancy and is given by

$$C_{3\varepsilon} = \tanh\left|\frac{v}{u}\right| \dots\dots\dots(40)$$

where v is the component of flow velocity parallel to gravitational vector and u is the component of flow velocity perpendicular to gravitational vector.

**1.2.2.4.2. RNG (Renormalization Group) k-ε Model**

The RNG k-ε was derived using a rigorous statistical technique (called renormalization group theory). It is similar to Standard k-ε model but includes following refinements:

- The RNG model has an additional term in its ε equation that significantly improves the accuracy for rapidly strained flows.
- The effect of swirl on turbulence is included in RNG model, enhancing accuracy for swirling flows.
- The RNG theory provides an analytical formula for turbulent Prandtl numbers while the standard k-ε model uses specified constant values.
- While the standard k- ε model is a high Reynolds number model, the RNG theory provides an analytically derived differential formula for effective viscosity that accounts for low Reynolds number effects.

These features make the RNG k-ε model more accurate and reliable for a wider class of flows than the standard k-ε model.

The transport equation for kinetic energy for RNG k-ε is as follows

$$\frac{\partial k}{\partial t} + U_j \frac{\partial k}{\partial x_j} = G_k + G_b - \varepsilon + \frac{\partial}{\partial x_j} \left[ \alpha_k \nu_{eff} \frac{\partial k}{\partial x_j} \right] \dots\dots\dots(41)$$

The transport equation for  $\varepsilon$

$$\frac{\partial \varepsilon}{\partial t} + U_i \frac{\partial \varepsilon}{\partial x_i} = \frac{\partial}{\partial x_j} \left[ \alpha_\varepsilon \nu_{eff} \frac{\partial \varepsilon}{\partial x_j} \right] + C_{1\varepsilon} \frac{\varepsilon}{k} (G_k + C_{3\varepsilon} G_b) - C_{2\varepsilon} \frac{\varepsilon^2}{k} - R_\varepsilon \dots\dots\dots(42)$$

The model constants  $C_{1\varepsilon}$  and  $C_{2\varepsilon}$  have values derived analytically by RNG theory.

$$C_{1\varepsilon} = 1.42, \quad C_{2\varepsilon} = 1.68 \dots\dots\dots(43)$$

In these equations,  $G_k$ ,  $G_b$  and  $C_{3\varepsilon}$  are given by Eq (34), (35) and (40) respectively.  $\nu_{eff}$  is the effective viscosity and is given by

$$d \left( \frac{\rho^2 k}{\sqrt{\varepsilon \mu}} \right) = 1.72 \frac{\hat{\nu}}{\sqrt{\hat{\nu}^3 - 1 + C_\nu}} d\hat{\nu} \dots\dots\dots(45)$$

where

$$\hat{\nu} = \frac{\nu_{eff}}{\nu} \quad \text{and} \quad C_\nu \approx 100 \dots\dots\dots(46)$$

Equation (45) is integrated to obtain an accurate description of how the effective turbulent transport varies with the effective Reynolds number, allowing the model to better handle low Reynolds number and near wall flows.

In high Reynolds number limit, Eq (45) gives Eq (38), which is

$$\nu_T = C_\mu \frac{k^2}{\varepsilon}$$

with  $C_\mu=0.0845$ , derived using RNG theory.

$\alpha_k$  and  $\alpha_\varepsilon$  are the inverse effective Prandtl numbers and are computed using the following formula derived analytically by RNG theory

$$\left| \frac{\alpha - 1.3929}{\alpha_0 - 1.3929} \right|^{0.6321} \left| \frac{\alpha + 2.3929}{\alpha_0 + 2.3929} \right|^{0.3679} = \frac{v_{mol}}{v_{eff}} \dots\dots\dots(47)$$

where  $\alpha_0=1$ . In the high Reynolds number limit ( $v_{mol} \ll v_{eff}$ )  $\alpha_k = \alpha_\epsilon \approx 1.393$ .

The main difference between RNG and Standard k- $\epsilon$  models is the additional  $R_\epsilon$  term in  $\epsilon$  equation, which is given by

$$R_\epsilon = \frac{C_\mu \eta^3 (1 - \eta / \eta_0) \epsilon^2}{1 + \beta \eta^3} \frac{1}{k} \dots\dots\dots(48)$$

where

$$\eta \equiv S \frac{k}{\epsilon}, \quad \eta_0 = 4.38 \quad \text{and} \quad \beta = 0.012 \dots\dots\dots(49)$$

The effect of this term in RNG  $\epsilon$  equation can be seen more clearly by rearranging equation (42). The third and fourth terms on the right hand side of equation (42) can be merged to give

$$\frac{\partial \epsilon}{\partial t} + U_i \frac{\partial \epsilon}{\partial x_i} = \frac{\partial}{\partial x_j} \left[ \alpha_\epsilon v_{eff} \frac{\partial \epsilon}{\partial x_j} \right] + C_{1\epsilon} \frac{\epsilon}{k} (G_k + C_{3\epsilon} G_b) - C_{2\epsilon}^* \frac{\epsilon^2}{k} \dots\dots\dots(50)$$

where

$$C_{2\epsilon}^* = C_{2\epsilon} + \frac{C_\mu \eta^3 (1 - \eta / \eta_0)}{1 + \beta \eta^3} \dots\dots\dots(51)$$

In the regions where  $\eta < \eta_0$ , the  $R$  term makes a positive contribution, and  $C_{2\epsilon}^*$  term becomes larger than  $C_{2\epsilon}$  and approaches to the value 2, which is close to  $C_{2\epsilon}$  in Standard k-  $\epsilon$  (1.92). So, for weakly and moderately strained flows, the RNG model tends to give results largely comparable to the standard model [2].

In the regions where  $\eta > \eta_0$ , however, the R term makes a negative contribution, making the value of  $C_{2\varepsilon}^*$  less than  $C_{2\varepsilon}$ . In comparison with the standard model, the smaller destruction of  $\varepsilon$  augments  $\varepsilon$ , reducing k and eventually the effective viscosity. As a result, in rapidly strained flows, the RNG model yields a lower eddy viscosity than the standard model.

Thus, the RNG model is more responsive to the effects of rapid strain and streamline curvature than the standard model, which explains the superior performance of the RNG model for certain classes of flows.

### **1.2.3. CFD Analysis of Airfoils and Blade Cascades**

Many researchers, especially dealing with turbomachinery and aerodynamics, focus on the computational study of airfoils, the blade cascades and wings to understand the characteristics of the flow around these objects and thus improve the performances of the related applications like turbomachinery, aircrafts etc. Usage of different solution techniques, algorithms and turbulence models are applied to different problems. The results of these simulations are compared with the experimental work that is done on the subject to have validation of the techniques. NASA Langley Research Center is one of the most relied sources of the experimental data, which the code generators or the implementers use for their validation. Below is the summary of several computational works done on performances of the blade cascades and airfoils by researchers. Their methodology, solution techniques and results are briefly explained.

Ahmed et.al [7] studied the numerical simulation of steady flow in a linear cascade of NACA 0012 airfoils with control volume approach. The flow field is determined by two-dimensional incompressible Navier Stokes equations and the effects of turbulence are accounted by standard k-  $\varepsilon$  model. They investigated the boundary

layer developed at the suction and pressure surfaces of the airfoil, the pressure, lift and drag coefficients employing different angles of attack ranging from 0 to 24 degrees and solidities ranging from 0.55 to 0.83. They considered the incoming flow to the infinite linear cascade as turbulence free. At the inlet boundary, incoming flow velocity is specified and at the pressure boundaries, the pressure is specified. The inlet and outlet boundaries are extended to four and five times the chord length of the airfoil, respectively, to have a proper description of the flow. The periodic boundary condition is applied to simulate infinite cascade model. After an iterative solution procedure of the governing equations, they found out that the lift and drag force increase as the angle of attack increases, but the maximum obtainable lift is reduced as solidity increases because the upper surfaces of the airfoils are influenced by the pressure suppression of the neighboring airfoils. The slight decrease in drag force is observed as the solidity is increased and it is concluded that this is due to the movement of separation point to trailing edge because of the pressure suppression of the airfoils.

Thole, K.A., Christophel, J.R., and Cunha, F.J. [8] studied the cooling at the tip of a turbine blade cascade using pressure side holes. Both experimental and CFD analysis are performed to have optimum configuration of the pressure side holes. The experiments are done on a large scale, low speed, closed loop wind tunnel providing an inlet velocity to the test section. The test results are compared with a CFD analysis performed on FLUENT 6.0, which is a commercial software. The authors employed unstructured grid using GAMBIT, and solved the Navier Stokes equations along with energy equation. The RNG k- $\epsilon$  turbulence model is applied in the solution. The computations were performed on a single turbine blade exposed to periodic conditions along all boundaries in the pitch direction. The inlet boundary conditions were set as uniform inlet velocity at approximately one chord upstream of the blade. Inlet mass flow boundary conditions are imposed on the cooling holes. After the experimental and computational analysis, optimum configuration and sizes of the pressure holes are investigated.

Catalano, P. and Amato M. [9] employed large set of turbulence models to typical aerodynamic applications for which certified experimental data are available in literature. They presented evaluation of turbulence models for these aerodynamic applications in terms of accuracy and numerical behavior. They tested the transonic flow over RAE 2822 airfoil and RAE M2155 wing and compared the results obtained for Spalart Allmaras, the Myong and Kasagi  $k-\epsilon$ , the Wilcox  $k-\omega$ , Kok TNT  $k-\omega$ , SST Menter  $k-\omega$  and a nonlinear eddy viscosity turbulence model with the experimental data available for several test cases. In the test with RAE 2822 airfoil, the Spalart Allmaras, the Myong and Kasagi  $k-\epsilon$  and Kok TNT provided similar results, more accurate than Wilcox  $k-\omega$  in terms of pressure and friction coefficients, velocity profiles and shock locations,. Among these models, SST Menter  $k-\omega$  and nonlinear model  $k-\epsilon$  gave the closest results to experimental data. In the test with RAE M2155 wing, the shock wave system is simulated in a satisfactory manner, and all the models predict a flow separation where the shocks meet. The Spalart–Allmaras, the Myong–Kasagi  $k-\epsilon$ , and the Kok TNT  $k-\omega$  yield a similar result, while the SST Menter  $k-\omega$  provides a solution similar to the nonlinear  $k-\epsilon$ . The Wilcox  $k-\omega$  predicts the flow to separate more outboard than all the other models and provides the smallest flow separated zone. For pressure coefficients, all the numerical results lie in a narrow band, and the comparison with the experimental data is generally good. In the sections where the shock boundary layer interaction is stronger, the nonlinear  $k-\epsilon$  and the Menter SST  $k-\omega$  better predict the shock location and the pressure recovery behind the shocks and in the trailing edge zones. The best results for velocity profiles are obtained by Menter SST  $k-\omega$  and the nonlinear  $k-\epsilon$  while the worst ones are obtained by the Wilcox and Kok TNT  $k-\omega$ .

The models are also tested for a high lift application, namely an A310 wing section is studied. The models did quite well and provide similar results for pressure coefficients before the stall occurs. The velocity profile results lied in a narrow band showing the same flow features. The aerodynamic coefficients are studied with only SST Menter and Kok TNT  $k-\omega$ , both showing reasonable accuracy but sudden characteristics of stall is only predicted by SST Menter  $k-\omega$ .

Anderson, W.K. and Bonhaus, D.L. [10] presented an implicit upwind algorithm for computing turbulent flows on unstructured grids. The inviscid fluxes are computed using an upwind algorithm and the solution is advanced in time using a backward-Euler time-stepping scheme. They showed the results for subsonic flow over a NACA 0012 airfoil, transonic flow over a RAE 2822 profile exhibiting a strong upper surface shock. They also showed the results for multi-element airfoils. The turbulence models for their study were Baldwin-Barth and Spalart-Allmaras models both of which are one-equation models. In the results for NACA 0012 test case, pressure distribution results obtained from the turbulence models were in good agreement with each other and experimental results although an overexpansion near the leading edge is observed in the computations, which is not seen in experimental results. The results of transonic flow over RAE 2822 showed that pressure distribution and shock location is well predicted by both models. The velocity profile results were in poor agreement with experimental data for the location  $x/c=0.75$ , but significantly better results were obtained in the location  $x/c=0.9$ . The authors also noted that previous studies with other turbulence models showed similar inaccuracies for the velocity profiles at location  $x/c=0.75$ . The cases for the multi-element airfoils indicate that good agreement between the computed and experimental pressures is obtained. Comparisons of computational and experimental velocity profiles are made at several stations on the upper surface of a three-element airfoil. At these locations, the flow is attached and the comparisons are good.

Xu, C. [11] in his dissertation, studied numerical analysis of two dimensional of turbine blade cascades. He adopted his code to several blade cascades and compared with experimental results. He used Baldwin-Lomax model to obtain turbulence quantities. Four types of boundaries are present, inlet and outlet flow boundaries, periodic boundaries and wall boundaries. The proposed and tested numerical solution gave results in agreement with the experimental results.

Pereira, L.A.A., Hirata, M.H., and Filho, N.M. [12] studied two-dimensional unsteady flow around multiple bodies at high Reynolds numbers using the vortex

method. They studied specifically flow characteristics around linear cascades of NACA 65-410 series airfoils and comparisons were made with results of potential flow theory and the findings from systematic study of NACA 65 series compressor blade sections in cascade. They implemented their solution with and without turbulence model. In general they concluded that the numerically predicted pressure distribution agrees well with experimental data however the potential flow results depart a little bit from the experimental values in the low-pressure surface. They observed no practical difference in the results of the simulation with and without turbulence in the neighborhood of the leading edge, since it is a low turbulence region. They observed that their model works more effectively in the rear part of the airfoils and in the wake regions and sub-grid turbulence modeling is essential in the trailing edge part of the airfoil.

Tulapurkara, E.G., [13] studied many turbulence models for the flow over airfoils, wings and a complete airplane. He summarized the advantages and disadvantages of the models being applied to airplane components, which the results for airfoils are as follows:

For computation of flow past airfoils, mixing length models of Cebeci and Smith, Baldwin and Lomax, the half-equation model of Johnson and King, the one-equation model of Spalart and Allmaras and Baldwin and Barth, the  $k-\epsilon$  model of Jones and Launder, the  $k-\omega$  model of Wilcox, the algebraic stress model (ASM) and Reynolds stress model have been used. The Cebeci and Smith model was popular in the 1970s and gives good results in case of attached flows. The Baldwin and Lomax model does equally well in these flows and has the simplicity aspect that boundary layer thickness is not involved in the computation. The Johnson and King model and its revised version take into account, to some extent, the departure from equilibrium in the boundary layer and gives a very good comparison with experimental data for flows with adverse pressure gradient. Computations using this model are able to predict the  $C_{Lmax}$  fairly well. The one-equation model of Spalart and Allmaras has also been found to predict well the  $C_L$  vs.  $\alpha$  (angle of attack) curve for multi-element airfoils. The  $k-\epsilon$ , model and  $k-\omega$  models also have similar capabilities. For situations

with large streamline curvature, like the flow past circulation-controlled airfoils, the Baldwin and Lomax model with correction for curvature gives reasonable results.

Hayashibara, S. [14] in his Ph.D. dissertation, studied the cascade flows around compressor blade sections both experimentally and numerically for the low Reynolds numbers. NACA 0015 airfoil and a linear cascade of NACA 65-(12) 10 are simulated using FLUENT, which is a finite volume CFD solver. The mesh is generated using GAMBIT. In the part where the flow around a single NACA 0015 airfoil is simulated, the main purpose was to validate and fine-tune both the experimental techniques and CFD simulation method to be used in the compressor cascade wake. The results were found satisfactory in terms of consistency between the experimental techniques and CFD method. The author studied mainly the boundary layer and wake characteristics of compressor blade cascades. He used a multi-block domain for the solution, corresponding to upper and lower surfaces of the airfoil, connected by a common interface boundary. As the previous references, periodic boundary condition is specified at the repeating direction for the airfoils. Hybrid mesh, which is the combination of structured and unstructured meshes, is employed in the domain. Structured mesh is applied around the airfoil (in the near wall region) while the rest of the domain is meshed with unstructured grid. As long as the boundary layers attached on the blade surface, the experimental and CFD results for velocity profiles showed good agreement with each other. Like the boundary layer characteristics, the wake characteristics of the cascade obtained both from the experimentation and CFD analysis were in fairly good agreement.

Yilbas, B.S. et al [15] studied numerical computation of the flow field around a cascade of NACA 0012 airfoils. The  $k-\epsilon$  model is employed to take into account the turbulence effects. The trailing edge separation at different angles of attack for solidity ratios and staggers is predicted and the resulting pressure, lift and drag coefficients are computed. They concluded that incidence at which the maximum lift occurs increases with solidity. The boundary layer thickness increases towards the trailing edge as the angle of attack increases while the rate of this increase reduces at

low solidity. They also observed that pressure coefficient on the suction surface at the trailing edge attains high values with an increase in incidence and with a decrease in solidity. Although it had not been predicted to be as drastic as that observed in the experiments, the lift coefficient is found to be reducing as the separation occurs. An increase in the lift and a slight increase in drag are observed as stagger angle is decreased at high incidences.

#### **1.2.4. CFD Analysis of Turbomachinery**

Design methods that use CFD techniques in turbomachinery area have become popular since one or two decades, because they produce competitive advantages by increasing the speed of the design cycle, reducing the testing time and therefore the necessary investment [16]. Design of a turbomachine was highly empirical and it required extensive development testing. As computers and their associated design software become tools of design, development time reduces appreciably. CFD improves the design techniques when used in making computational experiments to understand the flow physics.

The basic tools for the preliminary design of a turbomachine are not widely different from those performed two to three decades ago. The main change in preliminary design methods that has occurred in recent years after the introduction of CFD methods is the improvement of the computational and the graphical techniques for the presentation of results, enabling the designer to see the drawbacks of his design and apply necessary adjustments for the optimum design. Although there are many state-of-art works done on the CFD analyses of turbomachinery, only a few of them will be presented.

Oh, K.J. and Kang, S.H. [17] studied the dual performance characteristics of a small propeller fan. What is meant by dual characteristics is that the fan possesses radial type characteristics at low flow rates and axial type characteristics at high flow rates. They aimed investigating the sharp variation in the performance characteristics at

low flow rates. Finite volume method is used to solve the continuity and Navier-Stokes equations in the flow domain around the fan. The configuration of the fan was such that the fan was operating at the inlet of an open circular chamber. The governing equations were the continuity and the Reynolds-averaged N-S equations for an incompressible, viscous and turbulent flow. The Reynolds stresses are modeled using a modified k- $\epsilon$  turbulence model for swirling flows to account for a tangential velocity component imparted to the flow by the rotating fan. The employed boundary conditions were as follows:

- 1) Inlet and outlet sections: The streamwise gradient of flow variables is set to zero. The streamwise velocity component is corrected at the inlet and outlet planes so that the flowrate has a constant value.
- 2) Blade, hub and wall surface: The wall function method is employed. The first grid points next to the wall are placed in the logarithmic-law region and correlations of the wall function are imposed.
- 3) Periodic surfaces: Periodic boundary conditions are given on the periodic surfaces.
- 4) Wake centerline: Wake centerline conditions are given on the wake centerline.

Several conclusions were drawn from the performed analyses. When circumferentially averaged flow velocities are used to find the flow pattern in axial and radial flow directions, it is observed that at low flowrates, the radial velocity is much larger than the axial velocity in the fan region and the fluid in the fan region moves along the radial streamlines. The flow showed an inflow toward the hub, and a radial outflow at the tip, which makes an angular momentum change in the flow between the inlet and outlet of the fan. This is likely to cause a rapid increase in static pressure rise and fan power. At high flow rates, the flow follows axial streamlines in the fan region as can be expected in a normally operating fan.

Yan, J. and Smith, D.G. [18] conducted the CFD simulations of an axial turbine composed of two stator rows and a rotor row, and compared the solutions with the experimental results. The 3-d unstructured computational grid was constructed by GAMBIT and the solutions were obtained by FLUENT 5. The inlet total pressure and outlet static pressure boundary conditions were set up using the experimental results. The boundaries between rotor and stator were defined as periodic sliding interfaces. The rotor blades were defined as moving blades and the fluid around the blades as moving fluid. The flow is compressible due to high velocities. Reynolds stress model is implemented in the 3-d simulation of the turbine. The results for the 3-d simulation of the turbine showed very good agreement in the mass flow rate at the specified conditions (CFD result is 8.04 kg/s and experimental result is 8 kg/s). The Mach number distribution along the radial direction in the plane located 8.8 mm downstream of first stator blade row is 2% higher than experimental results. The authors concluded that considering the experimental error, the results were very well predicted by the CFD code. The yaw angle from the CFD at the mid-span is very close to experimental results. At the plane located 8.8 mm downstream of the rotor row, Mach number distribution from CFD shows good agreement with the test data in the mid-span and near the hub. However, near the casing the Mach numbers from the CFD are slightly higher than the test data. This is due to the tip clearance of rotor, which was not included in this computation. The yaw angle distribution at this plane from the CFD shows a generally similar profile to the test data. However, the complex details of the flow still have not been fully captured. Secondary flows around the blades are also predicted well by the unsteady flow calculations.

Corsini, A. and Rispoli, F. [19] presented the predictive performance of a non-linear turbulence closure in simulating the flow physics pertinent to a high-pressure axial ventilation fan. The study employed a cubic  $k-\varepsilon$  model. First, the authors performed validation tests on a flat plate with semi-circular leading edge and a double circular arc compressor cascade. The tests confirmed the improvement obtained in the simulating capabilities by using the cubic turbulence closure in highly complex flow configurations pertinent to turbomachinery. For the comparative analysis on the axial

ventilation fan, the authors concluded that the non-linear model was shown to provide a better base line for simulating non-equilibrium effects than the standard one. Concerning the flow survey behind the fan rotor for the tested operating points, the non-linear solution improved the swirl prediction and was in agreement with the available LDA data. The sensitization of the cubic stress dependence to strain and vorticity is considered as critical to modeling accurately severe 3D flow structure which is not achievable with the linear eddy diffusivity approach.

Lin, S.C. and Huang, C.L. [20] performed the analysis of a forward curved centrifugal fan both experimentally and numerically. The numerical simulation of the fan is done by a commercial CFD Code. The solution domain is divided into three parts, inlet region, rotor region and outlet region. These three parts have different mesh densities, according to the severity of the flow conditions. The results for CFD simulation served as a tool for arranging the diffuser section for low noise levels and adjusting the blade angles. The differences between experimental and numerical results were less than 5.4% for all the cases considered in the study.

Thakker, A. and Hourigan, F. [21] compared the 3-d computational fluid dynamics simulation of an impulse turbine with fixed guide vanes with the empirical performance data. GAMBIT and FLUENT are used to construct the model and perform the numerical simulation. In the simulation, mixing plane model is used to allow the modeling of one rotor/guide vane combination. Because the impulse turbine has both upstream and downstream guide vanes, two mixing planes were constructed, one is at the interface between pressure outlet of the upstream guide vanes and rotor, and one is at the interface between pressure outlet of the rotor and pressure inlet of the downstream guide vanes. The tip gap is not modeled; affecting the results in that a source of loss in the turbine is ignored and a smaller pressure drop across the turbine will be obtained than that was obtained experimentally. Additionally, hub and casing walls had zero shear specified on them to reduce the computational effort, resulting in lower predicted losses. Hybrid meshing scheme is used, allowing hexahedral cells in the near blade region of the guide vane and rotor,

and tetrahedral / pyramid cells in the rest of the domain. The standard  $k-\varepsilon$  model is employed as turbulence model with non-equilibrium wall functions. The reason why the non-equilibrium wall functions are preferred to standard wall functions is that they are better able to deal with complex flows involving separation, reattachment and strong pressure gradients. Solution adaptive grid refinement is also performed in the regions where strong pressure and velocity gradients occur. The torque produced by the turbine was well predicted by the model. Certain simplifications were made in the model, which were expected to lead lower prediction of losses. As a result, overall efficiency is over-predicted. The CFD simulation yielded a maximum efficiency of 54% as compared to a maximum efficiency of 49% from the experiment.

Widmann, J.F., et al [22] examined the flow through a vane –cascade swirl generator both experimentally and numerically. In the numerical analysis FLUENT is used. Two turbulence models, namely standard  $k-\varepsilon$  and RNG  $k-\varepsilon$  are employed for the turbulence models. The numerical simulations were generated using a segregated, implicit solver. The pressure and velocity were coupled using the PISO algorithm with neighbor and skewness correction, and standard wall functions were used for the near-wall treatment. When the RNG  $k-\varepsilon$  turbulence model was implemented, *the swirl-dominated flow* option was used. This option sets the swirl constant to 0.07. The authors meshed the computational domain with unstructured grid and modeled only  $30^\circ$  portion of it because of rotationally periodic symmetry in the swirl generator. The simulation results for the velocity magnitude at the outlet of the annulus using RNG  $k-\varepsilon$  model compared well with the experimental data, while the standard  $k-\varepsilon$  method fails to predict the recalculation zone observed near the inner wall of the annulus. The authors also computed the swirl number, which is an important parameter for the design of swirl generators, noting that this value should be validated with experimental results.

Danczyk, S.A. [23] performed the analysis of the flow field inside an axial flow fan both experimentally and numerically in his dissertation. Flow field inside the axial

fan is simulated in a commercial computational fluid dynamics code, CFX-TASCflow. The simulation modeled the first stage of the fan using three stator blades and two rotor blades. The full three-dimensional flow field was calculated and mid-span values are compared with Laser Doppler Anemometer measurements. Total pressure equal to atmospheric pressure is imposed at the inlet of the fan and the pressure at the outlet of the fan is taken from the experiments. Because the tip speed of the rotor blades is low enough, incompressible model is used. The computational grids were created with the objective to obtain high grid density in the region between the trailing edges of the stator blades and leading edges of the rotor blades. The turbulence model for the solution is a blend of  $k-\epsilon$  and  $k-\omega$  models. Because  $k-\epsilon$  model predicts the onset of separation from the walls too late and under-predicts the amount of separation,  $k-\omega$  model is used near the wall. Because the  $k-\omega$  model is strongly dependent on free stream conditions, the results are overly sensitive to the inlet specification of  $\omega$ , so  $k-\epsilon$  model is implemented at the outer region. For the results, calculated absolute mean velocities compared well to the measured values of the flow field in the free stream areas and seem to under-predict the velocity in the wake regions. The results for the simulation are also well for the flow between the rotor blades but the turbulence level is under-predicted.

### **1.2.5. Axial Flow Fans**

Axial flow fans are the types of fans that the fluid flow is predominantly axial, parallel to axis of rotation. Axial flow fans usually use air as the working fluid that operates in incompressible range, at low speeds and moderate pressures. In an axial flow fan, the flow is ideally axial, with no radial component, and the required pressure rise comes from the increase in the tangential velocity component due to rotation of the impeller and an aerodynamic diffusion process afterwards.

Axial fans are mainly used for ventilating and air conditioning applications of the buildings, mines, vehicles, underground transportation systems etc. Each application demands a different type of fan. To handle the system, specific fans are more

appropriate than others in terms of capacity and pressure rise capabilities. In this sense, axial flow fans are generally categorized into four types.

#### 1.2.5.1. Axial Flow Fan Types

- **Propeller Fans:** Sometimes called as the panel fans, propeller fans are the lightest, least expensive and most commonly used fans. These fans normally consist of a flat frame or housing to be mounted in a wall or in a partition to exhaust air from a building. This exhausted air has to be replaced by fresh air, coming in through other openings. If these openings are large enough, the suction pressure needed is small. The propeller fans, therefore, are designed to operate in the range near free delivery, to move large air volumes against low static pressures.

These fans can be built both direct drive and belt drive (Figure 1.3 and Figure 1.4). In direct drive arrangement, an electric motor is directly mounted to fan wheel, while a belt and pulley configuration is used to transfer the rotation from motor shaft to fan wheel in belt drive arrangement. Belt drive results in flexibility in performance, since any rotational speeds can be obtained for the fan wheel by selection of proper pulley ratio. In large sizes, belt drive is preferable since it will keep the speed of the fan wheel low or moderate while keeping the motor speed high, for lower cost because high-speed motors are less expensive than the low-speed motors of the same horsepower [24]. The direct drive arrangements have lower number of components resulting in lower cost and require no maintenance and regular checkups for adjustment of the belt. Direct drives are more efficient than the belt drives since some of the power is consumed in the belt pulley arrangement.



**Figure 1.3:** Propeller fan with direct drive

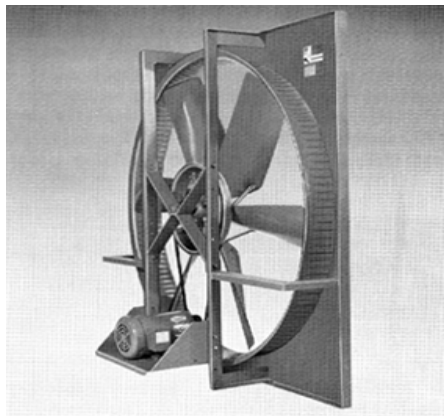


**Figure 1.4:** Propeller fan with belt drive

- **Tube-axial Fans:** A tube-axial fan is a glorified type of propeller fan with a cylindrical housing about one diameter long, containing a motor support, a motor and a fan wheel. The motor can be located either on upstream or downstream of the fan wheel. The fan wheel of a tube-axial fan can be similar to that of a propeller fan. It often has a medium sized hub diameter, about 30 to 50% of the blade outside diameter. The units are designed to operate in the ranges of moderate static pressures, higher than for a propeller

fan. A tube-axial fan can be connected to an inlet duct or an outlet duct or both but the best application is exhausting from an inlet duct because any length of outlet duct results in larger pressure losses after the fan wheel due to presence of air spin. Figure 1.5 is a typical tube-axial fan.



**Figure 1.5:** Tube-axial fan

- **Vaneaxial Fans:** A vaneaxial fan is a more elaborate unit than the previous ones. It has the outside appearance of a cylindrical housing at least one diameter long. As in a tube-axial fan, this housing contains the motor support, the motor, and the fan wheel but the vaneaxial fan housing includes a set of guide vanes and sometimes an inner ring, a converging tailpiece, and an expanding diffuser for static regain. The guide vanes at the downstream of the fan wheel removes the rotational component of the air, slowing it down, and converting some of the excess velocity pressure into more useful static pressure [25]. The hub diameter of a vaneaxial fan is larger than that of a tube-axial fan, usually between 50 to 80 % of the blade outside diameter. The vaneaxial fans are designed to operate in the range of fairly high static pressures. Figure 1.6 shows an example of vaneaxial fan.



**Figure 1.6:** Vaneaxial fan

- **Two-Stage Axial Fans:** Two-stage axial fans are sometimes a good solution for applications where higher static pressure is required. There are two ways to design a two-stage axial flow fan; two fan wheels rotating in the same direction with guide vanes placed between the two stages and two counter-rotating fan wheels with no guide vanes at all. By either method, the static pressure is doubled. In the first method, the guide vanes pick up the helical flow produced by the rotating blades of the first stage and reverse the rotational component to the opposite direction, and prepare the flow to second stage. In other words, they behave as the outlet vanes for the first stage and inlet vanes for the second stage. This configuration has the advantage that the same fan wheel shaft can be used for both stages with adjustments on blade angles for the second stage. In the second method, two fan wheels run in opposite directions and are driven by two separate motors. The air spin produced by the first stage is more or less neutralized by the deflection produced by the second stage. As a result, no guide vanes are needed, which reduces the manufacturing cost and compensates for the

possible extra expense of two motors instead of one. Another advantage of this configuration is that in case that one motor should fail, the unit can still deliver some air with only one stage running.

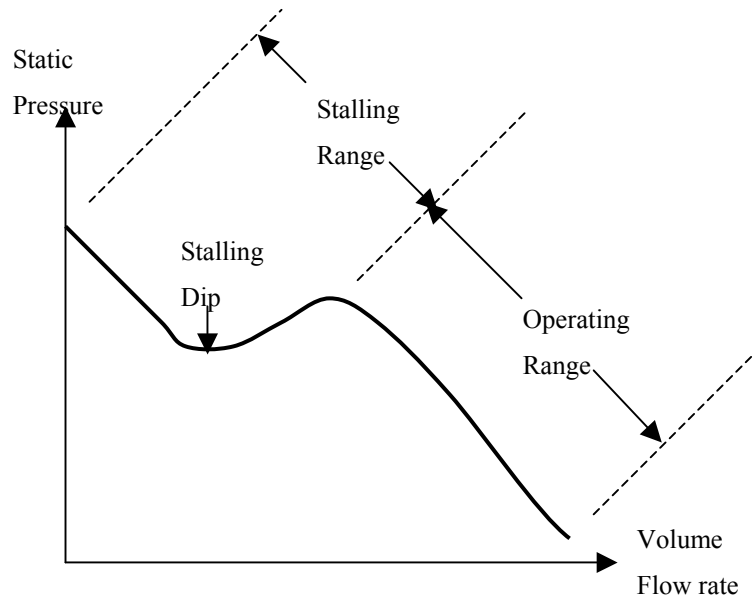


**Figure 1.7:** Two-stage axial flow fan

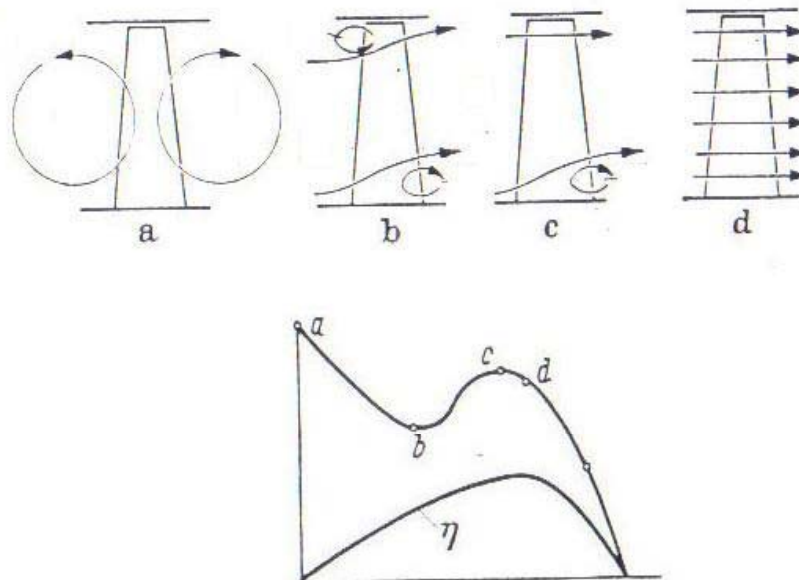
#### **1.2.5.2. Performance of Axial Flow Fans**

Figure 1.8 shows the shape of a typical pressure versus flowrate curve. Starting from the free delivery, the pressure value rises to a peak value. This is the good operating range for an axial flow fan. As the air volume decreases due to increasing restrictions, the axial air velocity decreases as well, resulting in an increased angle of attack and increased lift coefficients (the phenomena can be understood better in Chapter 2). The increase in the lift coefficient is responsible for the increase in the pressure. After the maximum lift angle is reached, the flow can no longer follow the upper contour of the blades, thus separate from the surface of the blade. Separated flow results in a decrease in lift coefficient, thus a decrease in pressure occurs. This phenomenon is called stall. After the stalling, the axial flow fan starts acting like an inefficient and noisy mixed flow fan. As the airflow approaches the fan inlet, the blades throw the air outward by centrifugal force and in this way produce the static

pressures of the stalling range, which keeps until the point of no delivery is reached. At this point, the blades act as a paddle wheel creating radial flow only. Figure 1.9 is a sketch of the flow behavior at different points on the pressure curve.



**Figure 1.8:** Static Pressure vs. Volume flowrate of an axial fan [24].



**Figure 1.9:** Effect of different flow conditions on axial fan performance [26].

In order to have a good operation with axial flow fans, one should provide a safety margin in order not to cause the fan to work in the inefficient and noisy stalling range. A good practice is that the peak pressure of the operating range should be 30 to 50 % higher than the pressure required for the application. This pressure safety margin will allow for possible errors that may have been made in the determination of system resistance and to allow for possible fluctuations of the system [24].

### **1.3. Overview of the FLUENT CFD Program**

#### **1.3.1. Introduction**

FLUENT is a state-of-the-art computer program for modeling fluid flow and heat transfer in complex geometries, using Finite Volume Method (FVM). The program provides complete mesh flexibility, solving the flow problems with unstructured meshes that can be generated about complex geometries with relative ease. Supported mesh types include 2D triangular/quadrilateral, 3D tetrahedral/hexahedral/pyramid/wedge, and mixed (hybrid) meshes. FLUENT also allows the user to refine or coarsen your grid based on the flow solution.

FLUENT is written in the C computer language and makes full use of the flexibility and power offered by the language. Consequently, true dynamic memory allocation, efficient data structures, and flexible solver control are all made possible.

All functions required to compute a solution and display the results are accessible in FLUENT through an interactive, menu-driven interface. The user interface is written in a language called Scheme, a dialect of LISP. The advanced user can customize and enhance the interface by writing menu macros and functions.

### 1.3.2. Program Structure

FLUENT package includes the following products:

- FLUENT, the solver.
- prePDF, the preprocessor for modeling non-premixed combustion in FLUENT.
- GAMBIT, the preprocessor for geometry modeling and mesh generation.
- TGrid, an additional preprocessor that can generate volume meshes from existing boundary meshes.
- Filters (translators) for import of surface and volume meshes from CAD/CAE packages such as ANSYS, I-DEAS, NASTRAN, PATRAN, and others.

Figure 1.10 shows the organizational structure of these components.

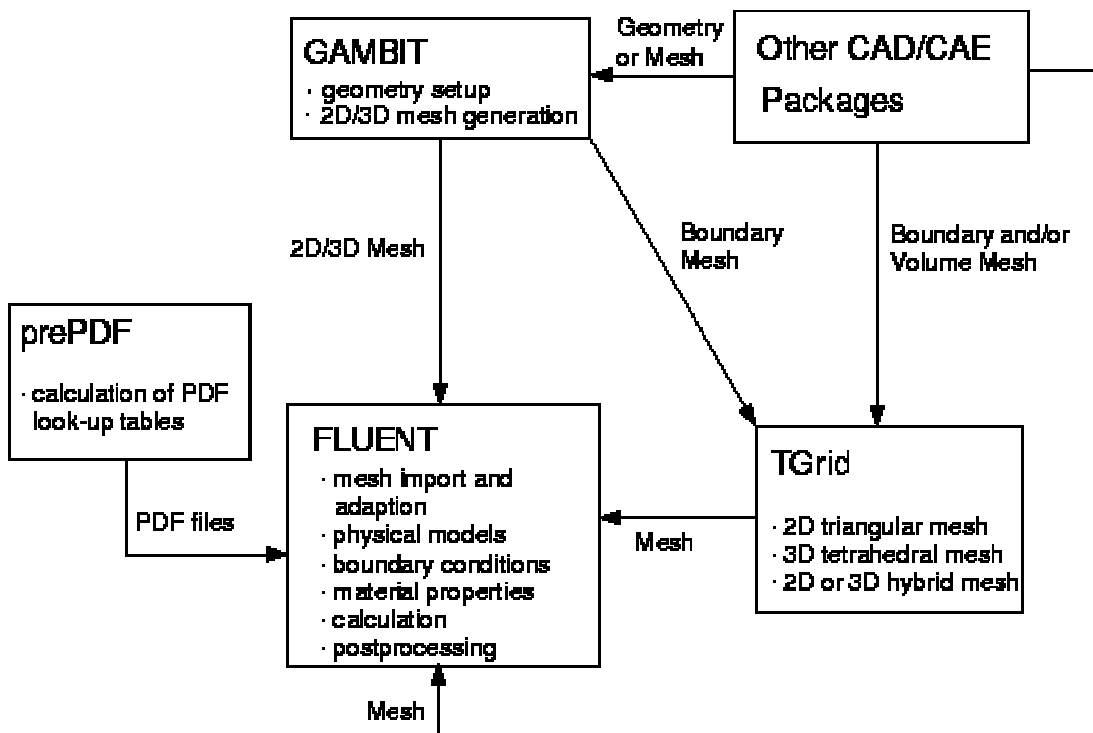


Figure 1.10: Basic Program Structure [2].

The user can create the geometry and grid by GAMBIT. Once a grid has been read into FLUENT, all remaining operations are performed within the solver. These include setting boundary conditions, defining fluid properties, executing the solution, refining the grid, and viewing and post processing the results.

### **1.3.3. Program and Modeling Capabilities**

Comprehensive modeling capabilities for a wide range of incompressible and compressible, laminar and turbulent fluid flow problems are provided in the program. A broad range of mathematical models for transport phenomena (like heat transfer and chemical reactions) is combined with the ability to model complex geometries. The range of problems that can be addressed is very wide. Applications include laminar non-Newtonian flow modeling in process equipment, turbulent heat transfer in turbomachinery and automotive engine components, pulverized coal combustion in utility boilers, compressible jets in process equipment, external aerodynamics and compressible reacting flow in solid rocket motors.

To permit modeling of fluid flow and related transport phenomena in industrial equipment and process, various useful features are provided in FLUENT. These include porous media, lumped parameter (fan and heat exchanger), streamwise-periodic flow and heat transfer, swirl and moving reference frame models. The moving reference frame family of models includes the ability to model single or multiple reference frames. A time-accurate sliding mesh method, useful for modeling multiple stages in turbomachinery applications, for example, is also provided, along with the mixing plane model for computing time-averaged flow models.

Another very useful set of models is the set of discrete phase models. These models can be used to analyze sprays and particle-laden flows in equipment like cyclones and aircraft-engine inlets. Several models for multiphase flows are also available,

and can be used, for example, to predict jet breakup, the motion of liquid after a dam break, cavitation, sedimentation and separation.

Turbulence models provided have a broad range of applicability without the need for fine-tuning to a specific application, and they include the effects of other physical phenomena, such as buoyancy and compressibility. Particular care has been devoted to addressing issues of near-wall accuracy via the use of extended wall functions and zonal models.

Various models of heat transfer can be modeled, including natural, forced and mixed convection with or without added complications such as conjugate heat transfer, porous media etc. The set of radiation models and related submodels for modeling participating media are general and can take into account the complications of combustion. A particular strength is the ability to model combustion phenomena via eddy dissipation models or probability density function models. A host of other models that is very useful for combustion applications are also available, including coal and droplet combustion and pollutant formation models.

#### **1.3.4. Boundary Conditions**

Boundary conditions specify the flow and thermal variables on the boundaries of the physical model. They are, therefore critical component of CFD simulations and it is important that they are specified appropriately. The boundary types that are available in FLUENT as follows:

- Flow inlet and exit boundaries: pressure inlet, velocity inlet, mass flow inlet, inlet vent, intake fan, pressure outlet, pressure far-field, outflow, outlet vent, exhaust fan
- Wall, repeating, and pole boundaries: wall, symmetry, periodic, axis
- Internal cell zones: fluid, solid (porous is a type of fluid zone)
- Internal face boundaries: fan, radiator, porous jump, wall, interior

Most commonly used boundary condition types will be presented briefly.

#### **1.3.4.1. Flow Inlet/Exit Boundary Conditions**

FLUENT provides 10 types of boundary zone types for the specification of flow inlets and exits

- Velocity inlet boundary conditions are used to define the velocity and scalar properties of the flow at inlet boundaries.
- Pressure inlet boundary conditions are used to define the total pressure and other scalar quantities at flow inlets.
- Mass flow inlet boundary conditions are used in compressible flows to prescribe a mass flow rate at an inlet. It is not necessary to use mass flow inlets in incompressible flows because when density is constant, velocity inlet boundary conditions will fix the mass flow.
- Pressure outlet boundary conditions are used to define the static pressure at flow outlets (and also other scalar variables, in case of backflow). The use of a pressure outlet boundary condition instead of an outflow condition often results in a better rate of convergence when backflow occurs during iteration.
- Pressure far-field boundary conditions are used to model a free-stream compressible flow at infinity, with free-stream Mach number and static conditions specified. This boundary type is available only for compressible flows.
- Outflow boundary conditions are used to model flow exits where the details of the flow velocity and pressure are not known prior to solution of the flow problem. They are appropriate where the exit flow is close to a fully developed condition, as the outflow boundary condition assumes a zero normal gradient for all flow variables except pressure. They are not appropriate for compressible flow calculations.
- Inlet vent boundary conditions are used to model an inlet vent with a specified loss coefficient, flow direction, and ambient (inlet) total pressure and temperature.

- Intake fan boundary conditions are used to model an external intake fan with a specified pressure jump, flow direction, and ambient (intake) total pressure and temperature.
- Outlet vent boundary conditions are used to model an outlet vent with a specified loss coefficient and ambient (discharge) static pressure and temperature.
- Exhaust fan boundary conditions are used to model an external exhaust fan with a specified pressure jump and ambient (discharge) static pressure.

#### **1.3.4.2. Wall Boundary Conditions**

Wall boundary conditions are used to bound fluid and solid regions. In viscous flows, the no-slip boundary condition is enforced at walls by default, but one can specify a tangential velocity component in terms of the translational or rotational motion of the wall boundary, or model a "slip" wall by specifying shear. The shear stress and heat transfer between the fluid and wall are computed based on the flow details in the local flow field.

#### **1.3.4.3. Symmetry Boundary Conditions**

Symmetry boundary conditions are used when the physical geometry of interest and the expected pattern of the flow/thermal solution have mirror symmetry. They can also be used to model zero-shear slip walls in viscous flows. Symmetry boundaries are used to reduce the extent of the computational model to a symmetric subsection of the overall physical system.

#### **1.3.4.4. Periodic Boundary Conditions**

Periodic boundary conditions are used when the physical geometry of interest and the expected pattern of the flow/thermal solution have a periodically repeating

nature. FLUENT treats the flow at a periodic boundary as though the opposing periodic plane is a direct neighbor to the cells adjacent to the first periodic boundary. Thus, when calculating the flow through the periodic boundary adjacent to a fluid cell, the flow conditions at the fluid cell adjacent to the opposite periodic plane are used. Two types of periodic conditions are available in FLUENT. The first type does not allow a pressure drop across the periodic planes. The second type allows a pressure drop to occur across translationally periodic boundaries, enabling you to model "fully-developed" periodic flow. For a periodic boundary without any pressure drop, there is only one input that the user needs to consider: whether the geometry is rotationally or translationally periodic. Rotationally periodic boundaries are boundaries that form an included angle about the centerline of a rotationally symmetric geometry. Figure 1.11 illustrates rotational periodicity. Translationally periodic boundaries are boundaries that form periodic planes in a rectilinear geometry. Figure 1.12 illustrates translationally periodic boundaries.

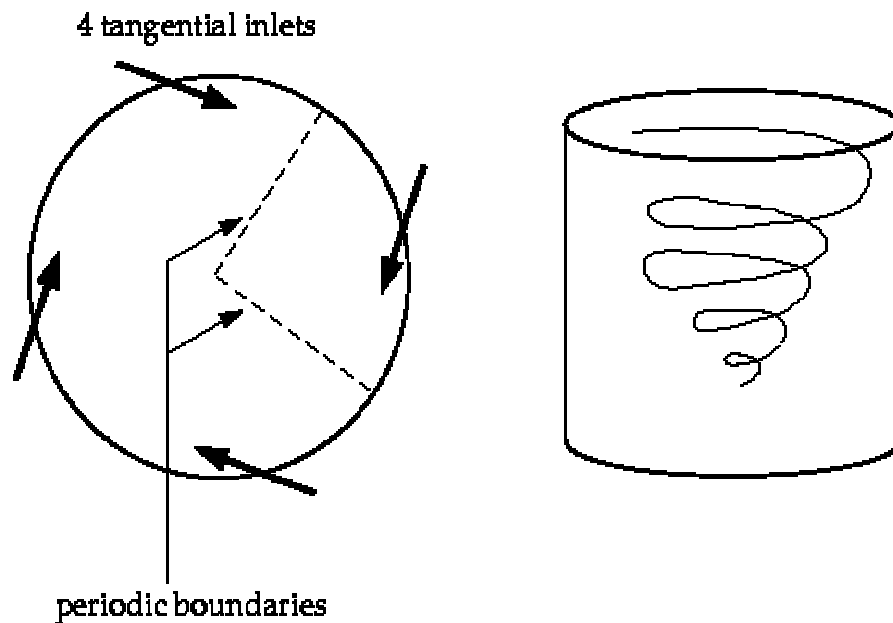


**Figure 1.11:** Rotationally periodic boundary conditions, swirling flow in a cylindrical vessel [2].

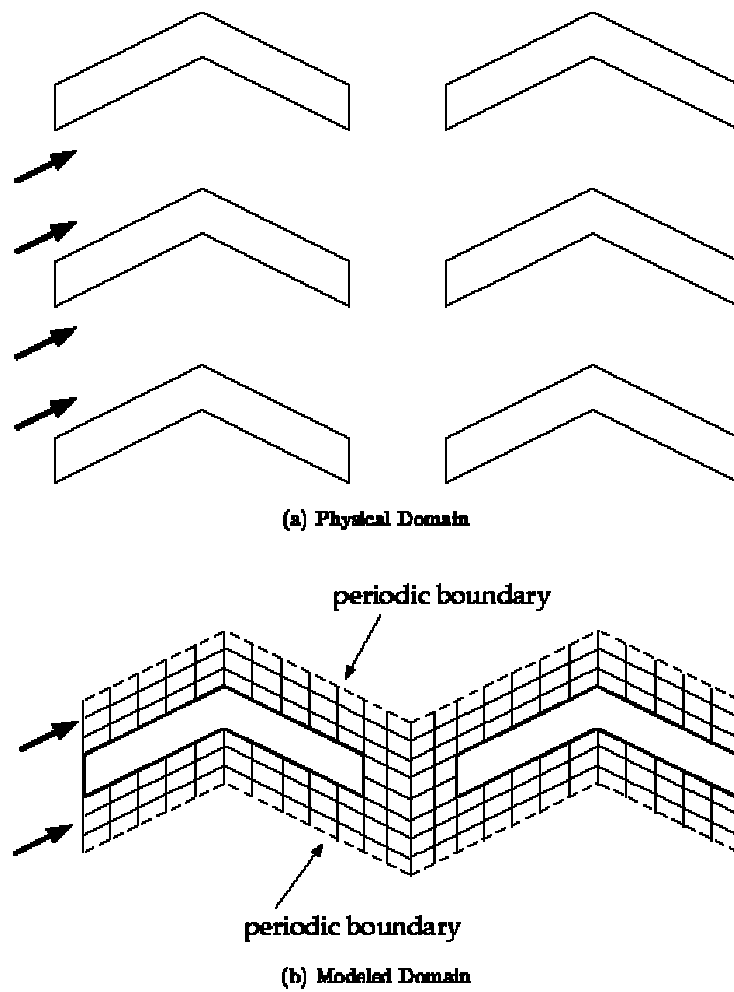


**Figure 1.12:** Translationally periodic boundary conditions [2].

### 1.3.5. Numerical Schemes

There are two numerical methods that FLUENT allows the user:

- Segregated Solver
- Coupled Solver

Using either method, FLUENT will solve the governing integral equations for the conservation of mass and momentum, and (when appropriate) for energy and other

scalars such as turbulence and chemical species. In both cases a control-volume-based technique is used that consists of:

- Division of the domain into discrete control volumes using a computational grid.
- Integration of the governing equations on the individual control volumes to construct algebraic equations for the discrete dependent variables (unknowns) such as velocities, pressure, temperature, and conserved scalars.
- Linearization of the discretized equations and solution of the resultant linear equation system to yield updated values of the dependent variables.

The two numerical methods employ a similar discretization process (finite-volume), but the approach used to linearize and solve the discretized equations is different.

Using segregated solver approach, the governing equations are solved sequentially (i.e., segregated from one another). Because the governing equations are non-linear (and coupled), several iterations of the solution loop must be performed before a converged solution is obtained. In the coupled solver, the governing equations of continuity, momentum, and (where appropriate) energy and species transport are solved simultaneously (i.e., coupled together). Governing equations for additional scalars are solved sequentially (i.e., segregated from one another and from the coupled set) as the segregated solver. Because the governing equations are non-linear (and coupled), several iterations of the solution loop must be performed before a converged solution is obtained.

### **1.3.6. Solution Adaptive Grid**

The solution adaptive mesh refinement feature allows refining and/or coarsening the grid based on geometric and numerical solution data. By using solution-adaptive refinement, cells can be added where they are needed in the mesh, thus enabling the features of the flow field to be better resolved. When adaption is used properly, the

resulting mesh is optimal for the flow solution because the solution is used to determine where more cells are added. In other words, computational resources are not wasted by the inclusion of unnecessary cells, as typically occurs in the structured grid approach. Furthermore, the effect of mesh refinement on the solution can be studied without completely regenerating mesh.

Solution-adaptive grid capability is particularly useful for accurately predicting flow fields in regions with large gradients, such as free shear layers and boundary layers. In comparison to solutions on structured or block-structured grids, this feature significantly reduces the time required to generate a good grid. Solution-adaptive refinement makes it easier to perform grid refinement studies and reduces the computational effort required to achieve a desired level of accuracy, since mesh refinement is limited to those regions where greater mesh resolution is needed.

The advantages of solution-adaptive refinement are significant. However, the capability must be used carefully to avoid certain pitfalls. Some guidelines for proper usage of the solution-adaptive refinement are as follows:

- The surface mesh must be fine enough to represent adequately the important features of the geometry. For example, it would be bad practice to place too few nodes on the surface of a highly curved airfoil, and then use solution refinement to add nodes on the surface. Clearly, the surface will always contain the facets contained in the initial mesh, regardless of the additional nodes introduced by refinement.
- The initial mesh should contain sufficient cells to capture the essential features of the flow field. In addition to having sufficient surface resolution to represent the shape of the body, the initial mesh should also contain enough cells so that a reasonable first solution can be obtained. Subsequent grid adaptation can be used to sharpen the shock and establish a grid-independent solution.

- A reasonably well-converged solution should be obtained before an adaptation is performed. If adapted to an incorrect solution, cells will be added in wrong region of the flow. However, careful judgment must be used in deciding how well to converge the solution before adapting, because there is a trade-off between adapting too early to an unconverged solution and wasting time by continuing to iterate when the solution is not changing significantly.

## CHAPTER 2

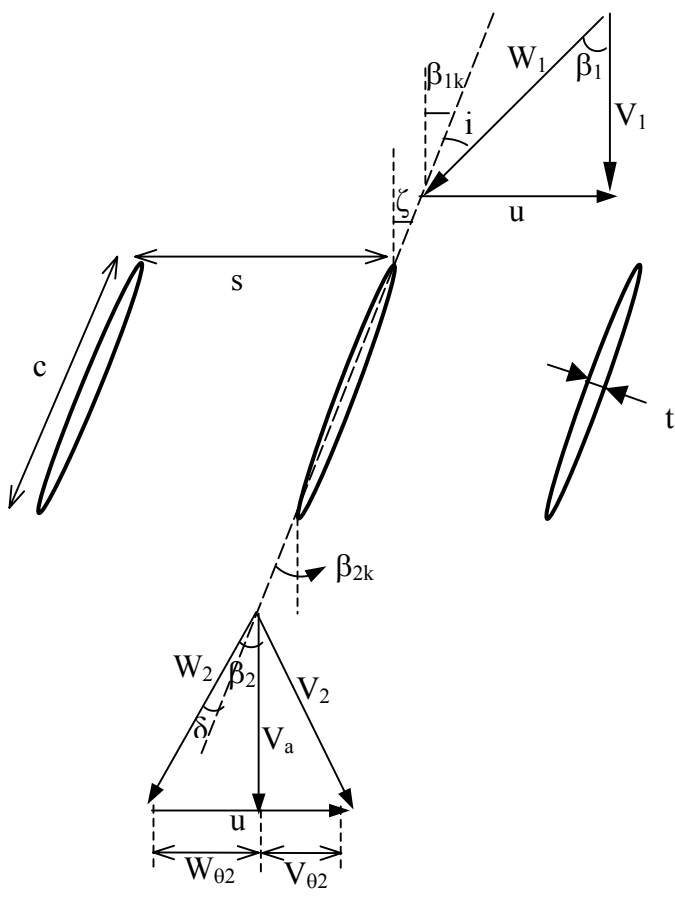
### AERODYNAMIC PERFORMANCE ANALYSIS OF BLADE CASCADES

#### 2.1. The Blade Profile

Because the reversible fans are supposed to work with the same performance when their direction of rotation is reversed, the blade profiles must be fully symmetrical. Not only the leading edges of the blades behave as trailing edges and the trailing edges behave as the leading edges, but also the pressure and suction sides of the blades alter their roles in opposite working directions. To satisfy these conditions, elliptical profiles with no camber are used. The maximum thickness of the blade is selected as 8% of the blade chord and location of the maximum thickness lies in the middle of the line connecting the leading and trailing edges of the blade. The aerodynamic performances of the profiles are computed for different solidities, angles of attack and incoming velocities.

In the design phase of the reversible axial flow fan, it will be assumed that there is no radial component of the velocity at the fan inlet and the pressure rise across the rotor is constant in the radial direction (free vortex design). As a result, pressure difference does not occur across the streamlines at the exit of the rotor and the streamlines consist of only axial and tangential components. Due to this fact, the aerodynamic performance is computed on a two-dimensional plane. In an axial turbomachine, the blades can be thought as if they lie on a line of infinite length so the solutions are obtained for an infinitely long linear cascade of blades.

Schematic view of the linear cascade and the velocity triangles are as follows:



- V : Absolute velocity
- W : Relative velocity
- u : Rotational velocity
- $\beta$  : Relative fluid angle
- c : Blade chord
- s : Blade spacing
- t : Blade thickness
- $\delta$  : Deviation angle
- i : Incidence
- $\beta_k$ : Relative blade angle
- $\zeta$  : Stagger angle
- $\sigma = \frac{c}{s}$  : Solidity
- $\frac{t}{c} = 0.08$
- Subscripts
- a: axial component
- $\theta$ : Tangential component

**Figure 2.1:** Linear blade cascade and velocity triangles

In the figure, subscripts  $\theta$ , a, 1 and 2 stand for the tangential direction, axial direction, rotor inlet and rotor outlet, respectively and the nomenclature is given in the figure.

**2.2. Calculation of Aerodynamic Parameters**

The main aerodynamic parameters that are used in the design of an axial fan can be classified as lift coefficient, drag coefficient, incidence and deviation angles. Lift coefficient and drag coefficient are the ratios of the lift and drag forces exerted on

the unit blade area by the flow to a term that accounts for the dynamic pressure of the flow. Before proceeding further on the details of the parameters, a sketch of the forces occurring on the cascade should be presented.

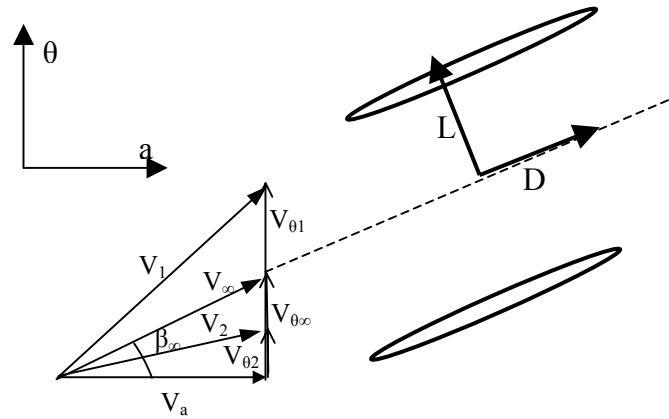


**Figure 2.2:** The forces on a stationary blade cascade

The Figure 2.2 introduces the forces exerted by the flow onto a stationary blade cascade.  $L$  is the lift force and  $D$  is the total drag force on the blades.  $L$  is perpendicular and  $D$  is parallel to the mean velocity, which is given by Eq (52).

$$\vec{V}_\infty = \frac{\vec{V}_1 + \vec{V}_2}{2} \dots\dots\dots(52)$$

As noted before,  $V_1$  and  $V_2$  are the velocities at the inlet and exit sections of the blades respectively.

$$\vec{V}_1 = \vec{V}_{\theta 1} + \vec{V}_{a1} \quad \text{and} \quad \vec{V}_2 = \vec{V}_{\theta 2} + \vec{V}_{a2} \dots\dots\dots(53)$$

In axial turbomachinery, the axial components of the velocities ( $V_a$ ) at the inlet and outlet are said to be constant due to continuity equation. So, if the axial components of the velocities are taken to be equal, then the mean velocity is given by Eq (54).

$$V_{a1} = V_{a2} = V_a \Rightarrow V_{\theta\infty} = \frac{V_{\theta1} + V_{\theta2}}{2} \dots\dots\dots(54)$$

In a single stage fan, in the absence of inlet guide vanes, the incoming velocity is assumed to have no tangential component, in other words the flow is pure axial. Then,

$$V_{\theta1} = 0 \Rightarrow V_{\theta\infty} = \frac{V_{\theta2}}{2} \dots\dots\dots(55)$$

The direction of the mean velocity is defined by the angle between the axial direction and the mean velocity direction, which is  $\beta_\infty$  in Figure 2.2.

The lift and drag coefficients of the blades located in cascades are functions of magnitude of the mean velocity, angle of attack, the shape of the profile and solidity of the blades. The coefficients for elliptical profiles are examined by changing these parameters in two-dimensional cascades.

The lift coefficient and drag coefficient are formulated as follows. A detailed derivation can be found in Ref [27].

$$C_L = \frac{L}{\frac{1}{2} \times \rho \times V_\infty^2 \times A_p} \quad \text{and} \quad C_D = \frac{D}{\frac{1}{2} \times \rho \times V_\infty^2 \times A_p} \dots\dots\dots(56)$$

$A_p$  is the projected wing area and is given by

$$A_p = c \times s \dots\dots\dots(57)$$

where  $s$  is the span and  $c$  is the chord of the blade.

After giving the nomenclature and terminology of the velocity triangles, lift and drag coefficient concepts, it is appropriate to continue with the performance analysis of the elliptical sections, CFD analysis of which is carried out using FLUENT 6.0.

### 2.3. Computational Mesh and Boundary Conditions

The computational mesh is generated with Gambit 2.0, which is the pre-processor of FLUENT 6.0. The elliptical profiles are located in a rectangular domain through which the air stream passes. The mesh is composed of triangular elements. A sample of computational domain is given in Figure 2.3.

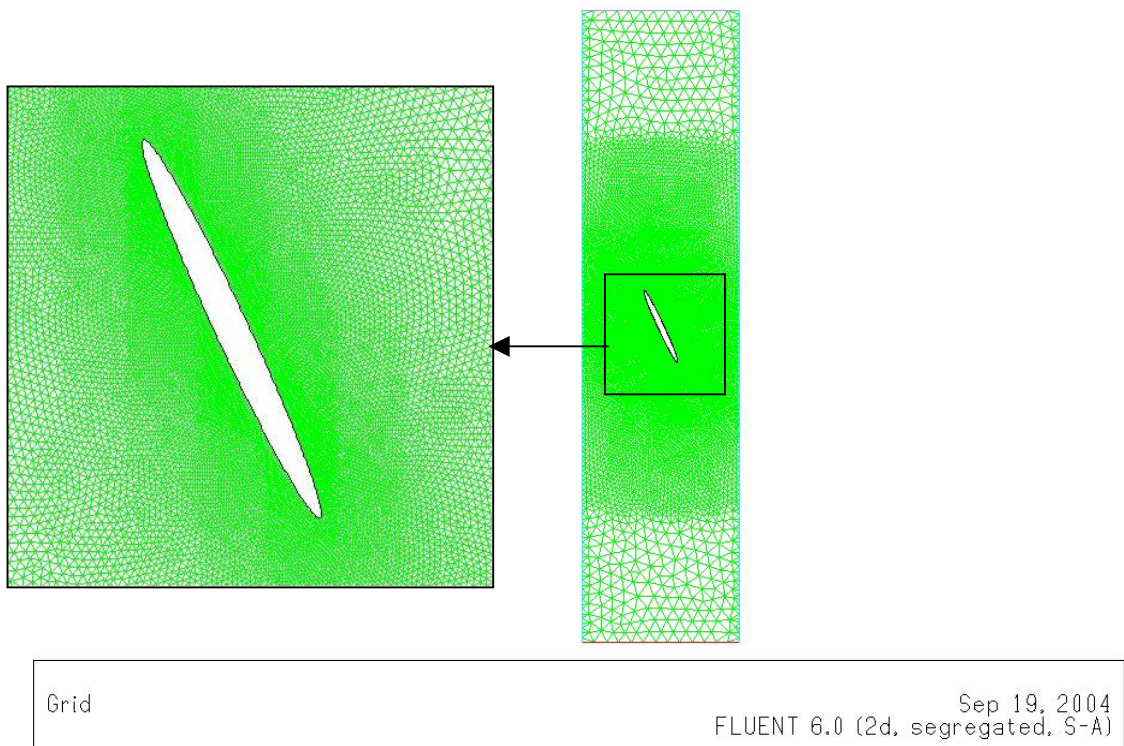


**Figure 2.3:** Computational mesh around the elliptical blade profile for  $\sigma = 0.5$  solidity and  $25^\circ$  angle of attack.

In Figure 2.3, the width of the rectangular domain is determined by the solidity of the cascade. In this case, the solidity is 0.5, that is, the spacing between the blades is

twice the chord length. The height of the rectangle is set such that the incoming velocity to the blade cascade is not affected by the static pressure increase in front of the cascade, so a margin of 4 to 5 chord length is left in the upstream of the cascade. Also 4 to 5 chord length distance is left in the downstream of the blades in order to avoid the affect of the boundary condition and to have a clear picture of the flow behind the cascade.

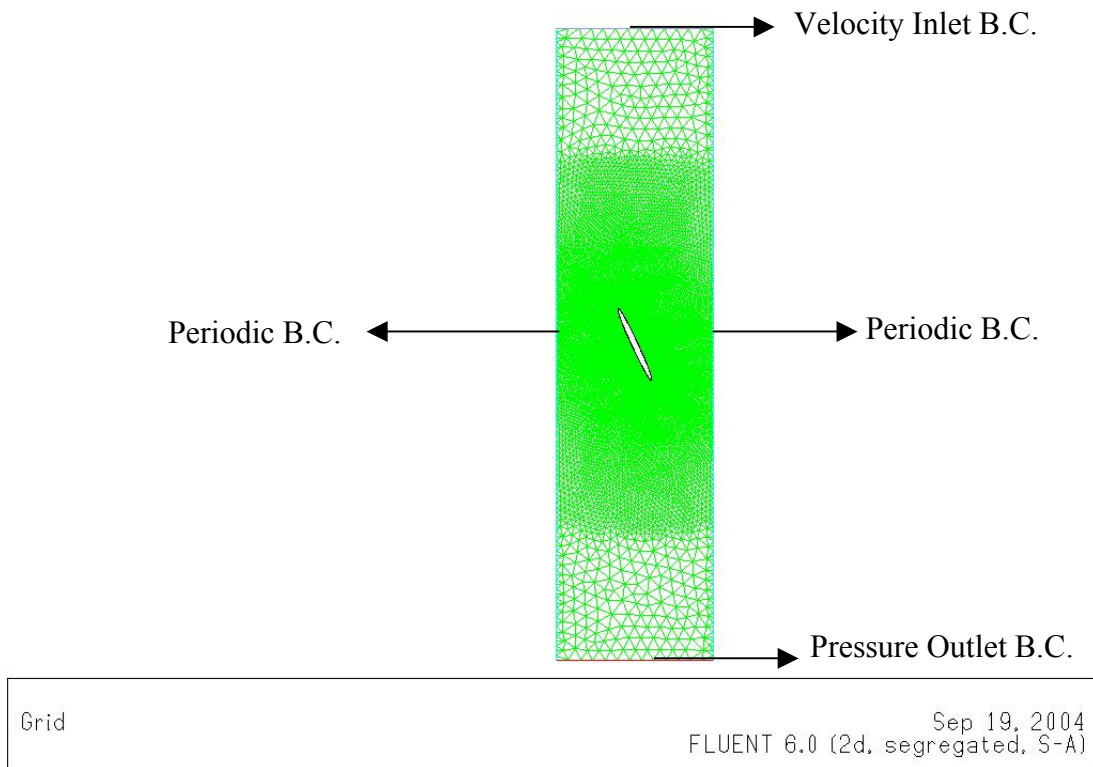


**Figure 2.4:** The boundary conditions (B.C.'s) of the computation.

Figure 2.4 presents the boundary conditions of the solution domain are given. The inlet edge of the rectangular domain is defined as velocity inlet boundary condition. The incoming velocities to the cascade are defined by describing the velocity magnitude and direction in this edge. Describing different velocity magnitudes in this boundary condition enables the user to have the performances of the blades for different working rotational speeds of the fan. The other described parameters are the turbulence intensity and hydraulic diameter at the section. The turbulence level at the

entrance is assumed as 5% of the mean velocity, which is a moderate intensity level, taking the effects of the ducting in front of the blades of the fan into account. Hydraulic diameter is the length of the edge describing the velocity inlet boundary condition. The FLUENT has the following form for the velocity inlet boundary condition description.

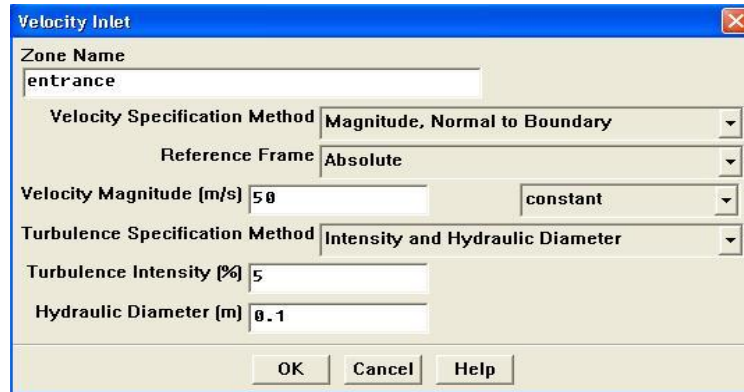


**Figure 2.5:** Velocity inlet B.C. panel in Fluent 6.0.

The outlet of the rectangular domain is defined as pressure outlet boundary condition. In this boundary condition, the pressure is defined as atmospheric, i.e. zero gage pressure. The other specified parameters are backflow turbulence intensity and backflow hydraulic diameter. In this case, 10% turbulence intensity is specified due to high turbulence at the downstream section. The form for pressure outlet boundary condition is given in Figure 2.6.

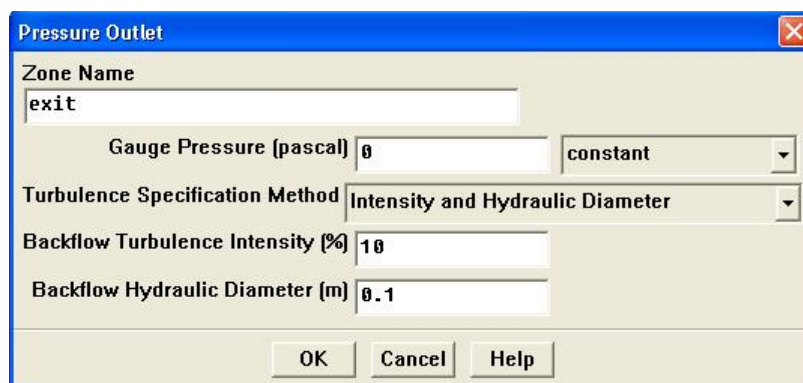


**Figure 2.6:** Pressure outlet B.C. in Fluent 6.0.

In order to construct an infinite cascade, free from the effects of the wall that surrounds the blades, periodic boundary conditions are specified for the side edges of the rectangular domain. The periodic zone between the periodic interfaces are repeated infinitely with pressure gradients across the interfaces are zero. The pressure information in the periodic edge is added to the neighboring periodic interface to reach the solution. Figure 2.7 shows the periodic interfaces and periodic zones in the solution domain with three periodic repeats.

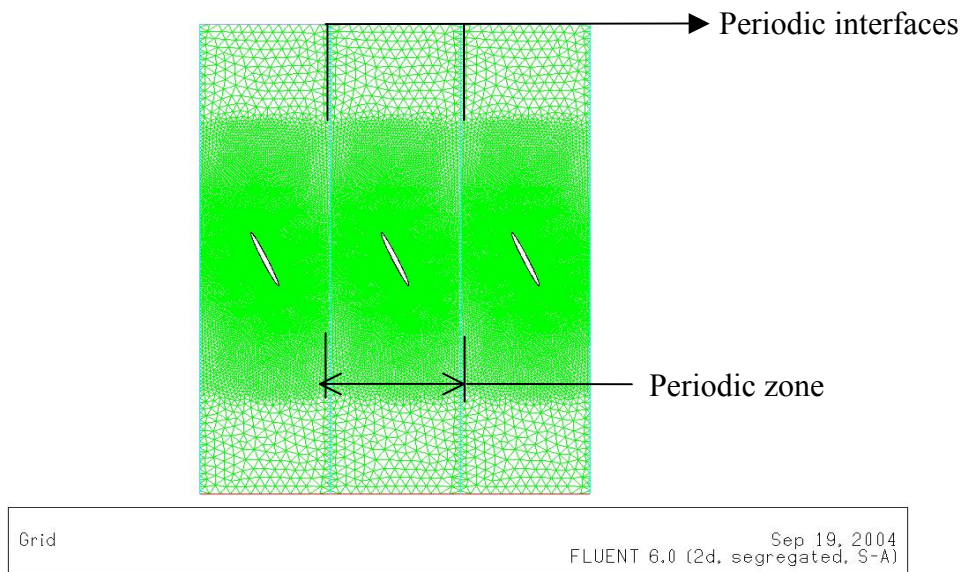


**Figure 2.7:** Periodic interfaces, periodic zone and three periodic repeat of the solution domain.

In order to reach acceptable solutions in computational fluid dynamics, the mesh intensity should be high enough. What is meant by the high mesh intensity is that, the critical parts of the modeled domain should accommodate enough number of cells so that a reasonable solution can be reached. For instance, high-pressure gradient areas should be densely populated with computational nodes and cells in order to minimize the errors coming from the space discretization. The errors due to space discretization are less pronounced in the areas of low gradients, so a coarser grid structure can be used. Gambit 2.0, the pre-processor of FLUENT 6.0, has the

option to apply finer mesh in the vicinity of a specified zone, which is the neighborhood of the blades in cascade analysis, and coarsen the grid in the regions where lower number of cells are enough to get an accurate solution. As it is seen in Figure 2.4 and Figure 2.7, the computational grid is very fine in the vicinity of the blades where there is much turbulence and strong pressure gradients, while the mesh is much coarser in the inlet section and outlet section of the domain where the flow is more relaxed.

Figure 2.8 (a) to (e) shows the other solution domains for different solidities of the cascades.

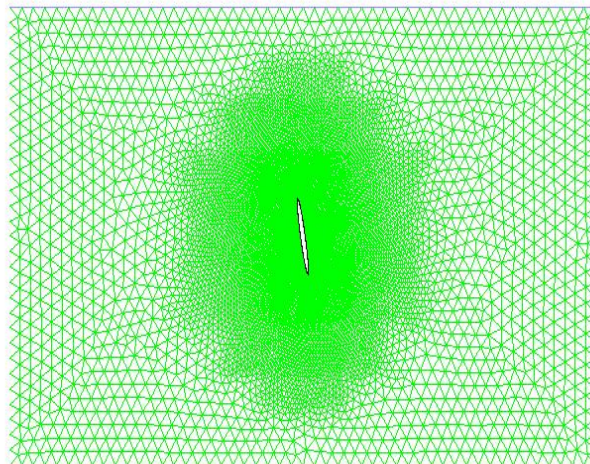
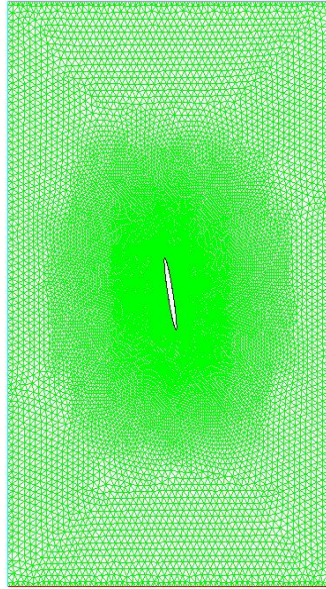


**Figure 2.8 (a):** The solution domain for  $\sigma = 0.1$ ,  $i=10^\circ$



Grid

Sep 20, 2004  
FLUENT 6.0 (2d, segregated, S-A)

**Figure 2.8 (b):** The solution domain for  $\sigma = 0.2$ ,  $i=10^\circ$



Grid

Sep 20, 2004  
FLUENT 6.0 (2d, segregated, sstk)

**Figure 2.8 (c):** The solution domain for  $\sigma = 1$ ,  $i=10^\circ$

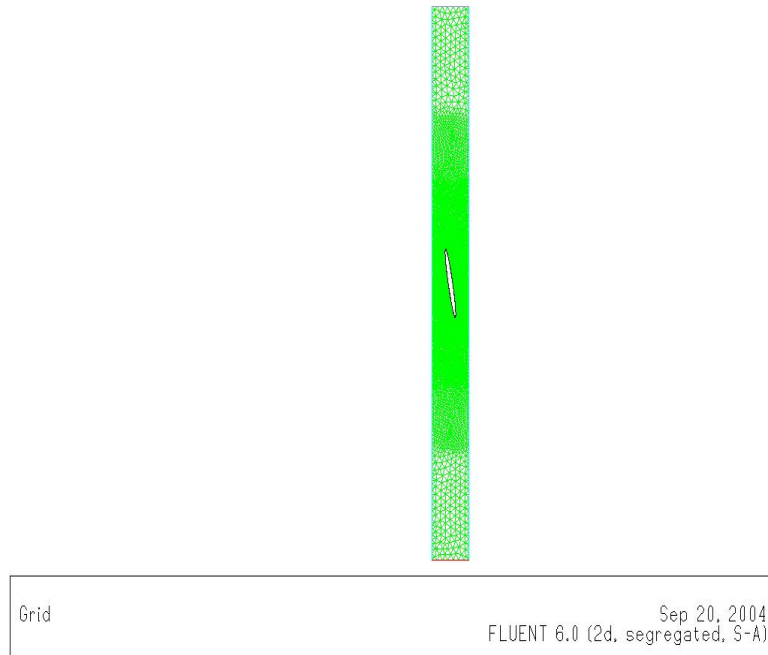


**Figure 2.8 (d):** The solution domain for  $\sigma = 1.5$ ,  $i=10^\circ$

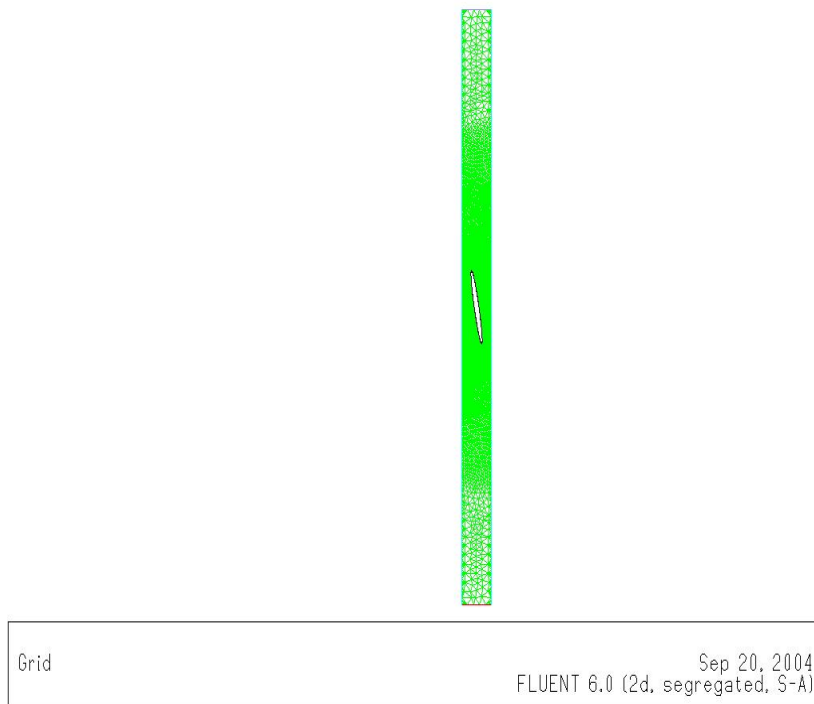


**Figure 2.8 (e):** The solution domain for  $\sigma = 2$ ,  $i=10^\circ$

## 2.4. Solution of the Blade Cascades

The results are obtained with the solution of the continuity, N-S equations along with the equations for the selected turbulence model. In this phase of the study, Spalart-Allmaras model is selected as the turbulence model. Modeling the turbulent viscosity with one equation, this model is specifically designed for flows with strong adverse pressure gradients and aerodynamic applications. The details of the model can be found in Chapter 1.

After the boundary conditions are specified and the solution models are selected, the iterations are performed in FLUENT. The point when to stop the iterations are determined by setting a convergence criteria for the variables that are computed, velocities in three directions, the continuity equation and the variable for the turbulence model. In most cases, the convergence criterion is set such that the difference between two successive iterations, residuals, are three to four orders of magnitude lower than the initial value. The solutions for the blade cascades are obtained with this criterion. During the solutions, iteration history is also checked for the stability and the trend of the residual curves. Figure 2.9 shows a typical convergence history graph of the solutions obtained for the blade cascades. It is seen from the figure that the residuals for the variables are decreased to at least four orders of magnitude and a stable trend is reached at the end. The convergence histories of other solution variables like lift and drag coefficients are also monitored to decide whether a reasonable solution is reached or not.

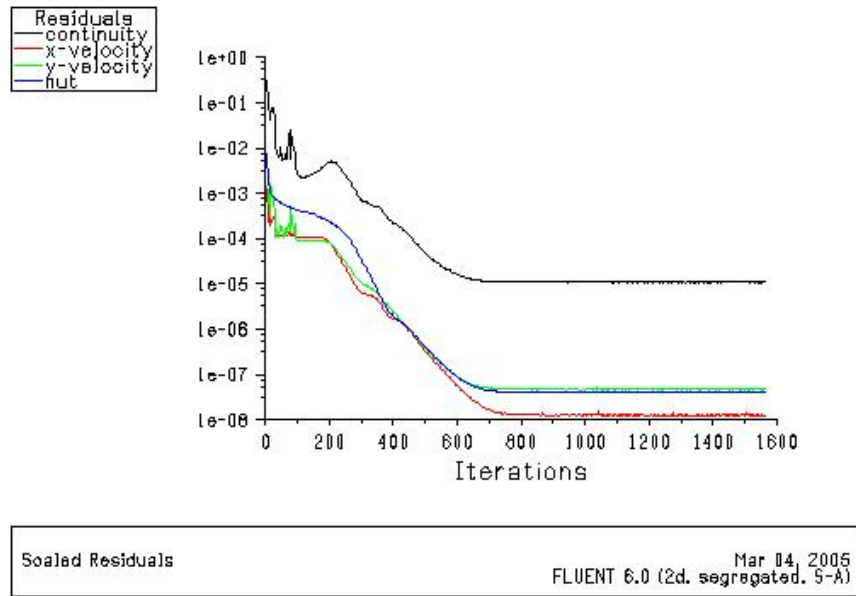


**Figure 2.9:** Convergence history graph for  $\sigma = 1.5$ ,  $i = 10^0$  for 30m/s velocity.

The net force on the blade cascades is due to the static pressure difference between the suction and pressure sides of the airfoils and due to total skin friction along the sides of the blades. Fluent program enables the user to compute these forces exerted on the blades due to the fluid flow in prescribed directions. The direction where the flow enters to solution domain is defined as y direction and the direction where the blades are located side by side is x direction. The coordinate axes defined on the model are shown in Figure 2.10.

To obtain the flow direction at the downstream of the cascade, a section should be defined. By the definition of this section, one can get the velocity magnitudes in the section from Fluent and calculate the flow direction, i.e.  $\beta_2$  angle. The experiments carried out to measure the cascade performances suggest that the measuring section should be approximately one chord length away from the trailing edges of the blades. Therefore, a measuring section is placed one chord length away from the cascade (Figure 2.10)

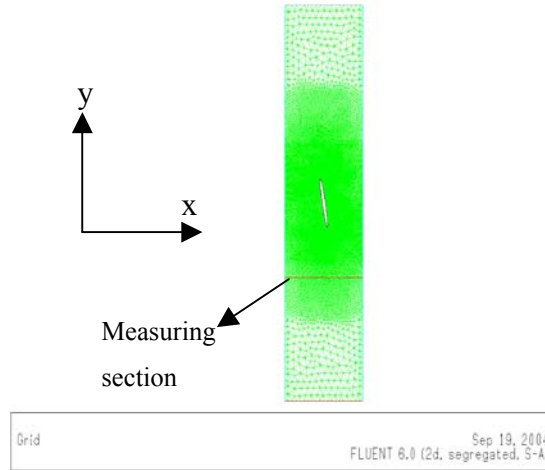


**Figure 2.10:** The coordinate axes and the measuring section one chord length away from the cascade.

The mean flow direction around the cascade is obtained by the help of the velocity components computed in measuring section and utilizing Equations (54) and (55).

To compute the flow direction, velocities in x direction must be known. Fluent can give these values by averaging them along this section. Figure 2.11 is a sample plot of these x velocities.

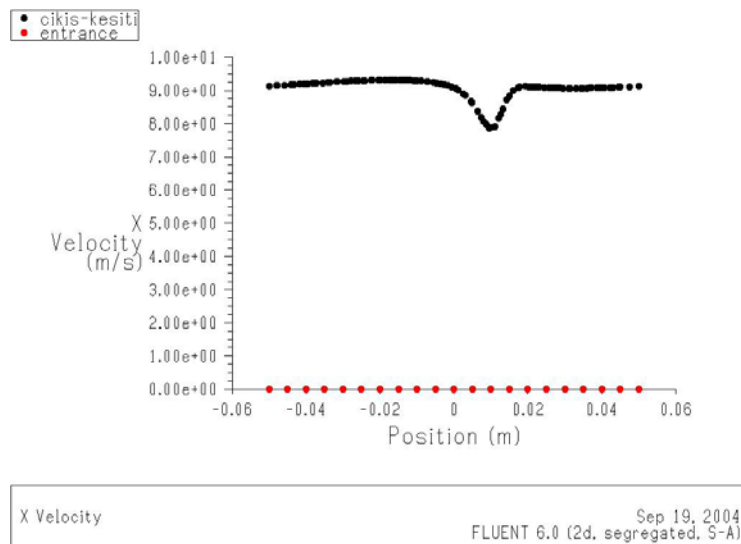


**Figure 2.11:** Velocities in x direction at one chord downstream.

Once the solution is obtained around the cascade, various properties of the flow can be monitored like total pressure contours, velocity vectors, stream functions to get a better insight through the flow field. The following figures are samples of these properties.

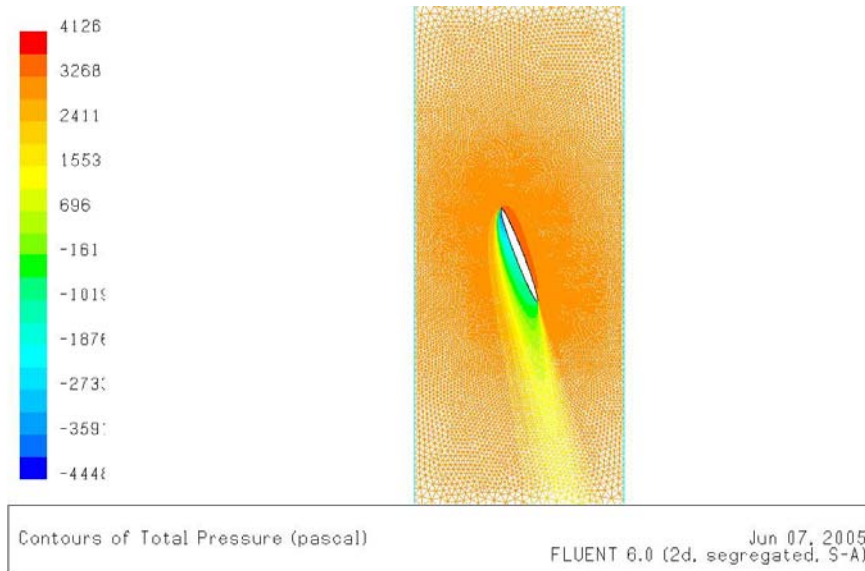


**Figure 2.12:** Total pressure distribution ( $\sigma = 0.5$ ,  $i = 20^\circ$   $V = 70$  m/s)

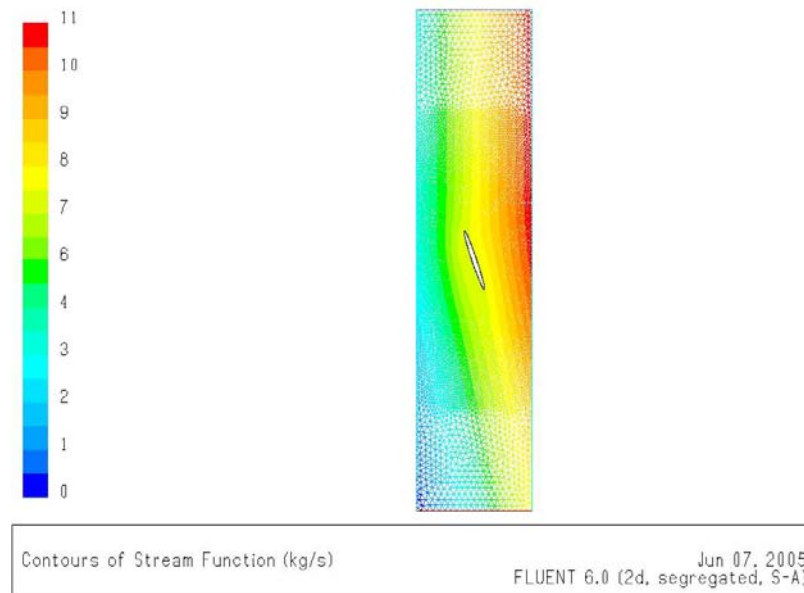


**Figure 2.13:** Contours of stream function ( $\sigma = 0.5$ ,  $i = 20^\circ$   $V = 70$  m/s)



**Figure 2.14:** Velocity vectors of the overall field ( $\sigma = 1.5$ ,  $i=30^\circ$ ,  $V=70$  m/s)

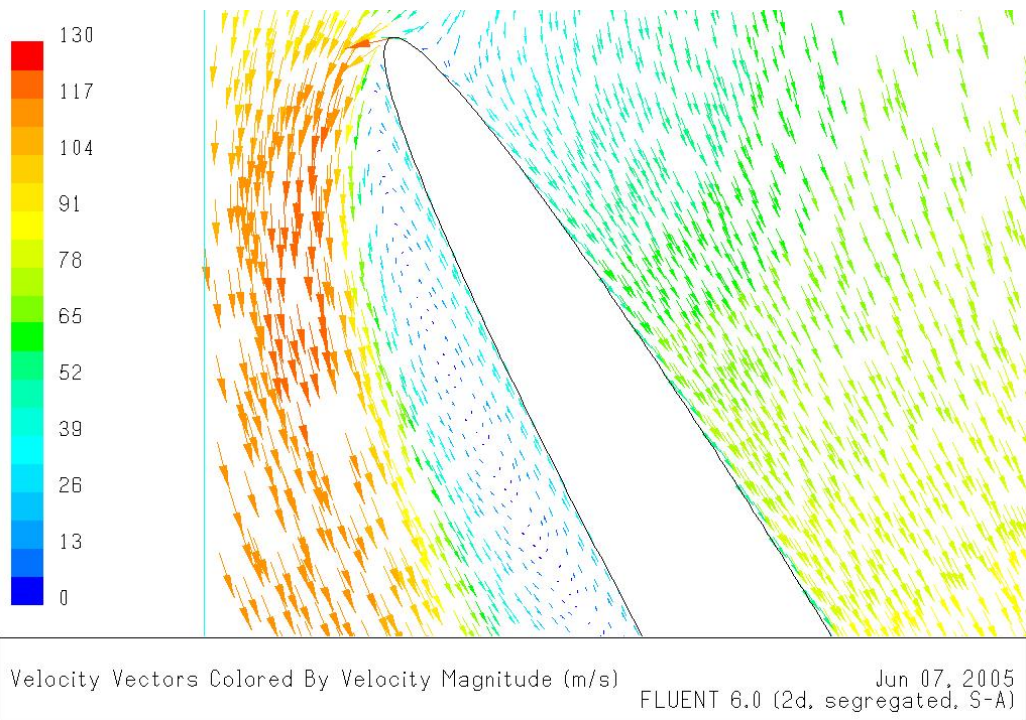
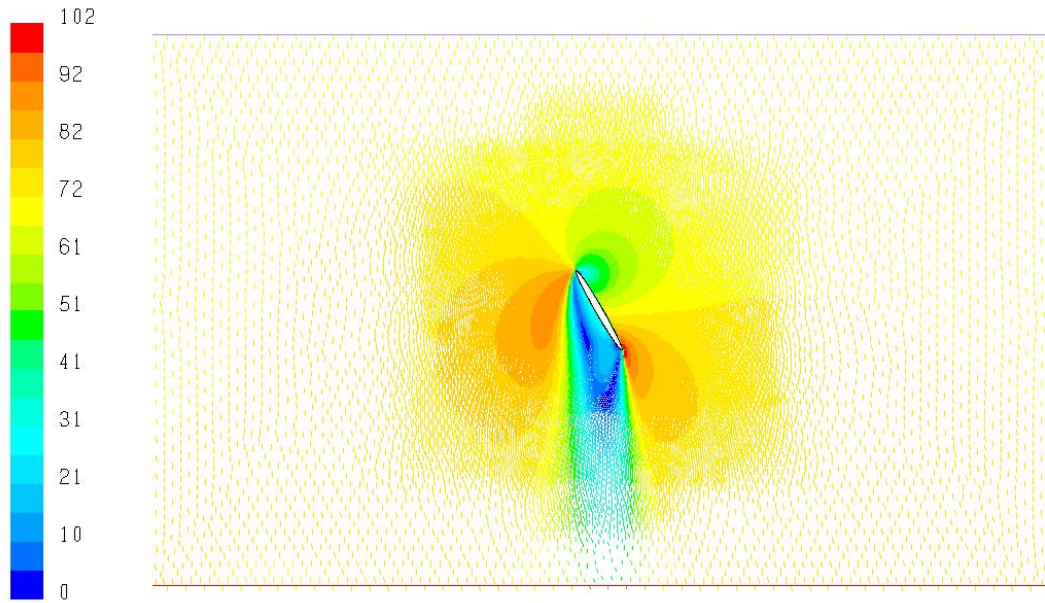
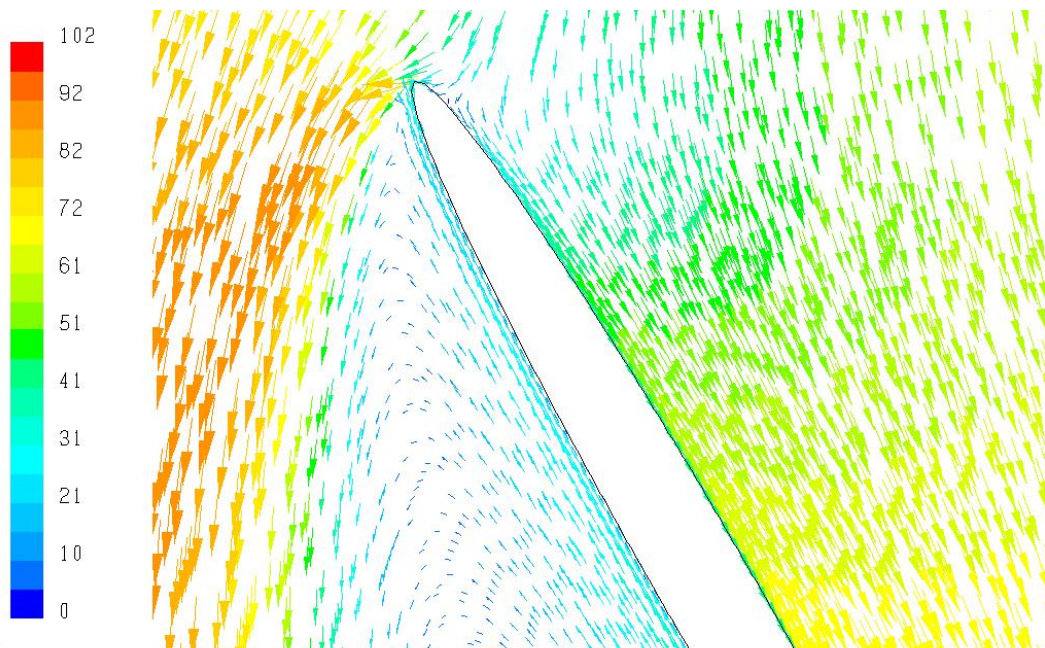


**Figure 2.15:** Detail of velocity vectors at leading edge ( $\sigma = 1.5$ ,  $i=30^\circ$ ,  $V=70$  m/s)



Velocity Vectors Colored By Velocity Magnitude (m/s) Jun 07, 2005  
FLUENT 6.0 (2d, segregated, S-A)

**Figure 2.16:** Velocity vectors of the overall field ( $\sigma = 0.1$ ,  $i=30^\circ$ ,  $V=70$  m/s)



Velocity Vectors Colored By Velocity Magnitude (m/s) Jun 07, 2005  
FLUENT 6.0 (2d, segregated, S-A)

**Figure 2.17:** Detail of velocity vectors at leading edge ( $\sigma = 0.1$ ,  $i=30^\circ$ ,  $V=70$  m/s)

The figures 2.14 to 2.17 show the velocity vectors around the blade cascades of solidities  $\sigma = 1.5$  and  $\sigma = 0.1$  in the overall field and in the vicinity of leading edges where flow separation occurs. When the vectors are investigated carefully, it is seen that the flow separation occurs drastically at low solidity. Furthermore, the flow reattachment is observed at high solidity due to the effects of the neighboring blades. The effect of the neighboring blades is more pronounced in high solidities because of narrower flow passages between the blades. This effect can also be observed by looking at the static pressure distributions on the blade surfaces. Figures 2.18 and 2.19 demonstrates the static pressure distribution on the blade surfaces for the solidities of  $\sigma = 1.5$  and  $\sigma = 0.1$ .

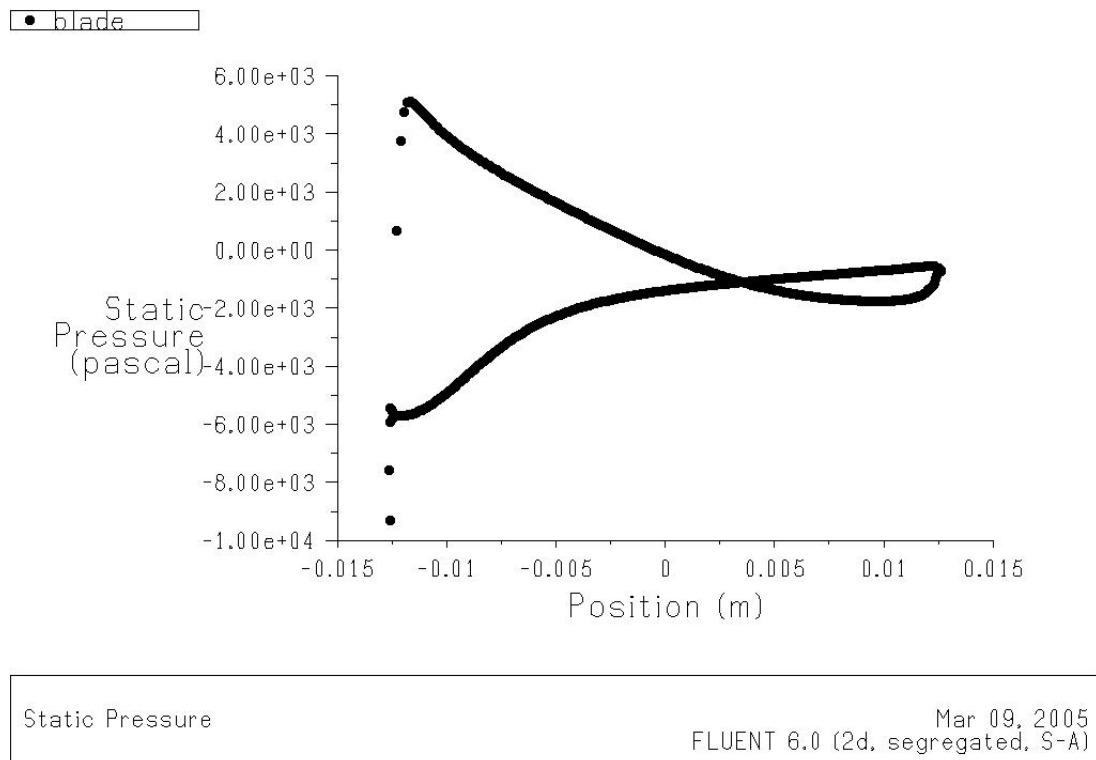


**Figure 2.18:** Static pressure distribution on the blades with  $\sigma = 1.5$

In Figure 2.18, the below line shows the suction side and above line shows the pressure side of the blade. As expected, a favorable pressure gradient is observed in the pressure side. The suction side pressure distribution curve has a constant trend at

the beginning, followed by a trend with an adverse pressure gradient section. This is interpreted as flow separation occurs just after the leading edge in the suction side and thus no pressure gradient is observed in this portion because the pressure at this portion is equal to the pressure of the point where the separation just took place. But the effect of neighboring blades causes the flow to reattach the surface, thus an adverse pressure gradient portion is observed because of the diverging flow passage.

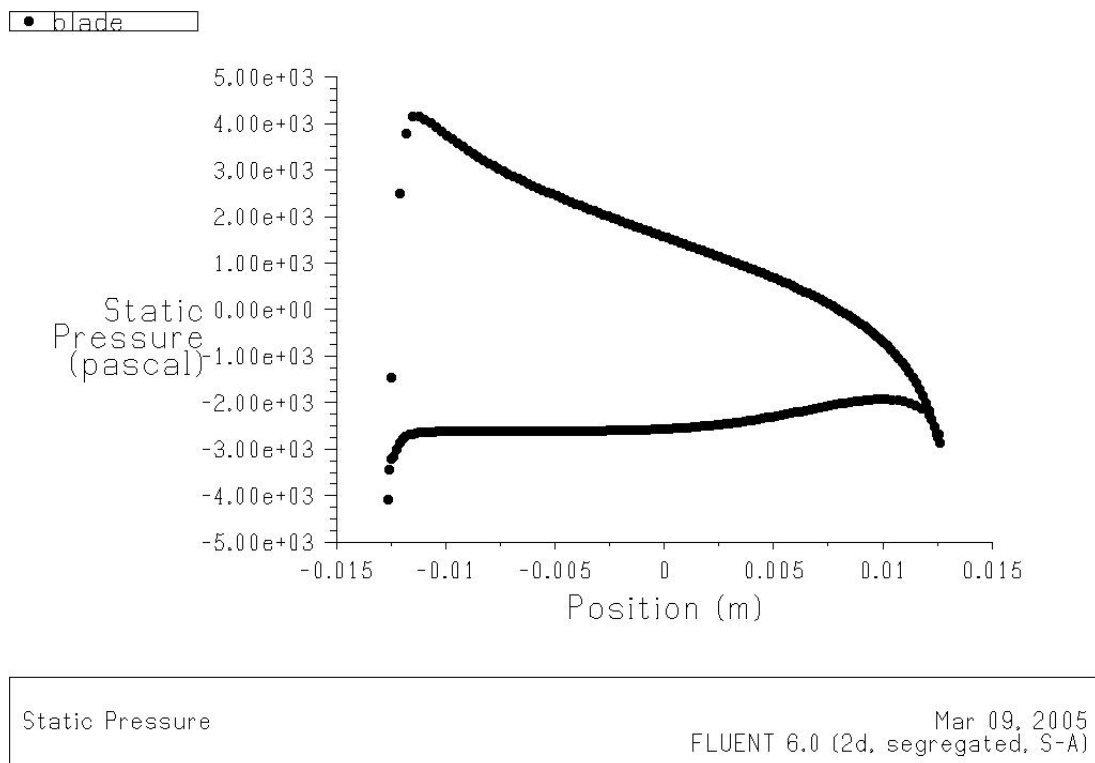


**Figure 2.19:** Static pressure distribution on the blades with  $\sigma = 0.1$

Figure 2.19 shows the static pressure distribution on the blades with  $\sigma = 0.1$ . The distinction between this and the former case is the length of constant trend portion of the suction side curve. In this case, no reattachment is observed after the flow separation because of low solidity blading.

Besides the forces exerted on the given surfaces, FLUENT also calculates the lift and drag coefficients if the reference area, which is the projected wing area in airfoil applications, and the reference velocity are indicated. In the calculations of lift and drag coefficients within FLUENT, the reference area is indicated as the projected wing area, which is chord length times the span of the blade, but the velocity at the upstream of the cascade is referenced. Then the obtained drag and lift coefficients are modified for the mean velocity direction and mean velocity magnitude because of the definitions given in Equation (56) and Figure 2.2. L and D forces are also computed for the mean flow direction, rather than the major coordinate axes directions. Sample results of the analysis are given in Table 2.1 for  $\sigma = 0.5$  and incoming velocity of  $V = 70$  m/s.

**Table 2.1:** Aerodynamic coefficients in X-Y directions and their reduction to mean velocity direction

		The Coefficients in X-Y direction		Measuring section parameters			Mean Velocity Properties		Projection of the coefficients on mean velocity direction		
		Lift Coeff.	Drag Coeff.	Y velocity (m/s)	X velocity (m/s)	Velocity Direction (°)	Direction (°)	Magnitude (m/s)	Lift Coeff.	Drag Coeff.	L/D
<b>Velocity = 70 m/s</b>	<b>0 deg</b>	0,000	0,025	70,0	0,0	0,0	0,0	70,0	0,000	0,025	0,000
	<b>5 deg</b>	0,264	0,041	70,0	4,6	3,8	1,9	70,0	0,265	0,032	8,218
	<b>10 deg</b>	0,519	0,090	70,0	9,1	7,4	3,7	70,1	0,522	0,056	9,316
	<b>15 deg</b>	0,718	0,174	70,0	12,6	10,2	5,1	70,3	0,725	0,108	6,698
	<b>20 deg</b>	0,896	0,329	70,0	15,6	12,6	6,4	70,4	0,916	0,225	4,072
	<b>25 deg</b>	1,034	0,533	70,0	17,9	14,4	7,3	70,6	1,076	0,391	2,751
	<b>30 deg</b>	1,180	0,756	70,0	20,4	16,2	8,3	70,7	1,250	0,566	2,209

The X and Y velocity magnitudes in measuring section part of Table 1 refer to  $W_{\theta_2}$  and  $V_a$  in Figure 2.1, respectively. As it is noted before,  $W_{\theta_2}$  is the tangential component of the relative velocity at the exit of the cascade and  $V_a$  is the axial component of the velocity. The velocity direction in measuring section refers to angle  $\beta_2$  in Figure 2.1. Mean velocity and mean velocity direction refer to  $V_\infty$  and  $\beta_\infty$  in Figure 2.2, respectively.

The aerodynamic parameters are obtained with different incoming velocities and solidities by changing angle of attack. The following graphs are the representations of aerodynamic parameters at  $V=70$  m/s incoming velocity. The graphs include different solidities for axial fan design considerations. These graphs are obtained for incoming velocities of 10 m/s, 30 m/s, 50 m/s, 70 m/s and 100 m/s to utilize the corresponding coefficients in the design phase of different radial positions of the fan rotor.

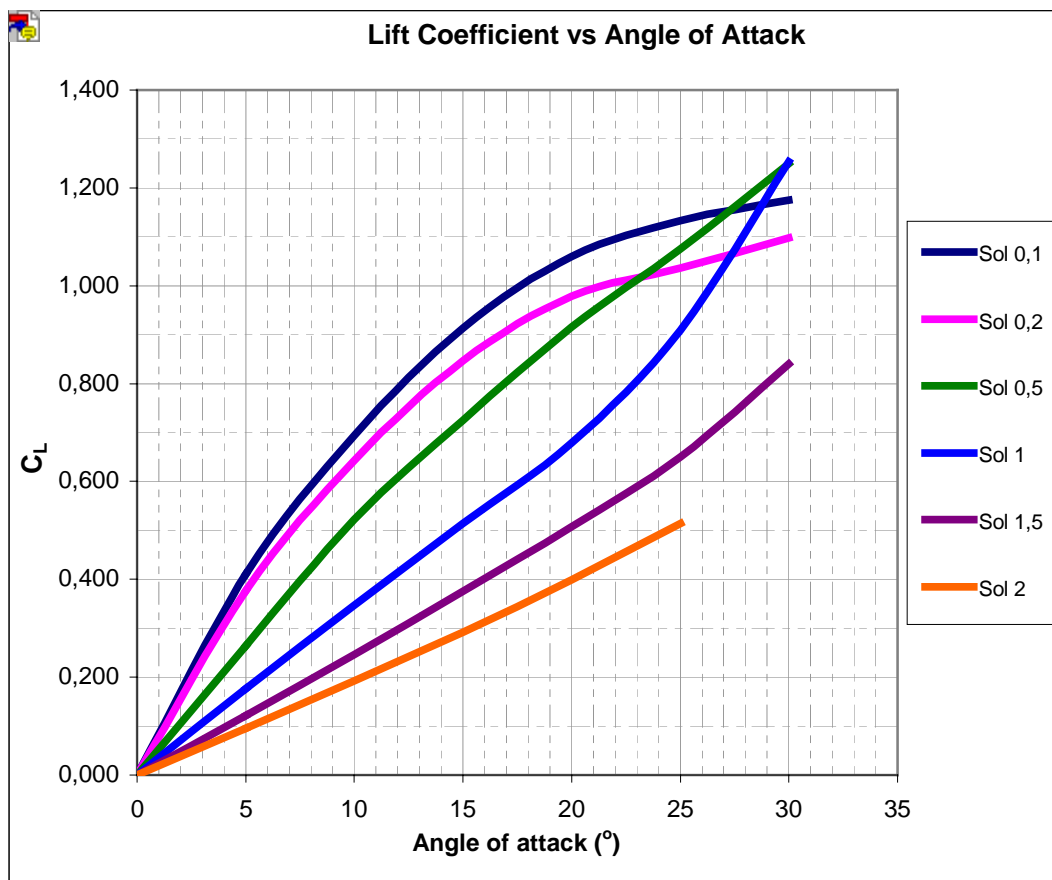


**Figure 2.20:** Lift coefficient vs. angle of attack at different solidities ( $V=70$ m/s).

From Figure 2.20, it can be concluded that lift coefficient is affected adversely with increase in solidity. This is because the net force on the blades is reduced when this volume between them is decreased with increase in solidity, i.e. the total force

decreases with a decrease in the area that it applies. Another reason is the effect of neighboring blades. At increased solidities, high-pressure side of the neighboring blade is closer to the low-pressure side (suction) of other blade than that of the blade located at a lower solidity. The high pressure in the vicinity of the suction side of the blade results in a decrease on the pressure difference across the blades.

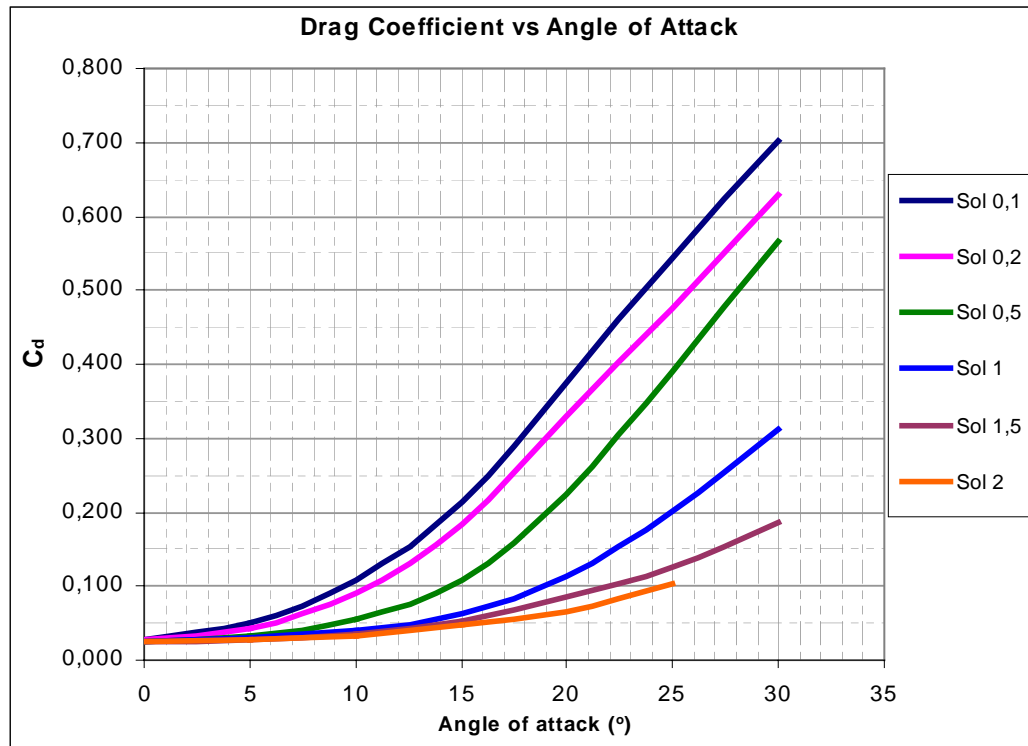


**Figure 2.21:** Drag coefficient vs. angle of attack at different solidities ( $V=70$  m/s).

In the graph for drag coefficient vs. angle of attack, a similar behavior is observed as lift coefficient curve. The drag force decreases as the solidity increases because the positive pressures occurring due to the pressure side of the neighboring blade result in a reduced net force on the blades along the flow direction. As the solidity decreases, the blades start to behave more like single blades. These cases are as if one blade is located in a flow stream. As Figure 2.20 is investigated carefully, the lift curves for low solidity are like those of single blades located in a free stream, in the

manner that the rate of increase of the lift coefficients decreases as the angle of attack increases.

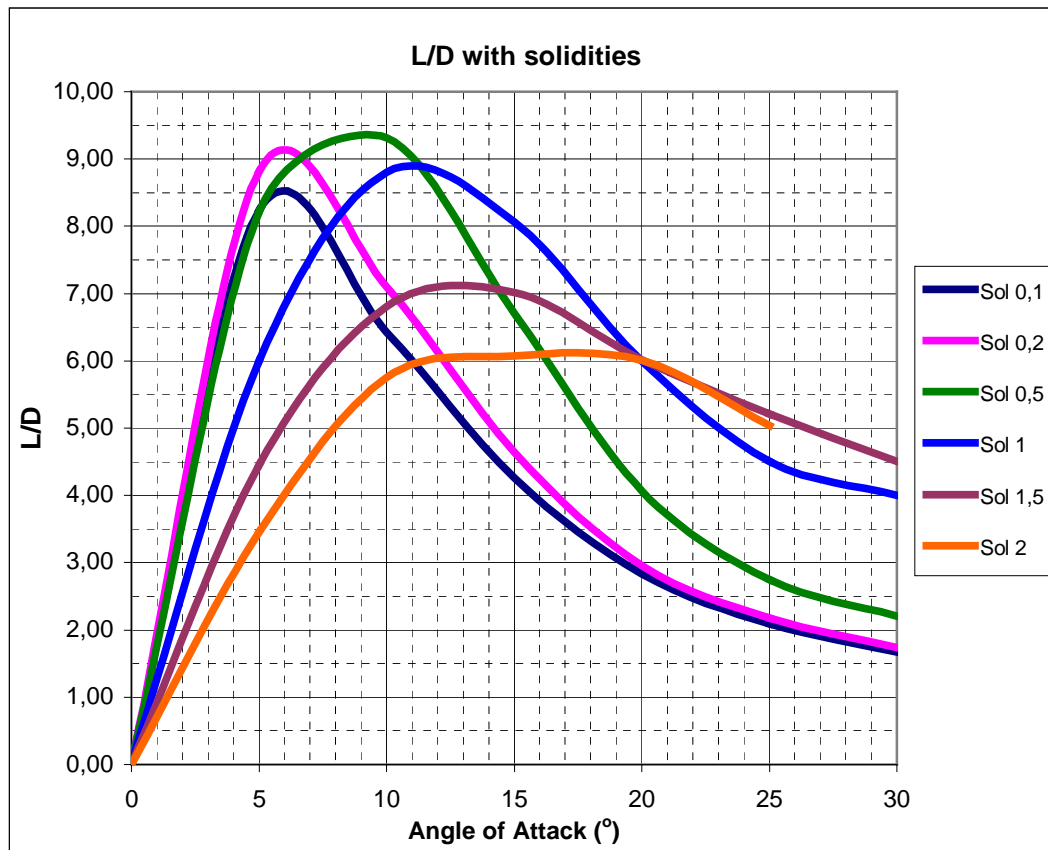


**Figure 2.22:** L/D vs. angle of attack at different solidities ( $V=70$  m/s).

Figure 2.22 displays the ratio of the lift forces to drag forces as the angle of attack increases at different solidities. It can be concluded from the graph that for elliptical airfoils that are tested, the optimum solidity is around 0.5 and the operating angle of attacks are around  $10^\circ$ .

## CHAPTER 3

### AERODYNAMIC DESIGN OF THE REVERSIBLE AXIAL FLOW FAN

#### 3.1. Introduction

The first thing to begin the aerodynamic design of an axial turbomachinery is to specify the design parameters, which are volumetric flowrate, the total pressure or head rise and the rotational speed. In the sample design shown here, design parameters for the reversible axial flow fans that are used in the emergency ventilation of underground transportation systems are used [28]. The parameters used are 532 Pa (50m of air) total pressure rise, 80 m<sup>3</sup>/s volumetric flowrate and 1000 rpm rotational velocity. Before starting the design, the ratio of the hub diameter to outer diameter is to be fixed. In the design, a hub to tip ratio of 0.4 is selected, as it is a typical value for emergency ventilation fans. A large hub to tip diameter ratio is avoided in order not to have deep stalling dips in fan performance curves. Deep stalling dips cause instable operation of the fan i.e. abrupt changes in flowrate, although flow resistances change insignificantly, which is the case for fans having large hub to tip ratios [24,26]. The number of blades in the rotor is also specified at the beginning as 7, within the range 5 to 12, which is the recommended range for axial fans [24].

The preferred design style for the rotor blades is “free vortex design”, which dictates that the total pressure rise across the blade from hub to tip is constant. The developed methodology will be repeated for different solidity ratios, and the solidity giving the best hydraulic efficiency will be selected for that radial distance from the axis. The

methodology will also be repeated for hub, mean and outer diameter of the fan to get the blade twist.

### 3.2. Selection of Outer Diameter

The outer diameter of the fan is selected by applying the methodology of ECK [26] that is developed for the selection of optimum diameter for fans having different configurations and design parameters. He used the specific speed ( $N_s$ ), including rotational speed ( $N$ ) in [rps], volumetric flowrate ( $Q$ ) in [ $m^3/s$ ] and head rise ( $H$ ) in [m], that is,

$$N_s = 0.379 \times N \times \sqrt[4]{\frac{Q^2}{H^3}} \dots\dots\dots(58)$$

For the present case, the specific speed is

$$N_s = 0.379 \times N \times \sqrt[4]{\frac{Q^2}{H^3}} = 0.379 \times 1000 \frac{1}{60} \times \sqrt[4]{\frac{80^2}{50^3}} = 3.005$$

After the specific speed is calculated, specific diameter ( $N_D$ ) is read from the graph given in Figure 3.1.

Note that specific speed is designated by  $\sigma_{opt}$  and specific diameter is designated by  $\delta_{opt}$  in Figure 3.1.

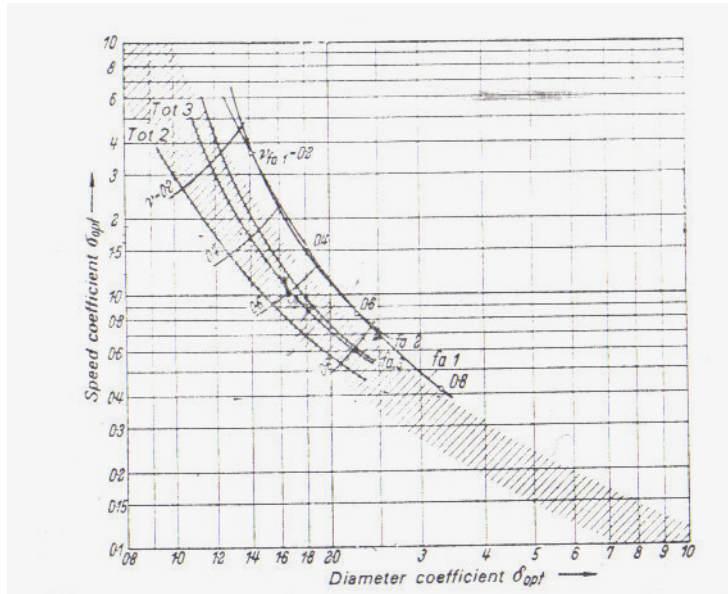


**Figure 3.1:** Optimum curves with minimal hub ratios for different methods of installation for impellers with low characteristics [26].

The specific diameter  $N_D$  is

$$N_D = 1.2$$

Blade loading coefficient ( $\psi$ ) is calculated using  $N_S$  and  $N_D$ .

$$\psi = \frac{1}{N_S^2 \times N_D^2} = \frac{1}{3.005^2 \times 1.2^2} = 0.077$$

Using this coefficient, the expression for diameter can be calculated as follows

$$D_{fan} = \frac{60}{\pi N} \sqrt{\frac{16\rho H}{\psi}} \dots\dots\dots(59)$$

$$D_{fan} = 2.029m$$

So outer diameter is selected. This value is also checked for typical emergency ventilation fans. The ranges for outer diameters in ventilation fans vary between 1.75 meters to 2.25 meters according to the capacities. So the selected diameter here is within the recommended range.

### 3.3. Design Basis and Assumptions

The design procedure is based on the method given in reference [27] but design procedure is modified to account for the particular reversible fan case. The point that needs to be highlighted for the modification is given during the design methodology. As it is previously mentioned, the design of the fan blades is decided to be “free vortex flow” type. This kind of design imposes no radial velocity component across the blade. Two sufficient conditions for achieving this type of flow involve a design assumption where both the theoretical total pressure rise and the axial velocity component are constant with changing radius. The absence of radial flow will ensure constancy of axial velocity component throughout the annulus.

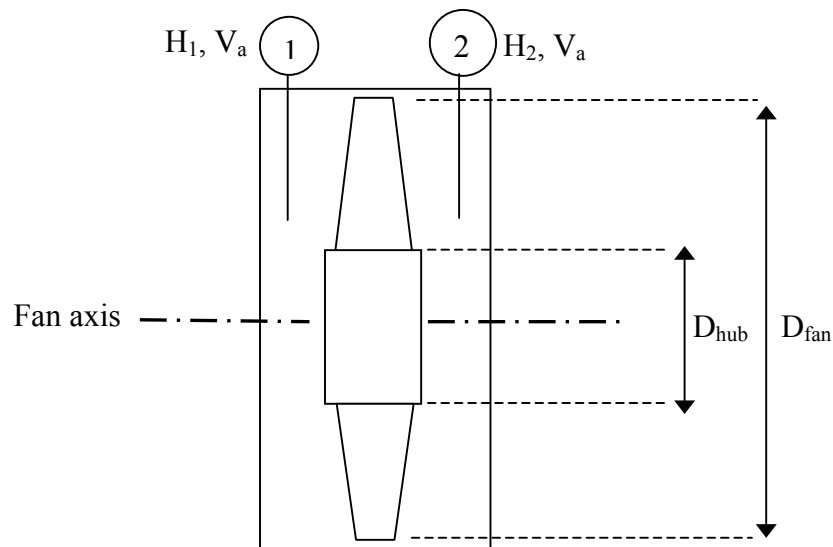


**Figure 3.2:** Fan configuration giving definitions of diameters and reference planes.

### 3.4. Design Procedure

The design starts with calculation of the axial velocity through the fan. Knowing the flowrate ( $Q$ ), outer diameter ( $D_{fan}$ ) and the hub diameter ( $D_{hub}$ ) of the fan,

$$V_a = \frac{Q}{\frac{\pi}{4} \times (D_{fan}^2 - D_{hub}^2)} \dots\dots\dots(60)$$

where  $D_{hub}$  can be calculated knowing the hub to tip ratio ( $x_b$ ), which is 0.4 in this case.

$$D_{hub} = D_{fan} \times x_b \dots\dots\dots(61)$$

In Figure 3.2, inlet and exit planes are indicated as 1 and 2, respectively.  $H_1$  and  $H_2$  are the total pressures in these sections and their difference is equal to the difference of theoretical pressure rise across the rotor ( $\Delta H_{th}$ ) and the losses due to the rotor itself ( $\Delta h_{rotor}$ ), that is,

$$H_2 - H_1 = \Delta H_{th} - \Delta h_{rotor} \dots\dots\dots(62)$$

Nondimensional form of this equation is obtained by dividing the terms by dynamic pressure based on the axial velocity  $V_a$ .

$$\frac{H_2 - H_1}{\frac{1}{2} \rho V_a^2} = \Psi_{fan} = \Psi_{th} - \Psi_{rotor} \dots\dots\dots(63)$$

$\Psi_{fan}$  is the design pressure rise across the fan while  $\Psi_{th}$  is the theoretical non-dimensional pressure rise and  $\Psi_{rotor}$  is the rotor loss coefficient and are described as

$$\Psi_{th} = \frac{H_{2th} - H_{1th}}{\frac{1}{2}\rho V_a^2} \quad \text{and} \quad \Psi_{rotor} = \frac{\Delta h_{rotor}}{\frac{1}{2}\rho V_a^2} \dots\dots\dots(64)$$

Before constructing the flow and blade angles, one should account for the rotor losses and put a margin on the rotor pressure rise term, which is the left hand side of Eq(63), where the concept of efficiency is introduced. To get the desired pressure rise across the fan ( $\Psi_{fan}$ ), the theoretical pressure rise term ( $\Psi_{th}$ ) should be used to construct the flow angles, which accounts for the losses. Dividing Eq. (63) by  $\Psi_{th}$  gives the blade efficiency, that is

$$\eta_{BL} = \frac{\Psi_{fan}}{\Psi_{th}} = 1 - \frac{\Psi_{rotor}}{\Psi_{th}} \dots\dots\dots(65)$$

At the beginning, because rotor losses are not known, efficiency value is assumed to obtain  $\Psi_{th}$  from  $\Psi_{fan}$ . Later in the design, this efficiency will be calculated and checked for convergence. It is also worth noting that this efficiency is not related to hydraulic efficiency of the fan, but only a measure of the effectiveness of the blading due to rotor losses.

After having the nondimensional theoretical pressure rise and the axial velocities, flow coefficient ( $\phi$ ) can be calculated. It is defined as the ratio of the axial velocity through the fan to the rotational velocity.

$$\phi = \frac{V_a}{N \frac{2\pi}{60} \times \frac{D}{2}} \dots\dots\dots(66)$$

The swirl coefficients at the inlet and exit of the rotor ( $\varepsilon_1, \varepsilon_2$ ) are calculated. The swirl coefficients are measures of the tangential velocities at the inlet and exit planes of the rotor.

$$\varepsilon = \frac{V_\theta}{V_a} \dots\dots\dots(67)$$

A swirl free inlet is assumed so,

$$\varepsilon_1 = 0 \dots\dots\dots(68)$$

In turbomachinery applications, the pressure rise is determined by the Euler equation, which is

$$\Delta H_{th} = \rho u (\Delta V_\theta) \dots\dots\dots(69)$$

Adapting the formula to current nondimensional coefficients and swirl free inlet condition, swirl coefficient is obtained at the exit of the rotor.

$$\varepsilon_2 = \frac{\Psi_{th} \times \phi}{2} \dots\dots\dots(70)$$

Knowing the flow coefficients and swirl coefficients at the inlet and exit, the flow angles can be constructed.

The relative flow angle at the inlet ( $\beta_1$ ), at the exit ( $\beta_2$ ) and mean flow angle are calculated as follows

$$\beta_1 = \arctan\left(\frac{1}{\phi}\right) \dots\dots\dots(71)$$

$$\beta_2 = \arctan\left(\frac{(1 - \varepsilon \times \phi)}{\phi}\right) \dots\dots\dots(72)$$

$$\beta_m = \arctan\left(\frac{\tan \beta_2 + \tan \beta_1}{2}\right) \dots\dots\dots(73)$$

After the flow angles are determined, the blade angles should be set ( $\beta_{1v}$ ,  $\beta_{2v}$ ). Here lies the key point of the design where the blade angles to be set are iterated using the incidence and deviation angles. As profiling of the blade is not allowed due to reversibility considerations, necessary deflection of the flow is obtained by relating the flow angle to the blade angle at the exit of the rotor, which the information is acquired from the two-dimensional analysis at given solidity. As a first step, the incidence angle is obtained from the difference of flow angles at the inlet and exit, that is

$$i = \beta_1 - \beta_2 \dots\dots\dots(74)$$

Getting the deviation angle values corresponding to this incidence angle from two-dimensional analysis for the analyzed solidity,  $\beta_{2v}$  is determined. Furthermore, setting  $\beta_{2v}$  puts a restriction on the inlet blade angle  $\beta_{1v}$ , because no camber is present on the blades. Thus, incidence angle should also be modified again for the modified settings of the blade (Figure 3.3).

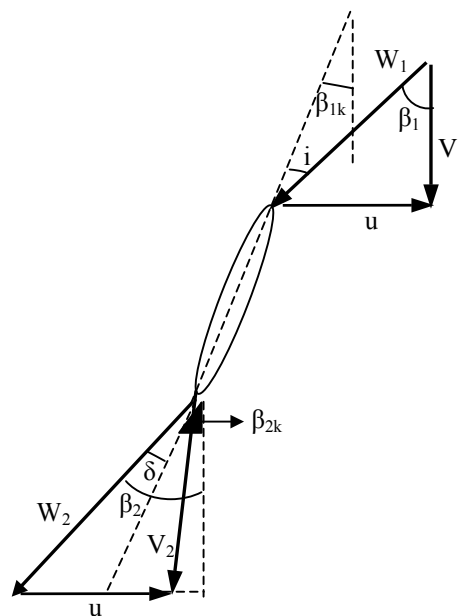


**Figure 3.3:** Flow triangles on the rotor

Sequentially,

$$\beta_{2k} = \beta_2 - \delta \dots\dots\dots(75)$$

$$\beta_{1k} = \beta_{2k} \dots\dots\dots(76)$$

$$i_{\text{mod}} = \beta_1 - \beta_{1k} \dots\dots\dots(77)$$

The incidence of the blades is determined using the deviation angle that corresponds to the given solidity and incidence in an iterative manner. After the modified incidence angle (Eq 77) is calculated, the deviation angle now differs from the one that is computed corresponding to the incidence angle obtained by Eq (74). Then, deviation angle corresponding to  $i_{\text{mod}}$  is obtained again to calculate new  $i_{\text{mod}}$ .

The aerodynamic parameters corresponding to the resulting incidence angle are obtained from the previously shown lift and drag coefficient curves for the desired solidity. But the drag coefficients obtained by two-dimensional analysis include only the profile drag, which is influenced by profile shape, blade solidity, Reynolds number and air turbulence. For the turbomachinery design, secondary drag and annulus drag should be included. Following equations are given in reference [34] and can be used for secondary losses and annulus losses, respectively.

$$C_{DS} = 0.018 \times C_L^2 \dots\dots\dots(78)$$

$$C_{DA} = 0.02 \times \frac{s}{h} \dots\dots\dots(79)$$

where  $s$  is the blade spacing and  $h$  is the blade height.

$$s = \frac{\pi \times D}{N_{\text{blade}}} \dots\dots\dots(80)$$

$$h = \frac{D_{fan} - D_{hub}}{2} \dots\dots\dots(81)$$

So, total drag coefficient is calculated as

$$C_D = C_{DP} + C_{DS} + C_{DA} \dots\dots\dots(82)$$

where  $C_{DP}$  is obtained from cascade data.

After the aerodynamic coefficients are obtained, the nondimensional rotor loss coefficient, derivation of which can be found in [27], is calculated.

$$\Psi_{rotor} = \Psi_{th} \times \frac{C_D}{C_L} \times \frac{\phi}{\cos(\beta_m)^2} \dots\dots\dots(83)$$

As a last step, efficiency value given by Eq (65) is calculated with the information of  $\Psi_{rotor}$  and  $\Psi_{th}$ . If this value is different from the presumed value, the procedure is repeated until the efficiency at the beginning converges to the efficiency at the end. All the design part of the work is carried out by Mathcad Professional 2001, which is among the most used programs for mathematical operations. Thus, the blade and flow angles are computed for the fan. The remaining is to describe the blade spacing and chord lengths. Blade spacing is already defined in Eq (80) and chord length is obtained from the solidity definition as

$$c = \sigma \times s \dots\dots\dots(84)$$

All the procedure described up to now is repeated for every solidity value that is studied in two-dimensional cascade analysis and the solidity which gives the maximum efficiency is taken for this particular radial position. This procedure is also repeated for different radial positions on the blades to get the blade twist. In this study, blade twist was obtained by performing the calculation for hub, mean and outer diameter of the fan.

### 3.5. Sample Design

A sample mean diameter design with a solidity of  $\sigma=0.5$  is presented numerically to have a better understanding of the design procedure. Note that following design is the finalized form of the iterative solution over the efficiency value.

- Calculate axial air velocity;

$$V_a = \frac{Q}{\frac{\pi}{4}(D_{fan}^2 - D_{hub}^2)} = \frac{80m^3/s}{\frac{\pi}{4}(2.029^2 - 0.812^2)} = 29.5m/s$$

- Assume blade efficiency value;

$$\eta_{BL} = 0.51$$

- Calculate theoretical nondimensional pressure rise coefficient;

$$\Psi_{th} = \frac{H \times \rho_{air} \times g}{\eta_{BL} \times \frac{1}{2} \rho_{air} V_a^2} = \frac{50 \times 1.085 \times 9.81}{0.51 \times \frac{1}{2} (1.085)(29.5^2)} = 2.216$$

- Flow coefficient at the mean diameter is obtained

$$\phi_{mean} = \frac{V_a}{N \frac{2\pi D_{mean}}{60} \frac{1.42}{2}} = \frac{29.5}{1000 \frac{2\pi \cdot 1.42}{60} \frac{1.42}{2}} = 0.396$$

- For a swirl free inlet,

$$\varepsilon_2 = \frac{\Psi_{th} \times \phi_{mean}}{2} = \frac{2.216 \times 0.396}{2} = 0.439$$

- Relative fluid angle at the inlet to the rotor

$$\beta_1 = \arctan\left(\frac{1}{\phi_{mean}}\right) = \arctan\left(\frac{1}{0.396}\right) = 68.4^\circ$$

- Relative fluid angle at the exit to the rotor

$$\beta_2 = \arctan\left(\frac{1 - \varepsilon_2 \phi_{mean}}{\phi_{mean}}\right) = \arctan\left(\frac{1 - 0.439 \times 0.396}{0.396}\right) = 64.4^\circ$$

- Mean fluid angle through the blade

$$\beta_m = \arctan\left(\frac{\tan \beta_1 + \tan \beta_2}{2}\right) = \arctan\left(\frac{\tan 68.4 + \tan 64.4}{2}\right) = 66.5^\circ$$

- Incidence can be first written as

$$i = \beta_1 - \beta_2 = 68.4^\circ - 64.4^\circ = 4.0^\circ$$

- The deviation angle can be acquired from two-dimensional cascade data. For the solidity that is being investigated and the above incidence, the deviation angle is  $\delta = 1.2^\circ$ . The blade angles are constructed to give the desired deflection angle as follows:

$$\beta_{2k} = \beta_2 - \delta = 64.4^\circ - 1.2^\circ = 63.2^\circ$$

$$\beta_{1k} = \beta_{2k} = 63.2^\circ$$

$$i_{mod} = \beta_1 - \beta_{1k} = 68.4^\circ - 63.2^\circ = 5.2^\circ$$

- For the modified incidence, the aerodynamic coefficients are read from the related graphs.

$$C_L = 0.28 \quad \text{and} \quad C_{DP} = 0.033$$

- Secondary drag is obtained with information  $C_L$  and annulus drag is obtained with information of  $s$  and  $h$  from Eq(80) and Eq(81).

$$C_{DS} = 0.018C_L^2 = 0.018 \times 0.28^2 = 0.0014$$

$$C_{DA} = 0.02 \frac{s}{h} = 0.02 \frac{0.637}{0.609} = 0.0209$$

- Total drag is calculated

$$C_D = C_{DP} + C_{DS} + C_{DA} = 0.033 + 0.0014 + 0.0209 = 0.055$$

- Rotor loss is computed

$$\Psi_R = \Psi_{th} \frac{C_D}{C_L} \frac{\phi_{mean}}{\cos(\beta_m)^2} = 2.216 \frac{0.055}{0.28} \frac{0.396}{\cos(66.5)^2} = 1.096$$

- Blade efficiency is determined

$$\eta_{BL} = 1 - \frac{\Psi_R}{\Psi_{th}} = 1 - \frac{1.096}{2.216} = 0.51 \quad \text{The efficiency value is converged.}$$

- With solidity  $\sigma = 0.5$ , the blade chord is calculated at mean radius

$$c = \sigma \times s = 0.5 \times 0.637 = 0.319m = 31.9cm$$

When the design is carried out for a given solidity, it is seen that there is one efficiency value that the design is consistent in terms of the flow angles and the incidences, i.e. the incorrect assumptions at the beginning lead to wrong efficiency values at the end. Table 3.1 summarizes the blading efficiencies corresponding to

each solidity that is analyzed for the hub, mean and outer diameters. The designs for the hub and tip radii can be found in Appendix A.

**Table 3.1:** Blading Efficiencies for Different Solidities

$\sigma$	$\eta_{BL}$ (Hub)	$\eta_{BL}$ (Mean)	$\eta_{BL}$ (Tip)
0.1	0.42	0.51	0.29
0.2	0.57	0.51	0.29
0.5	0.75	0.51	0.19
1	0.75	0.39	0.15
1.5	0.70	0.33	0.12
2	0.66	0.28	0.10

It is seen in Table 3.1 that the blading efficiencies decrease from hub to tip. As the rotational velocity of the blades increase from hub to tip, the mean flow direction should be changed to supply the necessary deflection for design head rise, i.e an increase in  $\beta_m$  is inevitable. Thus  $\cos(\beta_m)$  term in  $\Psi_R$  equation decreases that accounts for the decrease in efficiency value.

The design parameters and settings are presented for the reversible axial fan is given in Table 3.2 and Figure 3.4.

**Table 3.2:** Design Summary

	<b>HUB</b>	<b>MEAN</b>	<b>TIP</b>
<b>Radius (m)</b>	0.41	0.71	1.01
<b><math>\sigma</math></b>	1	0.5	0.2
<b><math>\eta</math></b>	0.75	0.51	0.29
<b><math>\beta_{1k}=\beta_{2k}</math> (°)</b>	42.7	63.2	70.3
<b>Chord (cm)</b>	36.4	31.9	18.2
<b>Incidence (°)</b>	12.5	5.2	4.4

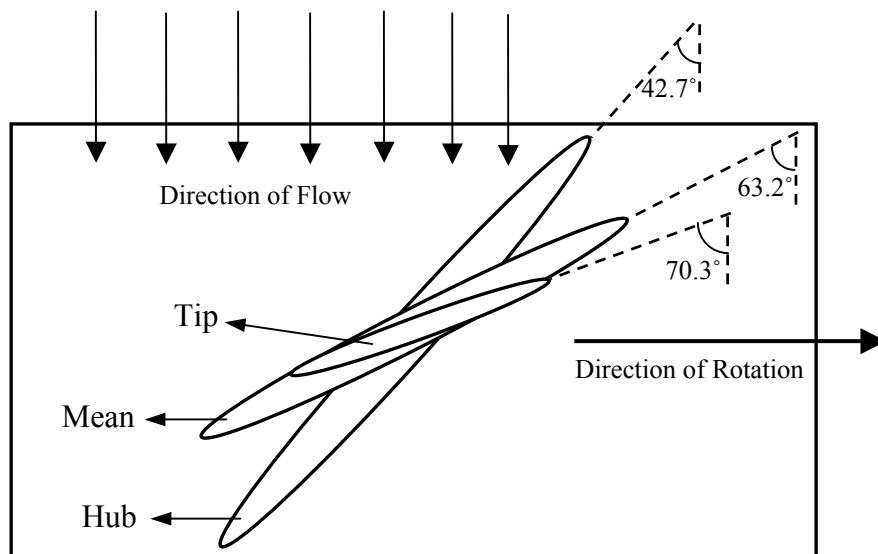


**Figure 3.4:** Schematic view of the blade settings at three radial positions

## CHAPTER 4

### PERFORMANCE ANALYSIS OF THE REVERSIBLE AXIAL FAN

#### 4.1. Introduction

The aerodynamic performance analysis of the designed reversible axial flow fan is done with the commercial CFD code, FLUENT 6.0. The geometry and the computational grid are constructed with Gambit 2.0, which is a pre-processor program for building and meshing the domains for CFD applications. Gambit 2.0 has also an add-on package, G/Turbo, which is specifically designed for modeling turbomachinery applications. This package provides automated geometry and meshing operations for blade row models. The model geometry can either be imported from an external program or generated within G/Turbo by the specification of curves describing the blade profile. In this study, the geometry of the designed fan is built within Gambit using G/Turbo package. The blade angles and chord lengths that are designed in Chapter 3 are used to have the complete picture. Also, G/Turbo meshing options allow the user to modify the decomposition of a turbo volume to facilitate meshing, to mesh the volume using either a structured or unstructured mesh. This option also enables to specify a clearance at the tip of the fan. The clearance of the modeled fan is selected as 3% of the outer diameter as it is commonly used for axial turbomachinery.

This chapter of the manuscript presents the computational mesh for the fan, the boundary conditions and the results of the computational runs for the performance analysis of the fan. The computational runs cover a range of operating conditions so

that the fan performance curve is obtained. Moreover, the rotational speed of the fan is increased to 1200 rpm, which is 20% higher than the design speed, and the results are checked with the results of a similitude analysis using affinity laws.

#### 4.2. Computational Mesh

The computational mesh of the solution domain consists of tetrahedral elements and triangular prisms. Because the domain repeats itself in every blade, the entire domain is not modeled for the required solution, only the volume around one blade is meshed. The number of cell elements in the domain is approximately 140000 and number of nodes is 27000, which accounts for one seventh of the entire fan. Figure 4.1 shows the computational mesh of the solution. In the figure, the interior elements are not shown to have the full visibility of the blade. Figure 4.2 is the mesh of the entire fan, which is built by seven periodic repeats for seven blades.

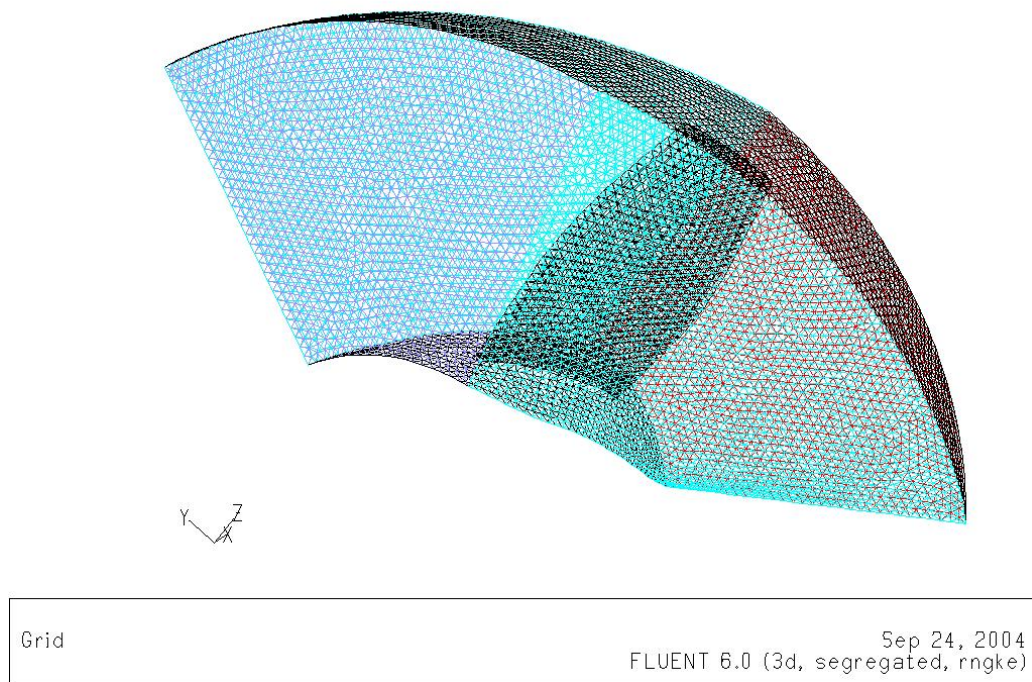


**Figure 4.1:** Computational mesh of the solution domain

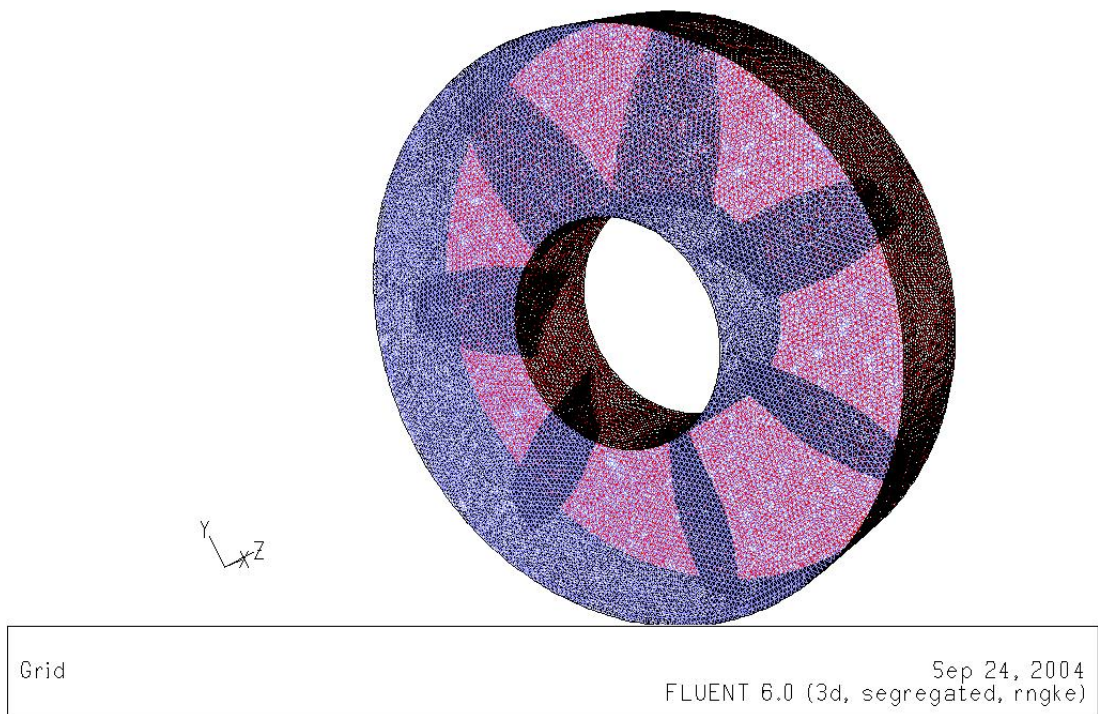


**Figure 4.2:** Computational mesh with seven periodic repeats

### 4.3. Boundary Conditions

The boundary conditions of the solution domain resemble those in the two-dimensional cascade analysis. Like the boundary conditions of the two-dimensional blade cascade solutions, the inlet and outlet faces of the mesh are Flow Inlet/Outlet type boundaries and the side faces are periodic boundaries. The difference is that the inlet face is defined as pressure inlet boundary, instead of velocity inlet boundary. Also, in three-dimensional fan analysis, the periodic boundary conditions are rotationally periodic, while the periodic boundaries in two-dimensional cascade analysis are translationally periodic. Figure 4.3 and Figure 4.4 summarize the boundary conditions of the solution domain.

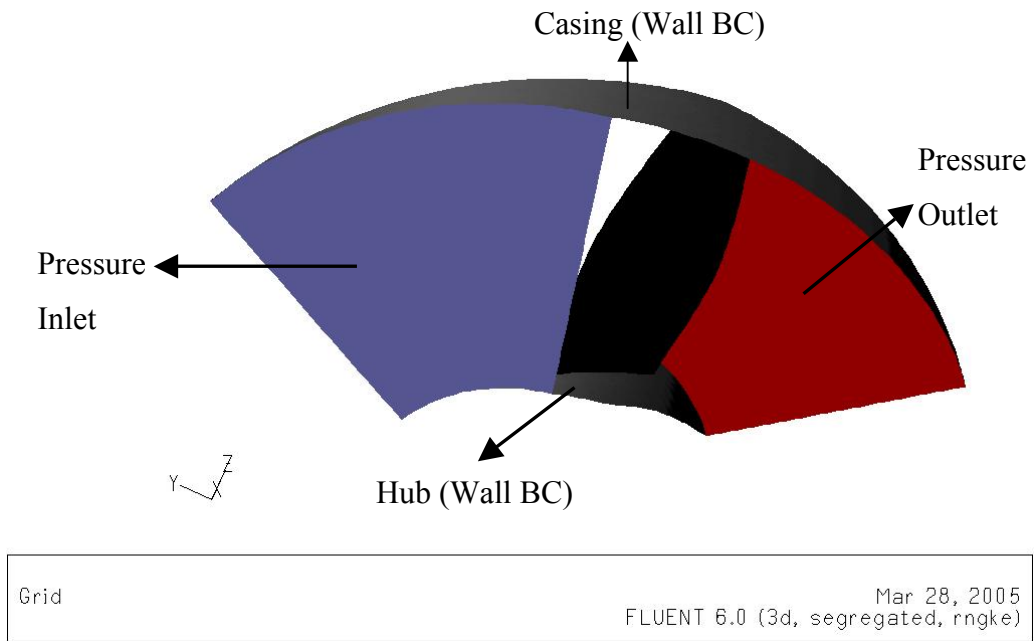


**Figure 4.3:** Fan Boundary Conditions (1)

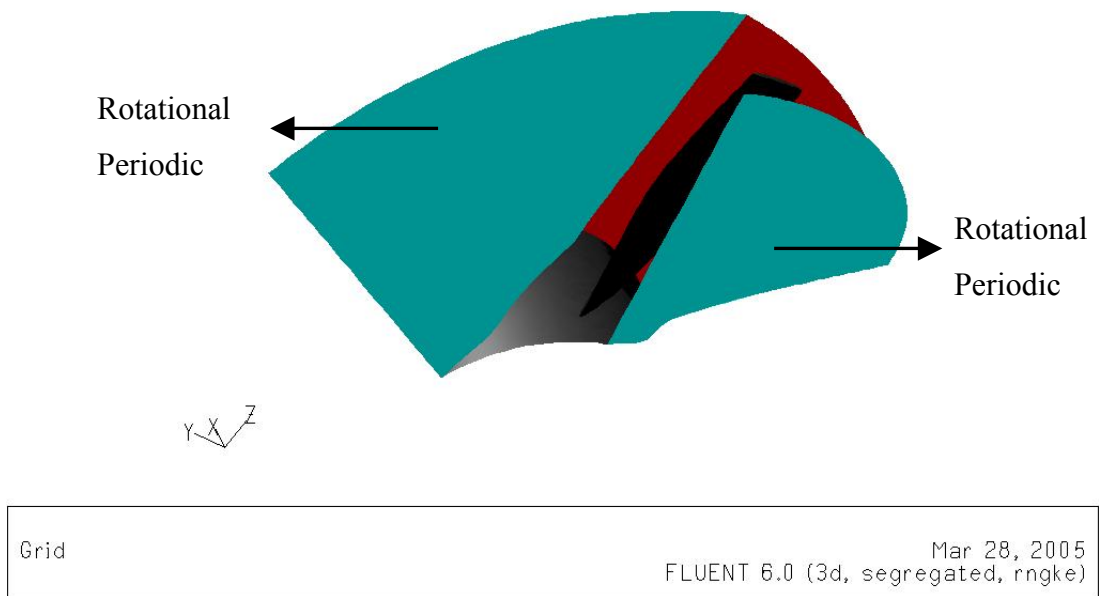


**Figure 4.4:** Fan Boundary Conditions (2)

The inlet boundary condition of the domain is pressure inlet boundary condition where the user must specify the total gage pressure at the inlet and the turbulence parameters for turbulence specification. In the current analysis, the gage pressure at the inlet is taken to be zero. Assuming a turbulence intensity level of 5% and hydraulic diameter of 0.62m at the inlet specifies the turbulence parameters. FLUENT 6.0 has the following form for pressure inlet boundary conditions.

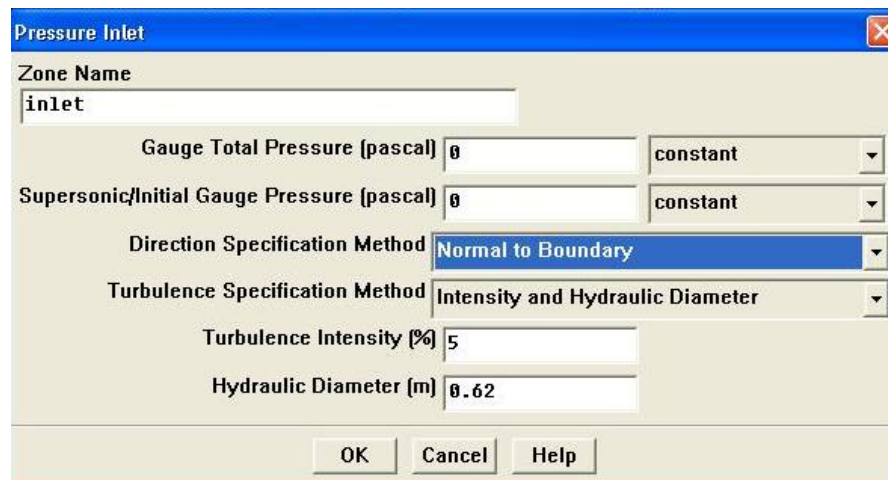


**Figure 4.5:** Pressure inlet boundary condition panel

The outlet face is described as pressure outlet boundary condition where the exit gage pressure can be specified. Figure 4.6 shows the related panel in FLUENT. In this boundary panel, radial equilibrium pressure distribution feature is activated. Because the fan is designed for free vortex method, the outlet boundary of the domain needs to satisfy the radial equilibrium pressure distribution. The specified gage pressure applies to the minimum radial position from the axis of rotation and the pressures for the rest of the zone are calculated accordingly, i.e.  $\omega r^2 = \text{constant}$  where  $\omega$  is the rotational velocity and  $r$  is the radial position. The preceding argument constitutes the framework on which the free vortex design technique for axial flow fans is based.

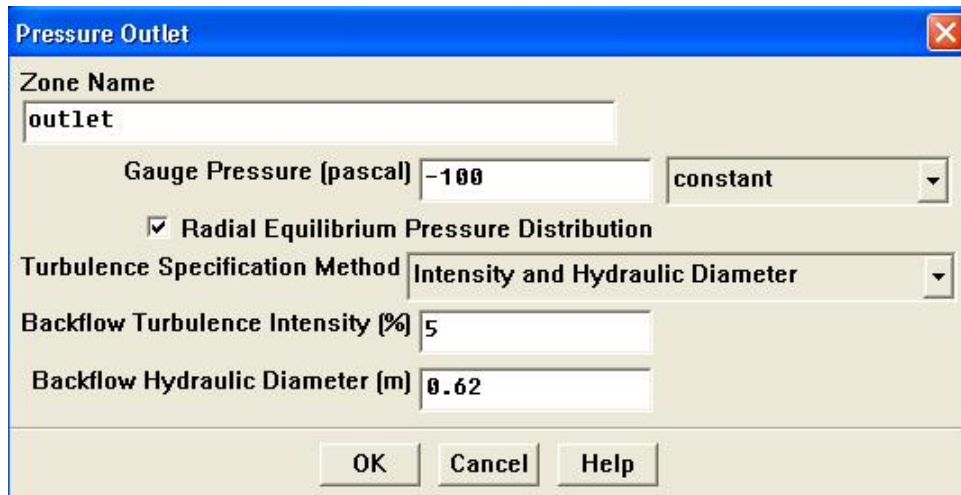


**Figure 4.6:** Pressure outlet boundary condition panel

The boundary conditions of the side faces of the domain were specified as rotational periodic boundary conditions. Like the translational periodic boundary condition that is explained in Chapter 2, the periodic zone between the periodic boundaries is rotated around a specified rotation axis. In these faces, the information for the cells is gathered from the cells located on the opposite periodic boundary as if there is no pressure gradient across the faces. The hub of the fan is defined as moving wall, which rotates at a speed of zero relative to adjacent cell zone. The casing is also defined as wall, but with zero absolute velocity. The blade surfaces, namely suction and pressure sides are defined as moving wall rotating at a speed of zero relative to adjacent cell zones, like the hub. The inside domain is described as air. The common technique used to describe a rotational speed to the solution domain is specifying the motion type as ‘moving reference frame’ for the interior part. 1000 rpm is assigned as the rotational velocity of the interior region along with the direction of rotation. Figure 4.7 shows the boundary condition panel used to describe the fluid motion.

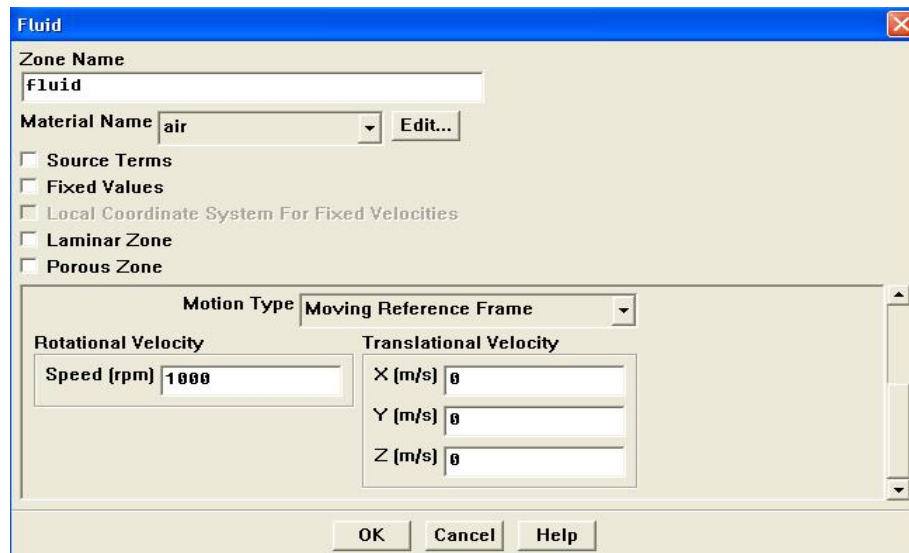


**Figure 4.7:** Boundary condition panel for the fluid zone

#### **4.4. Solution of the Aerodynamic Performance of the Fan**

##### **4.4.1. Turbulence Model and Solution Controls**

The results are obtained with the solution of the continuity and N-S equations along with the equations for the selected turbulence model. For the solution of the turbulence, RNG k- $\epsilon$  model is selected. This model is applicable to complex shear flows involving rapid strains, moderate swirl, vortices and locally translational flows (e.g., boundary layer separation, massive separation, room ventilation etc.) [2]. The details and several applications of the model can be found in Chapter 1.

After the boundary conditions are set, the solution and the turbulence model are specified. The solution is obtained by segregated solver with absolute velocity formulation, three dimensions in space and steady in time. The turbulence model is selected as RNG k- $\epsilon$  model and the swirl dominated flow feature is activated to enhance the accuracy for this application (Figure 4.8.). Standard wall functions are used for near wall treatment.

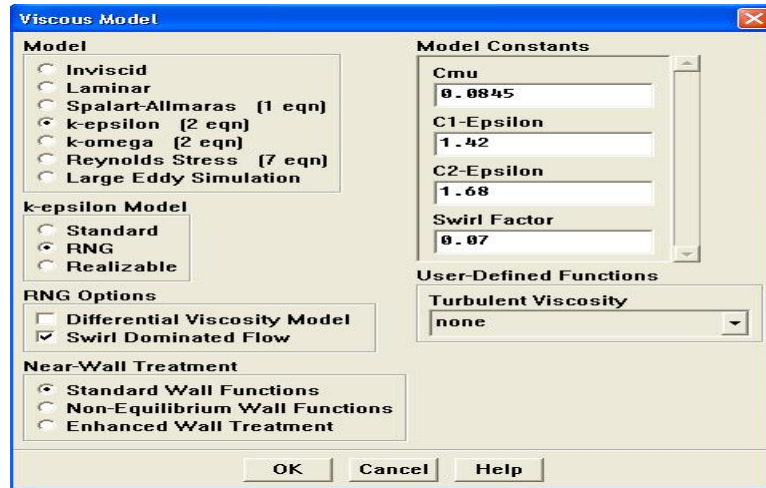


**Figure 4.8:** Viscous Model Form in FLUENT.

For the numerical solution of momentum, turbulence kinetic energy and turbulence dissipation rate equations, second order upwind discretization scheme is selected. Because the flow across the fan has high rates of swirl and turbulence, and unstructured mesh is constructed in the solution domain, the flow is not aligned with the grid, thus second order discretization is preferred for higher accuracy. Linear option is selected for the pressure interpolation scheme that simply averages the pressures in adjacent cells to obtain face pressure values. To obtain the pressure field, SIMPLE algorithm is used under pressure-velocity coupling drop-down list. This algorithm uses a relationship between pressure and velocity corrections to enforce mass conservation and obtain pressure field [2]. The details of the algorithm can be found in literature.

Another thing to be controlled for the solution is the under-relaxation factors. Because of the non-linearity of the equation set being solved by the segregated solver, it is necessary to control the change of solution variables at each iteration, which is typically done by under-relaxation. Let  $\Phi$  be any computed variable and in a simple form, the new value of the variable  $\Phi$  within a cell depends upon the old value,  $\Phi_{old}$ , the computed change in  $\Phi$ ,  $\Delta\Phi$ , and the under-relaxation factor,  $\alpha$ , as follows

$$\Phi = \Phi_{old} + \alpha \Delta \Phi \dots\dots\dots(83)$$

For most flows, the default under-relaxation factors do not usually require modification. If unstable or divergent behavior is observed, however, the under-relaxation factors for pressure, momentum, k and ε from their default values may need to be reduced. During the computations for the axial fan performance, default values were kept unless a divergent and unstable trend had been observed.

Figure 4.9 shows the solution control panel in FLUENT.

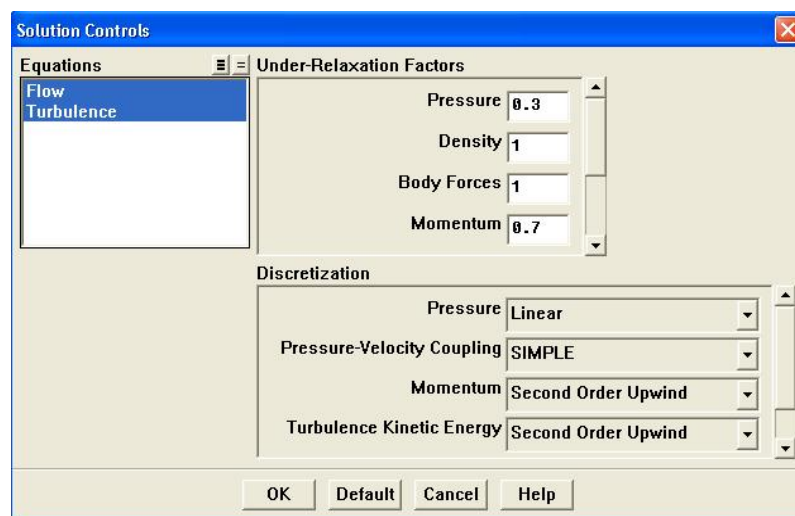


**Figure 4.9:** Solution Control Panel

#### 4.4.2. Iteration Results

The iterations for the performance points are made by assigning different gage pressure values at the exit boundary of the domain, resulting in corresponding flowrates for the pressure differentials across the fan. The inlet pressures are kept constant but the outlet pressures are changed. At the end the overall solution and the performance curve for the fan are given. The iterations are performed for the design rotational speed of 1000 rpm and for the increased rotational speed of 1200 rpm to check the consistency of the results with the fan affinity laws.

#### 4.4.2.1. Iteration Results for Design Rotational Speed

As it is noted before, the design is performed for a total pressure rise of 532 Pa, a design flowrate of 80 m<sup>3</sup>/s for the rotational speed of 1000 rpm. The results of the computations give a total pressure rise of 528.5 Pa across the fan for the design flowrate of 80 m<sup>3</sup>/s. This 0.6 % difference between the design pressure rise and numerical analysis can be interpreted as close and the results are in good agreement. The computed performance points for the fan are tabulated in Table 4.1 and the graphical representation is given in Figure 4.10.

**Table 4.1:** Computed Performance Points for the Fan (N=1000 rpm)

Flowrate (m <sup>3</sup> /s)	Total Pressure (Pa)	Total Head Rise(m)	Hydraulic Efficiency (%)
28,5	1239	116,4	29,5
45,8	1057,0	99,3	55,4
60,3	694,0	65,2	63,0
63,5	583,6	54,8	64,0
70,4	600,0	56,4	66,4
76,6	559,0	52,5	69,2
78,9	540,0	50,7	71,0
85,4	465,8	43,8	73,3
93,0	343,0	32,2	71,0
104,8	134,5	12,6	53,0

When Table 4.1 and Figure 4.10 are investigated carefully, it is seen that the range of computed flowrates does not extend to ‘closed valve’ position. The reason is that the operational range for the axial turbomachinery does not fall to the left of the stalling dip so the computations were not carried out in this unstable and inefficient range. Another reason is that the numerical analysis of ‘closed valve’ position requires more equipped computational resources because of the high instability and complexity of the flow in this range. Moreover, the hydraulic efficiency values seem

to be lower than other axial fan applications. This is probably the consequence of symmetrical blade profiles that need to be used in the application. The blade profiles do not have a camber thus the ratio of lift forces to drag forces is reduced, resulting in the decrease of hydraulic efficiency. The hydraulic efficiency of the fan is internally calculated by FLUENT. The program calculates the pressure rise across the inlet and outlet of the domain multiplies it by the flowrate and divides it to the product of torque exerted on the rotor and the specified rotational speed. This capability of the program is appreciated that the user does not have to calculate the torque exerted on the rotor due to highly complex force field.

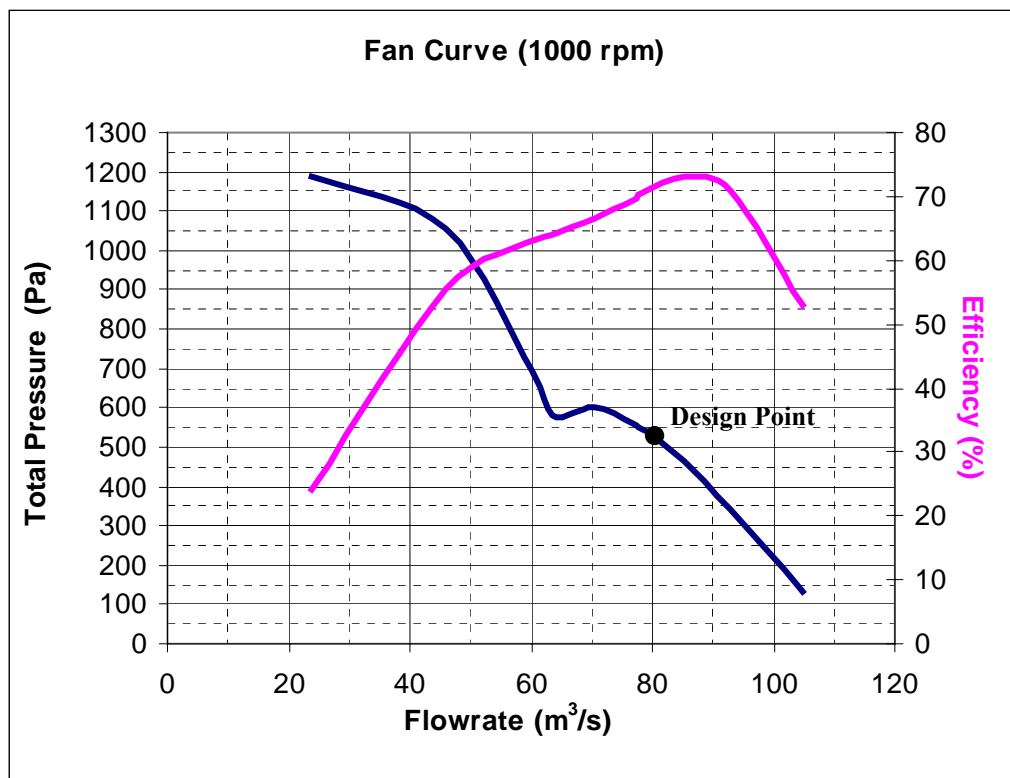


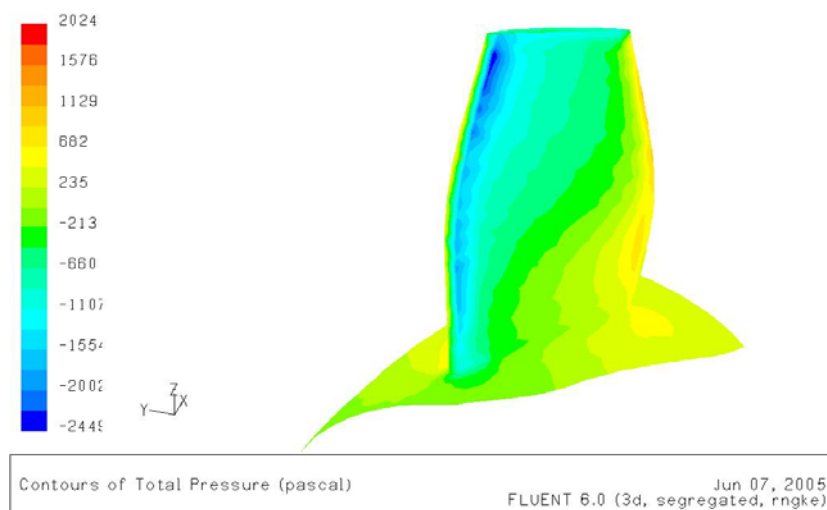
**Figure 4.10:** Fan Performance Curve (N=1000 rpm)

In Figure 4.10 it is shown that the safe operation range for the fan starts approximately from 70 m³/s flowrate. For the flowrates lower than this value the fan

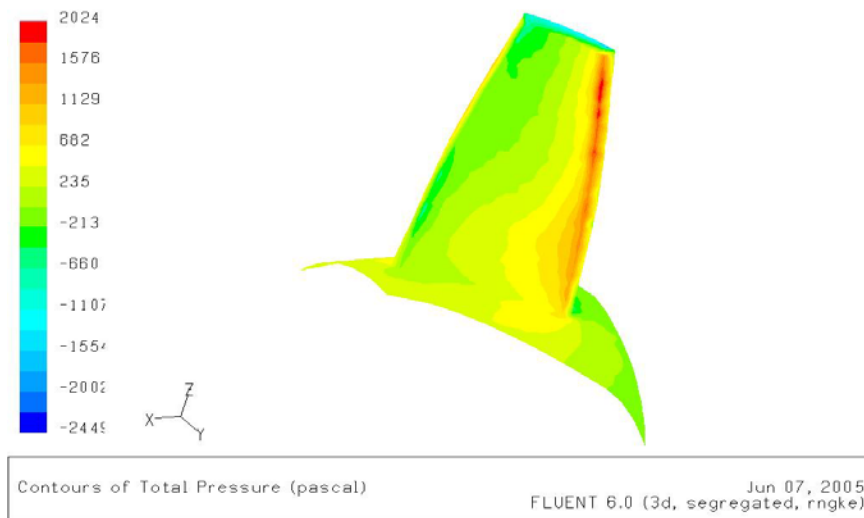
stalls and noisy and inefficient operation is expected. The operation between 75 m<sup>3</sup>/s and 95 m<sup>3</sup>/s is recommended.

When Figure 4.10 is investigated, it is seen that maximum efficiency point of the fan is approximately at 85 m<sup>3</sup>/s flowrate but not at 80 m<sup>3</sup>/s, which is the design point. The possible reason of the difference is the deflection of the pathlines at the inlet of the blade row due to the pressure differential across the rotor. As the pressure differential across the rotor is increased, the incoming flow starts to gain tangential component at the entrance region thus swirl free inlet assumption of the design is disturbed. The deviated pathlines result in the change of effective incidences on the blade, so the design incidences, which give the most efficient operation, are no longer present on the rotor blades. This phenomenon is less pronounced in the operating points that have less pressure rise and the corresponding L/D ratio for the blades, which is responsible for the efficiency, is closer to the design values.

Figure 4.11 displays the total pressure contours on the blades. 4.11(a) shows the suction side of the blade and 4.11 (b) displays the pressure side. The low-pressure region on the suction side and the high-pressure region on the pressure side are identified.

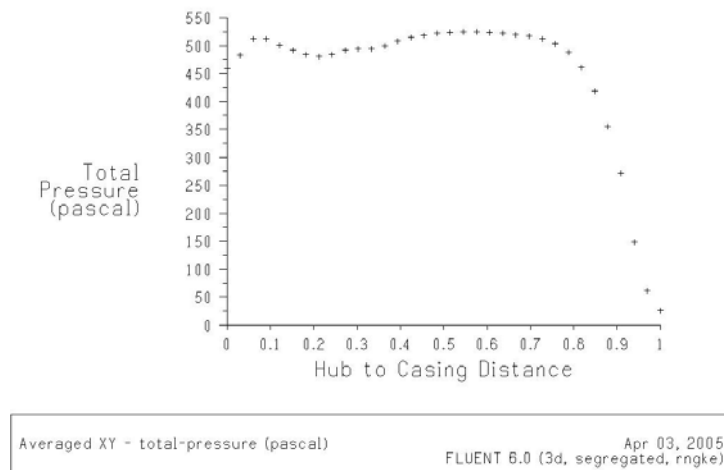


**Figure 4.11(a):** Total pressure contours on the suction side of the blade



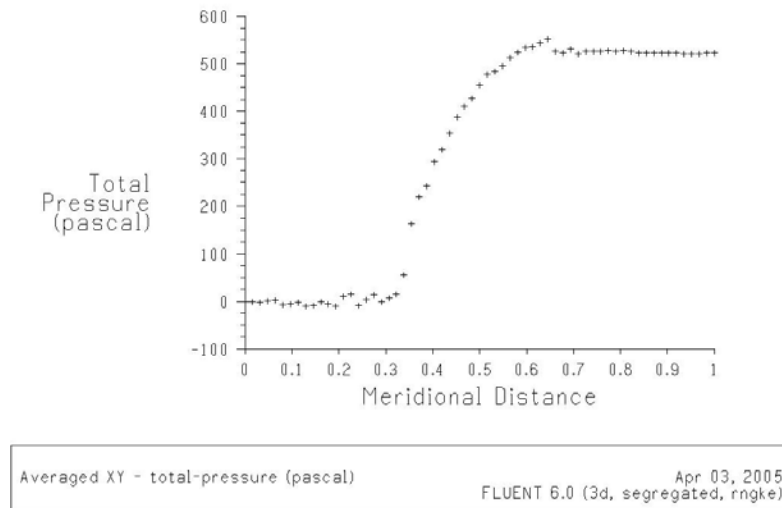
**Figure 4.11(b):** Total pressure contours on the pressure side of the blade

Because the fan is designed with free-vortex technique, the pressure at the outlet section do not vary along the radial direction. Figure 4.12 shows the variation of total pressures at the outlet section along radial direction for 85.4 m<sup>3</sup>/s flowrate.

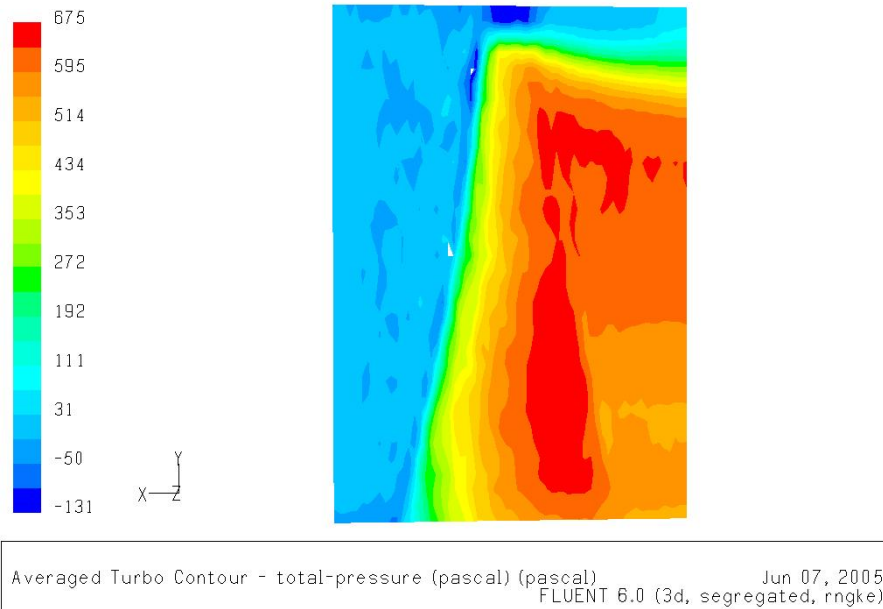


**Figure 4.12:** Total pressures at the outlet section along radial direction

As it is seen in Figure 4.12, the pressure values at the outlet follows approximately a stable trend as it is expected. Figure 4.13 shows the total pressure values along meridional direction from inlet to outlet, at the mid-height from hub to casing.



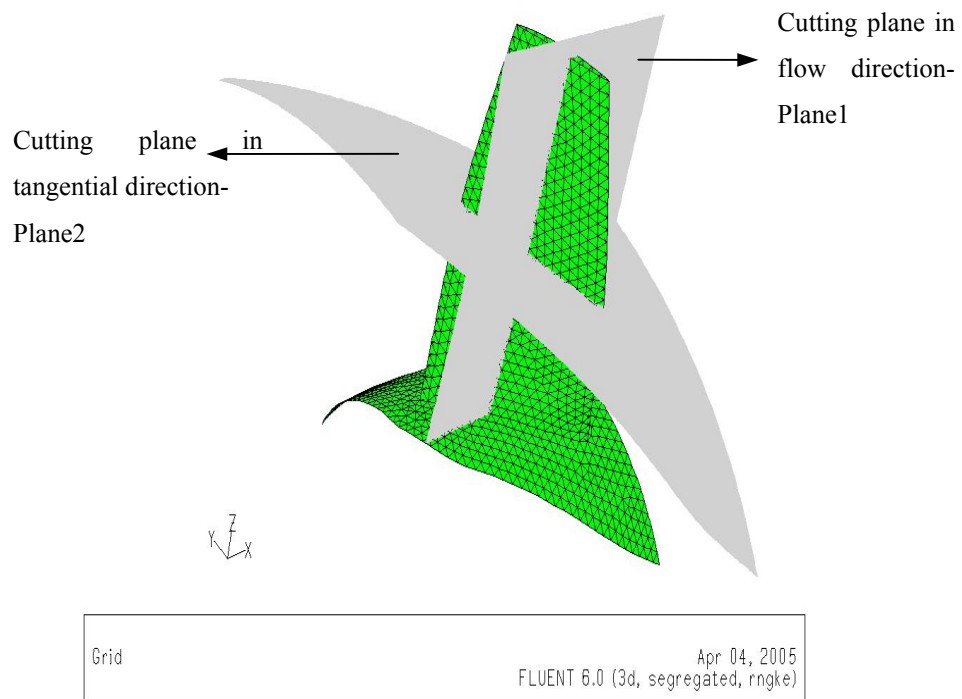
**Figure 4.13:** The total pressures along meridional direction at the mid height from hub to casing



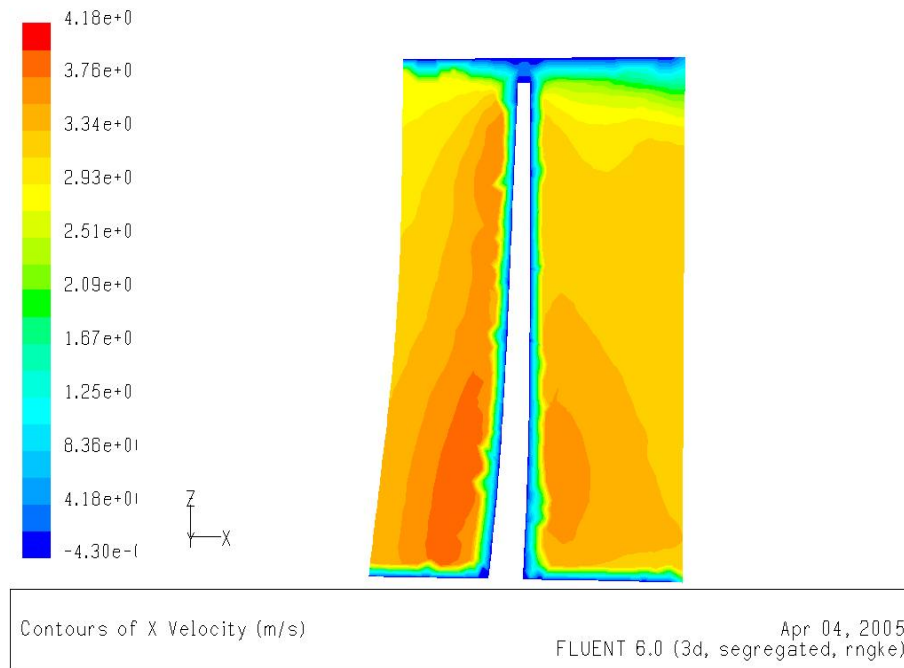
**Figure 4.14:** Circumferentially averaged total pressures in the domain

Figure 4.14 displays the circumferentially averaged total pressure values in the domain. The total pressures increase from the inlet to the outlet and the decrease in the magnitudes is seen in the clearance region.

In order to have a better understanding of the velocity vectors and flow in the tip clearance region, the section as shown in Figure 4.15 should be investigated. The velocity contours are seen in the following figure. Figure 4.16 shows that there is no backflow occurring in the tip clearance region.



**Figure 4.15:** Planes that cut the blades in flow and tangential directions



**Figure 4.16:** Contours of X direction velocity in Plane 1

As it is noted in Chapter 1, the axial flow characteristics of axial turbomachinery change as the pressure resistance increases (Figure 1.9). The path lines start to deflect in radial direction as the ‘closed valve position’ is approached and centrifugal effects begin to appear. First, the path lines start to separate from the hub and deflect in radial direction (Figure 1.9(c)). As the pressure resistance is increased, the deflections of the path lines are more pronounced in the higher radial positions (Figure 1.9(b)).

The path lines across the rotor of the designed fan are shown in Figure 4.18(a) to 4.18(f) for the operating points given in Figure 4.17. The figures show the centrifugal behavior of the axial fan when the pressure resistance is increased. Figures 4.19(a) to 4.19(c) display the path lines at the hub section. Figure 4.18(d) displays no radial flow on the mid span section while the flow slightly separates from the hub at the same operating point (Point D) in Figure 4.19(b).

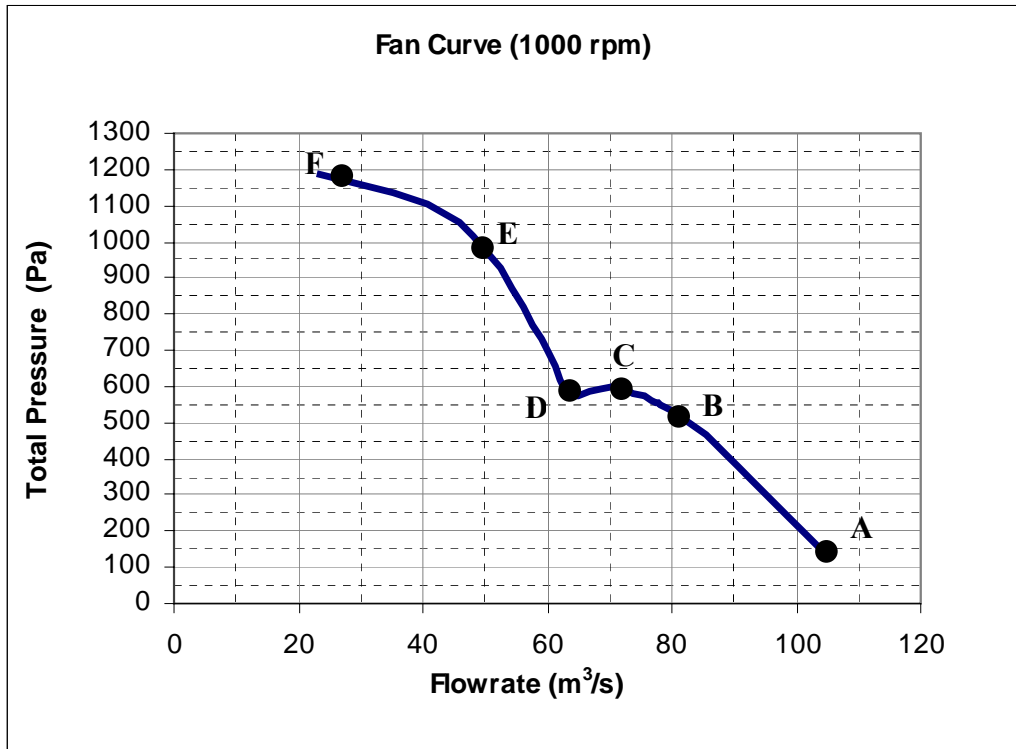


**Figure 4.17:** Several operating points

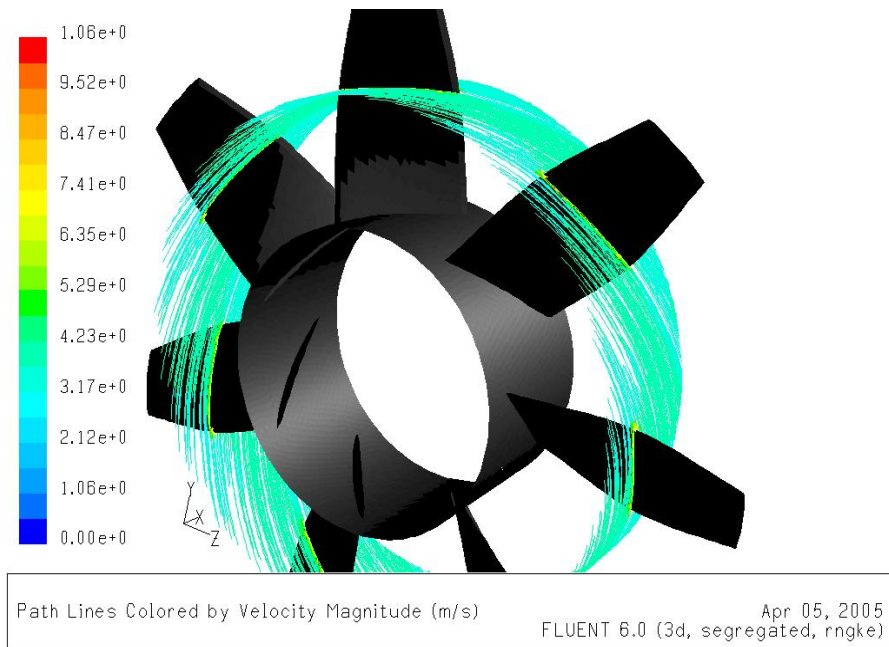


**Figure 4.18(a):** Pathlines at mid-span for operating point (A)

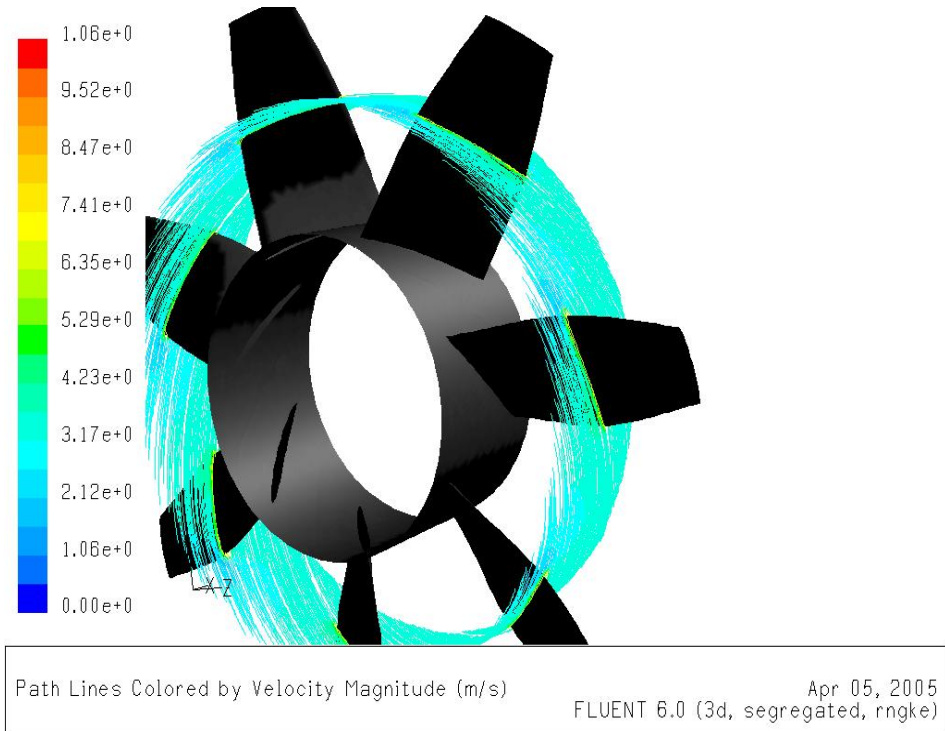


**Figure 4.18(b):** Pathlines at mid-span for operating point (B)

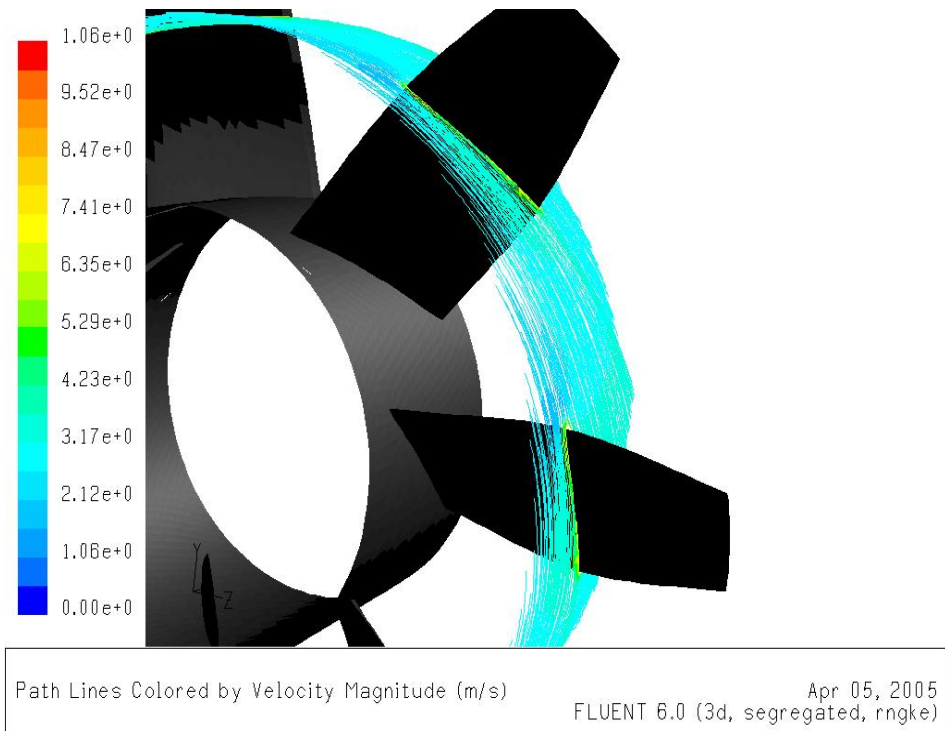


**Figure 4.18(c):** Pathlines at mid-span for operating point (C)

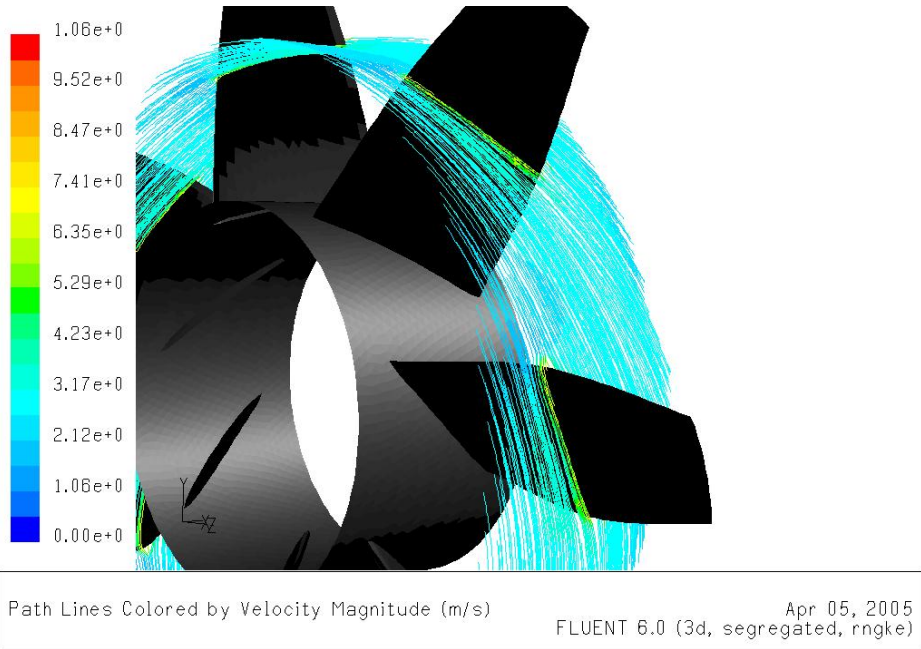


**Figure 4.18(d):** Pathlines at mid-span for operating point (D)

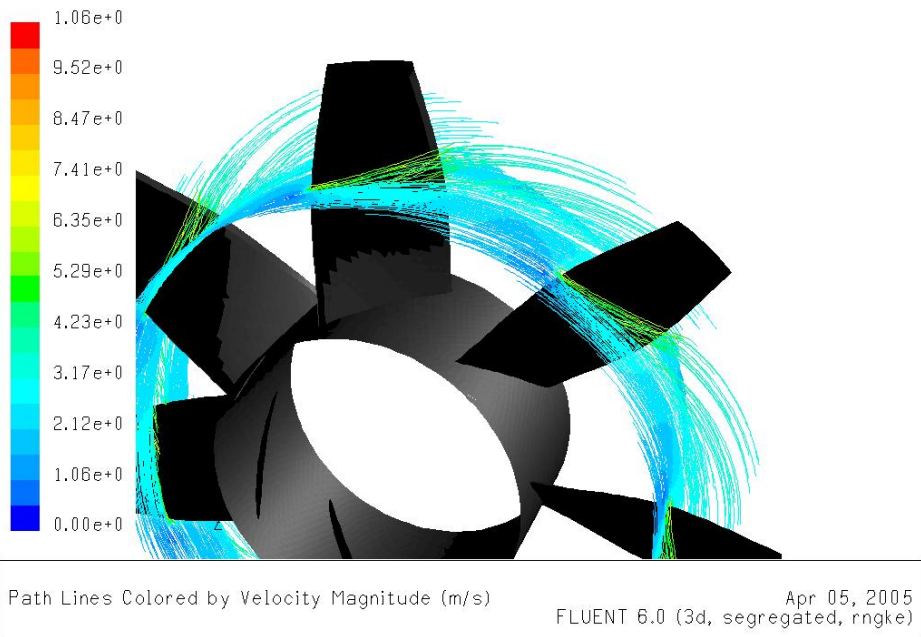


**Figure 4.18(e):** Pathlines at mid-span for operating point (E)

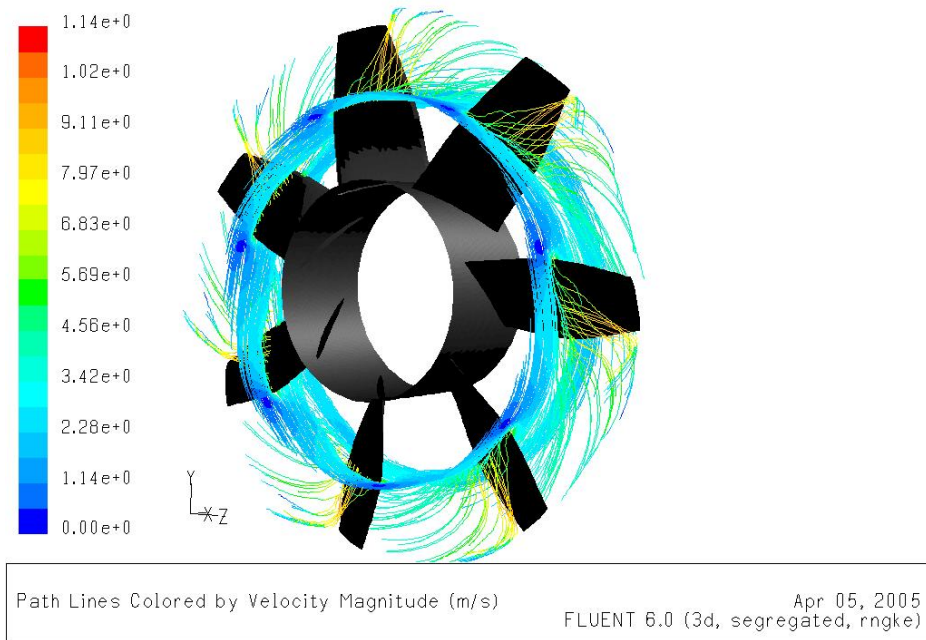


**Figure 4.18(f):** Pathlines at mid-span for operating point (F)

Figure 4.18(a) to 4.18(f) show that the pathlines at the mid-span start to deviate from ideal streams after operating point E given in Figure 4.17. Figure 4.18 (b) and 4.19 (a) show that the pathlines are smooth at the mid-span and at the hub; there is no separation of the flow either from the blades and the hub. As it can be remembered from Chapter 1, at the lowest point of the stalling dip (point D in Figure 4.17), the pathlines across the rotor start to separate from the hub surfaces of the fan (Figure 4.19 (b)) while the pathlines show a favorable trend at the mid-span for the same operating point (Figure 4.18 (d)). This separation is caused by the separation of the stream on the back of the blades due to increased incidences. The particles separated from the hub are collected on the front side of the succeeding blade, so a vortex structure is formed at the tip of the blade (Figure 4.20). From this point to shut off, the flow passes the rotor no longer axially but at a slope. As the shut off is approached, the vortex at the tip of the blade gets larger and the separated stream from the hub extends into the blade passage. The flow passes the rotor more or less radially and therefore the pressure rises as in the radial blades (Figure 4.19(c)).

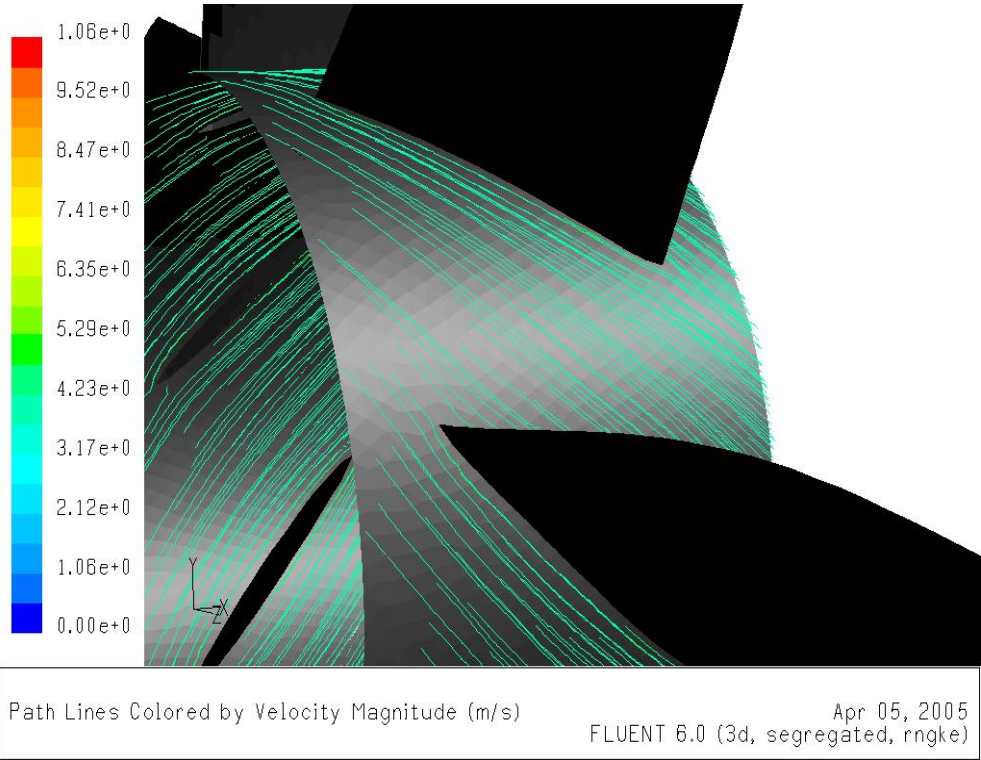


**Figure 4.19(a):** Path lines on the hub at design point (B)

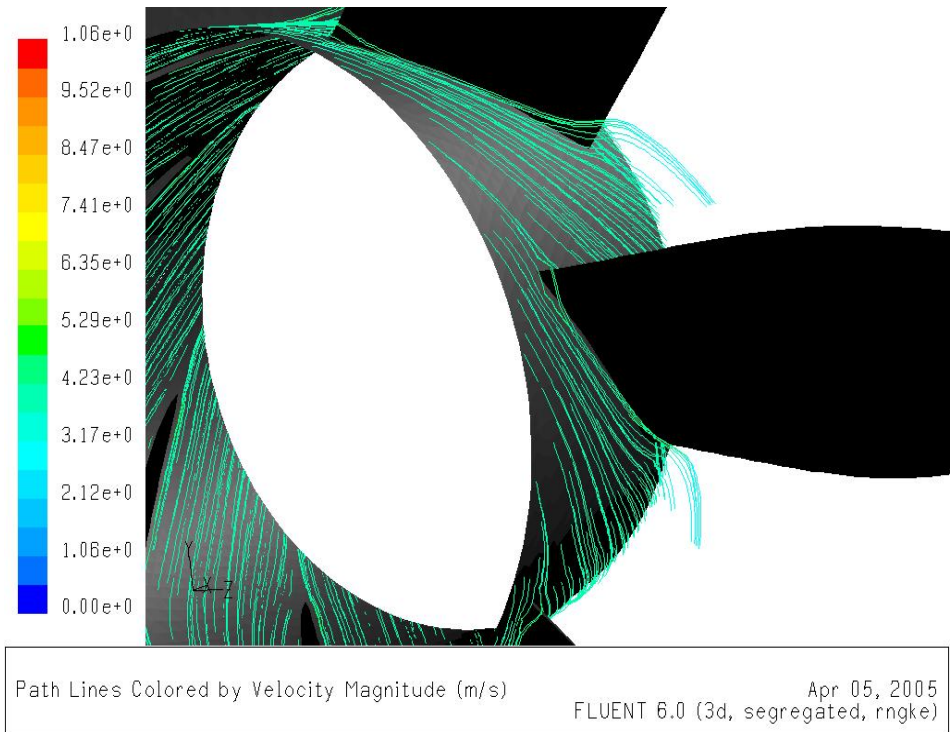


**Figure 4.19(b):** Path lines on the hub at operating point (D)

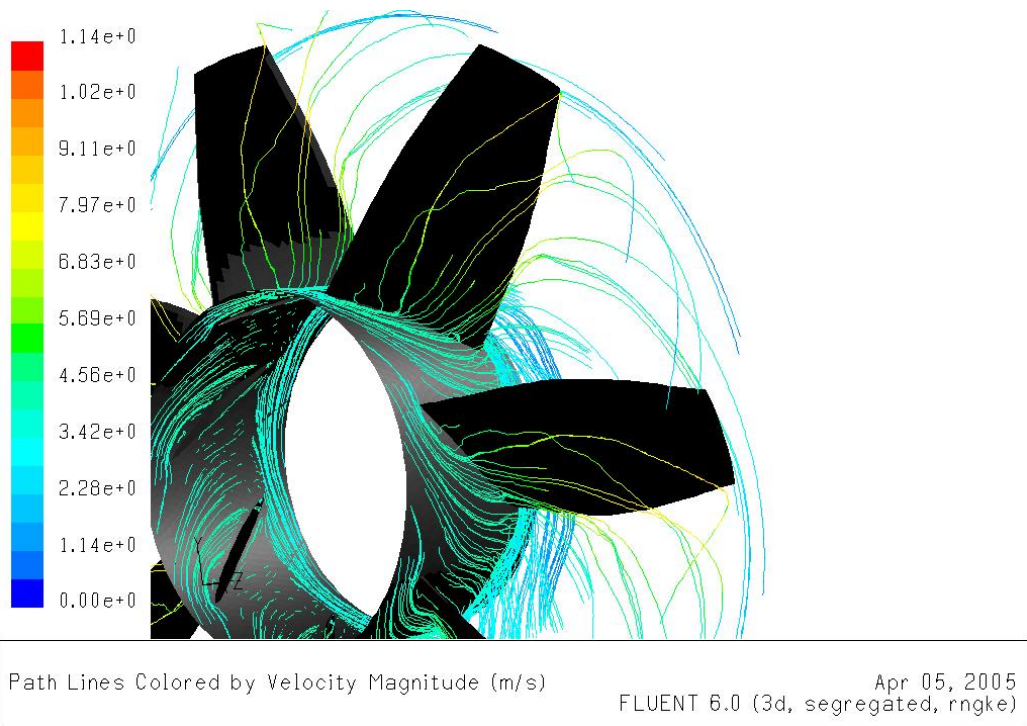


**Figure 4.19(c):** Path lines on the hub at operating point (F)

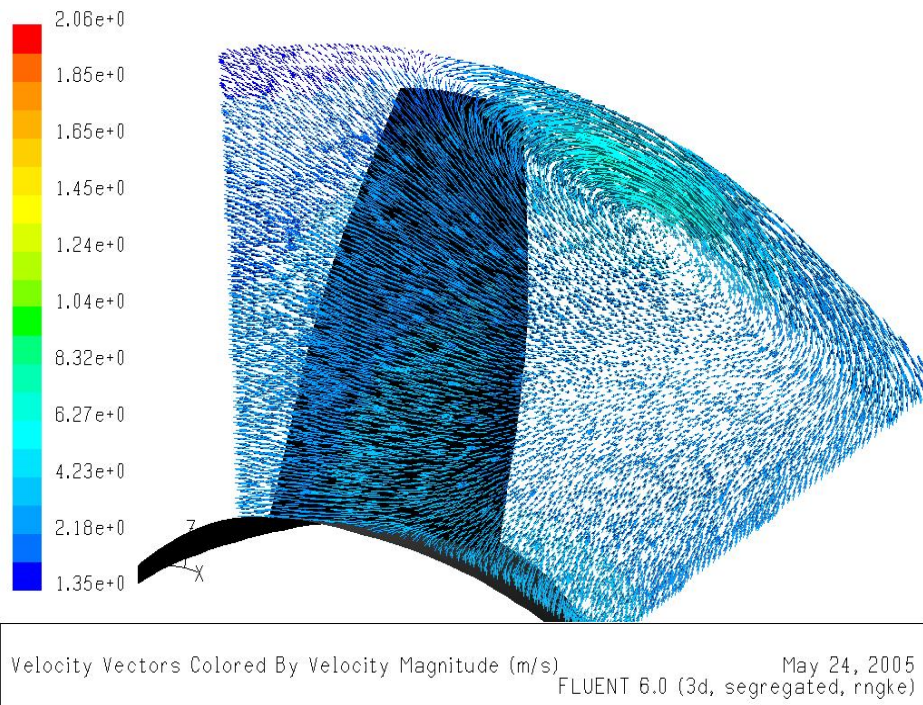


**Figure 4.20:** Vortex formation at the tip of the blade for operating point (D).

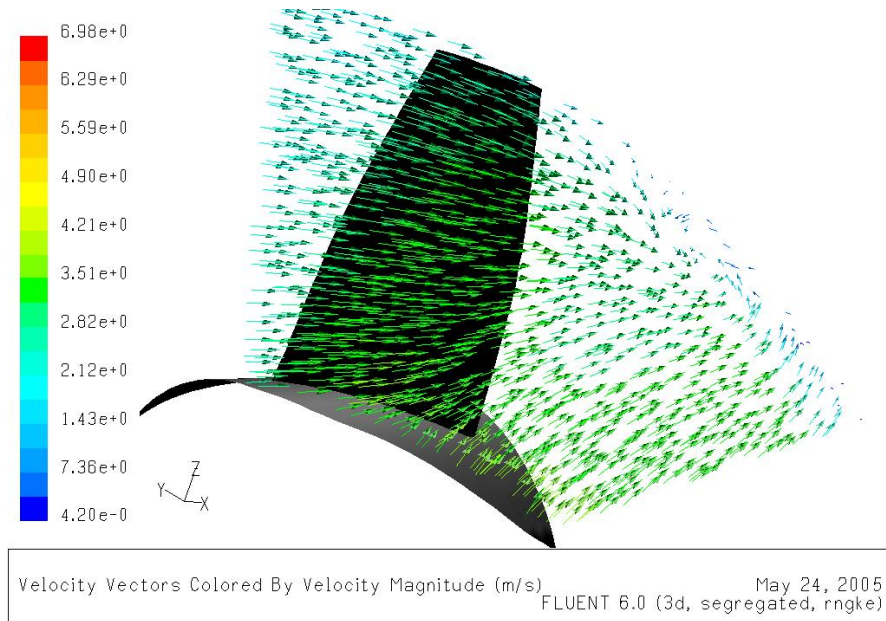


**Figure 4.21:** Smooth airflow at the design point (B).

The loss in the axial component of the velocity and the velocity magnitude can be seen in the following figures. Figure 4.22 shows the contours of velocity magnitudes for the operating point (B). The velocity colors in Figure 4.20 has usual trend for axial turbomachinery while the loss in the velocity magnitude at operating point (F) is observed inside the blade passage in Figure 4.23.

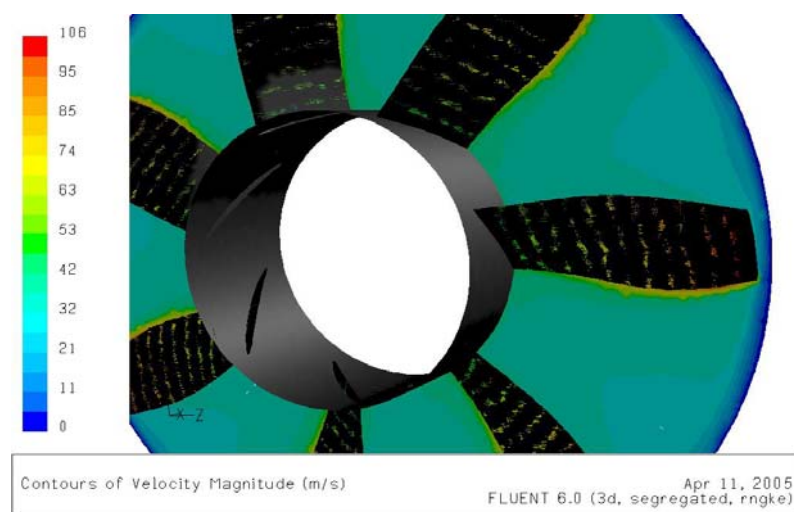


**Figure 4.22:** Contours of velocity magnitude at operating point (B)

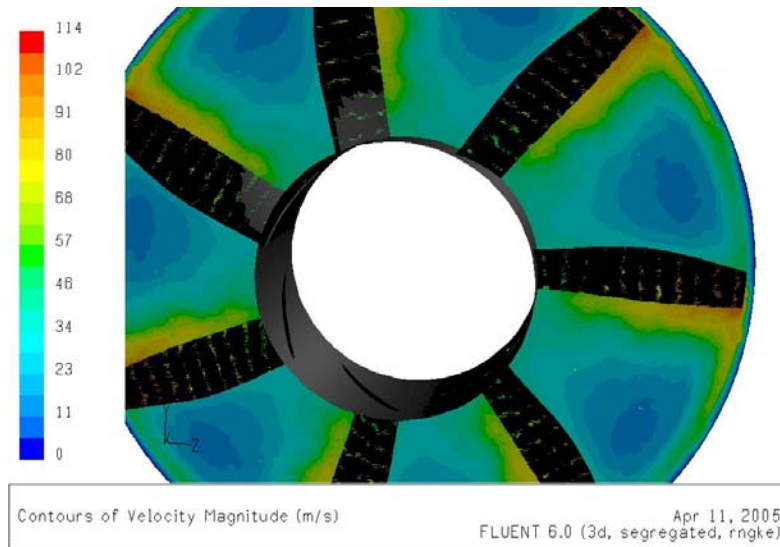


**Figure 4.23:** Contours of velocity magnitude at operating point (F)

The velocity vectors inside the blade passage are shown in Figures 4.24 and 4.25. The velocity vectors direct the usual flow direction at the operating point (B) in Figure 4.24. The recirculation zone is identified in Figure 4.25 at the operating point (F).

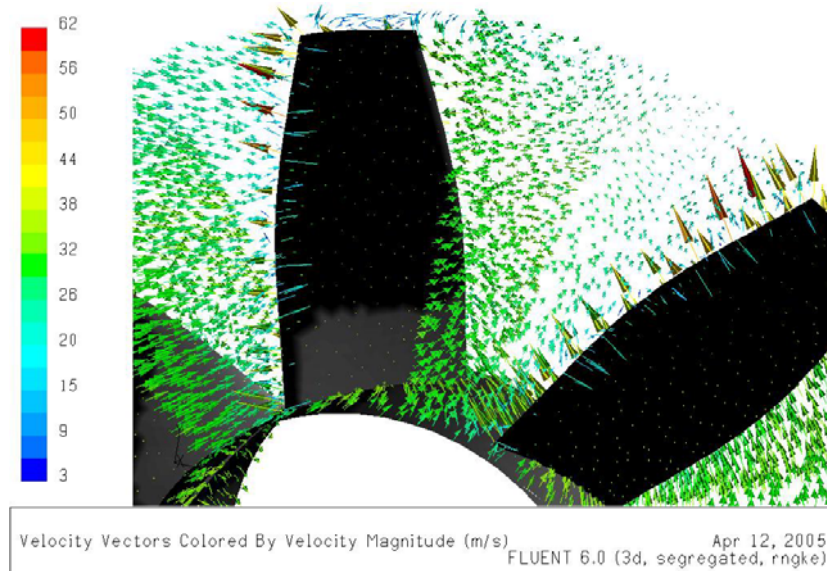


**Figure 4.24:** Velocity vectors at operating point (B).

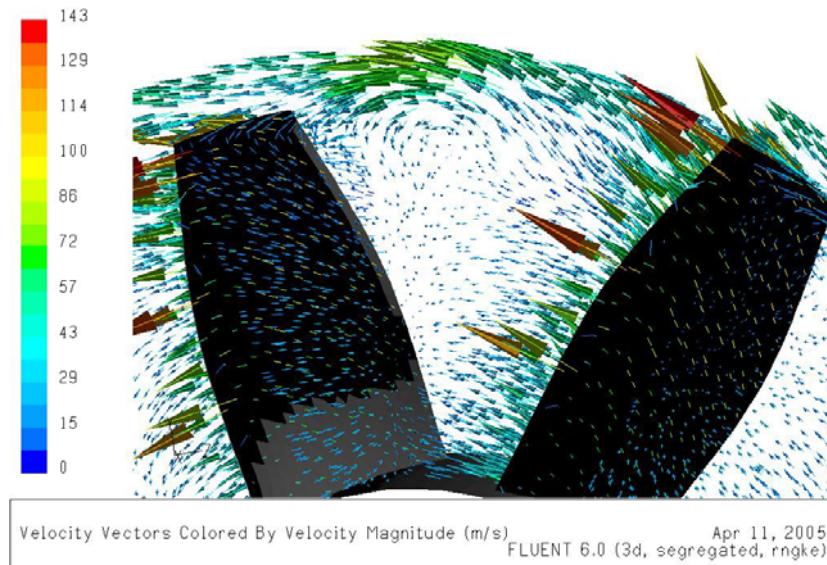


**Figure 4.25:** Velocity vectors at operating point (F).

The performance of the designed fan is examined thoroughly. The performance points and the fan curve are obtained. Also, a deep view of the fluid flow inside the blade passages and across the fan is investigated.

#### 4.4.2.2. Iteration Results for the Increased Rotational Speed

##### 4.4.2.2.1. Fan Similitude Analysis

Performance of a turbomachine can be described by several independent variables, which are

- Volumetric flowrate (Q)
- Energy per unit weight (H)
- Characteristic dimension (D)
- Power (P)
- Density and viscosity of the working fluid ( $\rho, \mu$ )
- Rotational speed of the impeller (N)

These parameters are interrelated with each other in terms of nondimensional terms. For similar turbomachines, these nondimensional terms are constant for different operating conditions. These nondimensional terms can be given as

$$\pi_Q = \frac{Q}{ND^3} \dots\dots\dots(84a)$$

$$\pi_H = \frac{gH}{N^2 D^2} \dots\dots\dots(84b)$$

$$\pi_P = \frac{P}{\rho N^3 D^5} \dots\dots\dots(84c)$$

$$\pi_\mu = \frac{\mu}{\rho ND^2} \dots\dots\dots(84d)$$

The first three  $\pi$  terms are also referred as affinity laws;  $\pi_\mu$  is used to correct the similarity for Reynolds number effects.

For the current axial fan application the flow is incompressible, gravitational acceleration is constant and only rotational speed change is present. The nondimensional parameters reduce to

$$\pi_Q = \frac{Q}{N} \dots\dots\dots(85a)$$

$$\pi_H = \frac{gH}{N^2} \dots\dots\dots(85b)$$

$$\pi_P = \frac{P}{N^3} \dots\dots\dots(85c)$$

If an operating point on the fan curve for the design speed is denoted by  $(Q_1, H_1)$ , the similar operating point  $(Q_{1'}, H_{1'})$  for 20% increased rotational speed that corresponds to  $(Q_1, H_1)$  is found as

$$Q_{1'} = 1.2Q_1 \dots\dots\dots(86a)$$

$$H_{1'} = (1.2)^2 H_1 = 1.44H_1 \dots\dots\dots(86b)$$

$$P_{1'} = (1.2)^3 P_1 = 1.728P_1 \dots\dots\dots(86c)$$

The efficiencies of a fan operating at two different operating conditions are assumed to be the same if the first three  $\pi$  terms given by Eq (84a) to Eq (84c) are equal. But this assumption of equal efficiency at similar operating conditions implies also the equality of Reynolds numbers and geometrical similarity of the surface roughness. For the same machine operating at different speeds, surface roughness is the same at two operating conditions but the Reynolds number differs. The correction for the Reynolds number on the efficiency can be done by the empirical formula given by Ackeret.

$$\frac{1 - \eta_{1'}}{1 - \eta_1} = \frac{1}{2} \left[ 1 + \left( \frac{Re_1}{Re_{1'}} \right)^{0.2} \right] \dots\dots\dots(87)$$

**4.4.2.2.2. The Comparison of the Results**

The results for the similarity analysis of the data obtained for the design rotational speed and the simulation results for the increased speed are tabulated in Table 4.2.

**Table 4.2:** Data for increased rotational speed analysis

Design Speed (1000 rpm)		Similarity Results (1200 rpm)		Simulation Results (1200 rpm)	
Flow Rate (m <sup>3</sup> /s)	Total Pressure Rise (Pa)	Flow Rate (m <sup>3</sup> /s)	Total Pressure Rise (Pa)	Flow Rate (m <sup>3</sup> /s)	Total Pressure Rise (Pa)
28,5	1239	34,1	1784	38,5	1708
45,8	1057	55,0	1522	67,4	1263
60,3	694	72,3	999	72,3	951
63,5	584	76,2	840	78,2	859
70,4	600	84,5	864	84,3	862
76,6	559	91,9	805	88,8	805
78,9	540	94,7	778	89,9	800
85,4	466	102,4	671	97,4	738
93,0	343	111,6	494	105,5	591
104,8	135	125,8	194	117,1	370

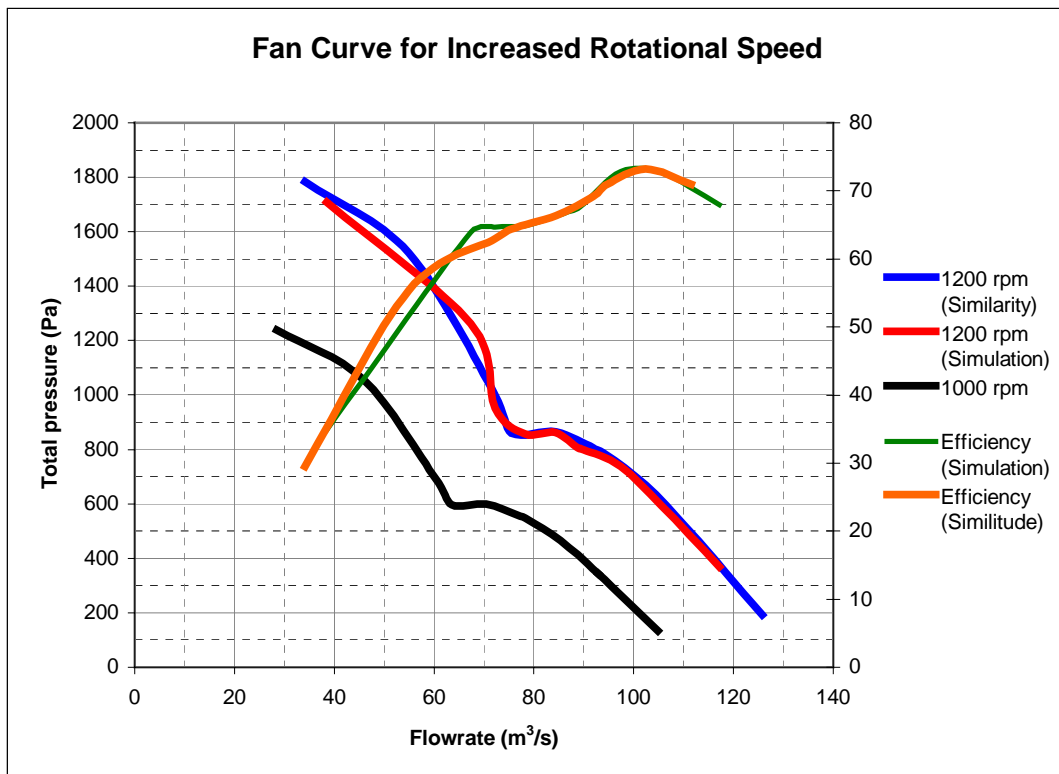


**Figure 4.26:** Fan performance curves for increased rotational speed

The data on Table 4.2 are expressed graphically by the fan performance curves in Figure 4.26 for the design speed and increased rotational speed. The increased rotational speed curves include both the similarity analysis and simulation results. The curves for the increased rotational speed show approximately the same trend in the recommended operation range. After the fan stalling, little discrepancy is observed. The results of the simulation for this region can be interpreted as acceptable because the flow in this region of the performance curve is quite chaotic inside the blade passages thus the analysis may not predict consistent results with the similarity analysis. Briefly, the results in the recommended operation range are quite well and the results in the region left to fan stalling point are in acceptable ranges.

## **CHAPTER 5**

### **DISCUSSION OF THE RESULTS AND CONCLUSION**

#### **5.1. General**

Axial ventilation fans are the most important components that are used to discharge the smoke generated by the fires in underground transportation systems, mines etc. These fans should operate bi-directional, i.e. same performance in exhaust and supply mode operation, to cope with the possible fire incidences that may occur in any location along the tunnels or in the stations. The fact under the capability of bi-directional operation lies on the selection of blade profiles and their proper settings.

In this study, the design and performance analysis of reversible axial ventilation fans are performed. The aerodynamic performances of the symmetrical elliptical blade profiles for bi-directional operation are acquired from CFD analysis via FLUENT CFD Code, and the results are embedded into the developed design procedure. The aerodynamic performance of the designed fan is simulated for the design rotational speed and an increased rotational speed, results of which are compared with the similitude analysis.

#### **5.2. Aerodynamic Performance of Blade Cascades**

The aerodynamic performances of the blade profiles are acquired via CFD analysis. The symmetrical elliptical blade profiles located as a linear cascade are exposed to air streams, velocities of which range from 10 m/s to 100 m/s. The incidences of the

blades are also changed as well as the solidity. The lift and drag coefficients of the profiles are obtained for combinations of the above variables, air stream velocity, solidity and angle of attack. From the results, it can be concluded that lift coefficient is affected adversely with increase in solidity. The drag force is observed to be decreasing as the solidity increases. The ratio of the lift forces to drag forces show that the optimum solidity is around 0.5 and the incidence is around  $10^\circ$ . The change of the incoming air velocity does not affect the coefficient magnitudes significantly. The increase of the incidences results in increased lift and drag coefficients as expected but after optimum values, the drag coefficients increase more rapidly and the lift to drag ratio start to decrease from these points onwards. These optimum values correspond to the angles when the air stream separates from the suction surfaces just after the leading edge of the airfoil. The operation after the separation point should be avoided due to loss of performance and control on the airfoil. It is remarkable to note that when the fan is operating for lower flow rates than the design rate, the incoming air velocity onto the blades decreases. The most important consequence of this phenomenon is the increase of the incidence angle of the blades that are set for the design range. The separation of the flow over the blades takes place for these increased incidences, meaning that the fan is operating in the stalling range.

### **5.3. Reversible Axial Fan Design**

The reversible axial fan is designed for ventilation purposes in underground transportation systems, mines etc. Total pressure rise of 532 Pa, volumetric flowrate of  $80\text{m}^3/\text{s}$  and rotational speed of 1000 rpm are selected as design parameters, which are typical for an emergency ventilation fan of a metro tunnel. The key point on the design of an axial fan is to obtain the flow deflection at the exit of the rotor for the required pressure rise. In standard axial fan applications, flow deflection is mainly provided by the camber of the blades but in reversible fan application, the blade profiles do not have camber so the only source of flow deflection is the proper blade settings. In these applications, the effect of the deviation angle on the rotor

performance becomes more significant than standard axial fan applications and this variable should be carefully embedded into the design procedure. In the developed design procedure, deviation values are obtained from the CFD analysis of the linear cascades for corresponding incidence angle and solidity, and used for the evaluation of the blade settings. The challenging point of the design is to adapt the incidence values, which have already been restricted by the blade shape and necessary deflection parameters (tangential velocity component, fluid angle at the outlet of the rotor etc) and update them considering the deviation angles. When the incidence angles are updated, corresponding deviation angles also change, resulting in a new change in incidence parameter. This iterative solution converges to a specific value where the changes in incidences and deviations have little influence on each other. The solutions are obtained for every solidity value on three radial locations, hub, mean and tip diameters. The solidities that give the maximum blading efficiencies are selected to decide on the chord lengths of the blades at the specified radial locations.

#### **5.4. Performance Analysis of the Reversible Axial Fan**

The performance analysis of the reversible axial fan, which is designed by the developed procedure, is carried by FLUENT 6.0. The geometrical model of the fan and the computational mesh are constructed in Gambit 2.0 which are then exported to the CFD code, FLUENT. The solutions are obtained for several operating conditions, simply by changing the pressure boundary conditions at the fan outlet. Thus, a family of points is collected to form the fan performance curve. The resulting fan curve mainly displays the operating range, the stalling point, and the stalled operation range. When the performance curve is examined at the design point, which is 532 Pa total pressure rise and 80 m<sup>3</sup>/s, the simulation gave a quite close result, which is 528.5 Pa of total pressure rise for 80 m<sup>3</sup>/s flow rate. During the computational runs for the performance analysis, the solutions within the operation range of the fan had no problems in terms of convergence and stability while several difficulties are faced in terms of convergence when the fan is operating in the stalling

range. When these difficulties are faced, the solution adaptive grid refinement, which is introduced in Chapter 1, is performed in the regions where the gradients are high, which lead the solution to divergence and promote instability. The increased number of cells and nodes in high-pressure gradient areas are found to be the solution to convergence problems. Furthermore, the fan was also operated at an increased rotational speed of 1200 rpm. When the solutions are compared with the similitude analysis, it is observed that the simulations yield results that are close enough to those of similitude analysis in the operation range but little discrepancy is observed in the stalling range due to highly distorted nature of the flow in this region but still it can be concluded that the solutions are consistent.

### **5.5. Recommendations for Future Work**

A methodology of reversible axial fan design is established and the aerodynamic performance is tested by CFD techniques. During the fan design, aerodynamic parameters for the blade profiles are acquired for a limited number of solidity values. The intermediate solidities should be increased for more efficient solidity selections. Furthermore, the blade twist is obtained by constructing the blade angles on three radial locations. For a more thorough design, the blade angles should be calculated for increased number of radial locations. The aerodynamic performance of the fan should also be obtained experimentally and the results should be compared with those of the CFD analysis to conclude that the fan meets the design requirements.

## REFERENCES

- [1] Ferziger, J.H., Peric M., “Computational Methods for Fluid Dynamics”, Springer-Verlag, 1996.
- [2] Fluent 6.0 Documentation, FLUENT INC.
- [3] Hinze, J.O., “Turbulence”, McGraw-Hill, 1975.
- [4] Jaw, S.Y., Chen, C.J., “Present Status of Second Order Closure Turbulence Models”, Journal of Engineering Mechanics, May 1998, pp 485-501.
- [5] Wilcox, D.C., “Turbulence Modeling for CFD”, DCW Industries, 1998.
- [6] Taylor, G.I., “Statistical Theory of Turbulence”, Proc. R. Soc.Lond. Vol. A152, 1935, p421.
- [7] Ahmed, N., Yilbas, B.S., Budair, M.O., “Computational Study into the Flow Field Developed Around a Cascade of NACA 0012 Airfoils”, Computational Methods in Applied Mechanics and Engineering, 167, 1998, pp 17-32.
- [8] Christophel, J.R., Thole, K.A., Cunha F.J., “Cooling the Tip of a Turbine Blade Using Pressure Side Holes- Part1: Adiabatic Effectiveness Measurements”, Proceedings of ASME Turbo Expo 2004, Power for Land, Sea, and Air, June 2004.
- [9] Catalano, P., Amato, M., “An Evaluation of RANS Turbulence Modeling for Aerodynamic Applications”, Aerospace Science and Technology, Vol. 7, 2003, pp 493-509.
- [10] Bonhaus, D.L., Anderson, W.K. “An Implicit Upwind Algorithm for Computing Turbulent Flows on Unstructured Grids”, Computers Fluids, Vol.23, 1994, pp 1-21.

- [11] Xu, C., “Numerical Study of Flow and Heat Transfer in Turbomachinery” Ph.D. Dissertation, The University of Wisconsin-Milwaukee, December 2000.
- [12] Pereira, L.A.A., Hirata, M.H., Filho, N.M., “Wake and Aerodynamics Loads in Multiple Bodies- Application to Turbomachinery Blade Rows”, *Journal of Wind Engineering and Industrial Aerodynamics*, Vol.92, 2004, pp 477-491.
- [13] Tulapurkara, E.G., “Turbulence Models for the Computation of Flow Past Airplanes”, *Prog. Aerospace Sci.* Vol. 33, 1997, pp 71-165.
- [14] Hayashibara, S., “Cascade Flow Simulation and Measurement for the Study of Axial Compressor Loss Mechanism”, Ph.D. Dissertation, Wichita State University, 2003.
- [15] Yilbas, B.S., Budair, M.O., Ahmed, N., “Numerical Simulation of the Flow Field Around a Cascade of NACA 0012 Airfoils- Effects of Solidity and Stagger”, *Computational Methods in Applied Mechanics and Engineering*, 158, 1998, pp 143-154.
- [16] AGARD Lecture Series 195, “Turbomachinery Design Using CFD”, May 1994.
- [17] Oh, K.J., Kang, S.H., “A Numerical Investigation of the Dual Performance Characteristics of a Small Propeller Fan Using Viscous Flow Calculations”, *Computers and Fluids*, Vol. 28, 1999, pp 815-823.
- [18] Yan, J., Smith, D.G., “CFD Simulations of 3-Dimensional Flow in Turbomachinery Applications”, *Turbomachinery Flow Prediction VIII ERCOFTAC Workshop*, March 2000.
- [19] Corsini, A., Rispoli, F., “Flow Analyses in a High-Pressure Axial Ventilation Fan with a Non-Linear Eddy Viscosity Closure”, *International Journal of Heat and Fluid Flow*, 2004.
- [20] Lin, S.C., Huang, C.L., “An Integrated Experimental and Numerical Study of Forward-Curved Centrifugal Fan”, *Experimental Thermal and Fluid Science*, Vol.26, 2002, pp 421-434.
- [21] Thakker, A., Hourigan, F., “Computational Fluid Dynamics Analyses of a 0.6 m, 0.6 Hub-to-Tip Ratio Impulse Turbine with Fixed Guide Vanes”, *Renewable Energy*, 2004.
- [22] Widmann, J.F., Charagundla, S.R., Presser, C., “Aerodynamic Study of a Vane-Cascade Swirl Generator”, *Chemical Engineering Science*, Vol.55, 2000 pp 5311-5320.

- [23] Danczyk, S.A., "Experimental and Computational Investigation of the Flow Field Inside an Axial Fan", Ph. D. Dissertation, Texas A&M University, December 2002.
- [24] Bleier, F.P., "Fan Handbook: Selection, Application and Design", McGraw-Hill, 1998.
- [25] MacRunnel, T.M., "Vaneaxial Fan Design and Sizing Using 3D-CAD Modeling Software", M.S. Thesis, California State University, Long Beach, Department of Mechanical Engineering, May 1997.
- [26] Eck, B., "Fans", Pergamon Press, 1973.
- [27] Wallis, R.A., "Axial Flow Fans and Ducts", John Wiley and Sons, 1983.
- [28] ZITRON Ventilation Fans Catalogue.
- [29] Glauert, H., "The Elements of Aerofoil and Airscrew Theory", Cambridge University Press, 1947.
- [30] Gostelow, J.P., "Cascade Aerodynamics", Pergamon Press, 1984.
- [31] Abbot, I.H., Von Doenhoff, A.E., "Theory of Wing Sections", Dover Publications, 1959.
- [32] Riegels, S.F.W., "Aerofoil Sections", London Butterworths, 1961.
- [33] Sayers, A.T., "Hydraulic and Compressible Flow Turbomachines", McGraw-Hill, 1990.
- [34] Saravanamuttoo, H.I.H., Rogers, G.F.C., Cohen, H., "Gas Turbine Theory", Prentice Hall, 2001.
- [35] Horlock, J.H., "Axial Flow Compressors, Fluid Mechanics & Thermodynamics", Robert E. Krieger Publishing Co., 1973.
- [36] Kovats, A., Desmur, G., "Pumps, Fans and Compressors", Blackie and Son Ltd., 1958.
- [37] Osborne, W.C., "Fans", Pergamon Press, 1977.
- [38] Stepanoff, A.J., "Turboblowers; Theory, Design and Application of Centrifugal and Axial Flow Compressors and Fans", John Wiley and Sons, 1955.

- [39] Ülgen, N.S., “Design, Construction and Testing of an Axial Flow Fan for the Low Speed Wind Tunnel in Mechanical Engineering Department of METU”, M.S. Thesis, Middle East Technical University, February 1981.
- [40] Wilson, D.G., Korakianitis, T., “The Design of High Efficiency Turbomachinery and Gas Turbines”, Prentice Hall, 1998.
- [41] Dubois, T., Jauberteau, F., Temam,R., “Dynamic Multilevel Methods and the Numerical Simulation of Turbulence”, Cambridge University Press, 1999.
- [42] Durbin, P.A., Pettersson Reif, B.A., “Statistical Theory and Modeling of Turbulent Flows”, John Wiley and Sons, 2000.
- [43] Aksel, M.H., “Fluid Mechanics, Volumes I-II”, METU Press, 1999.

## APPENDIX A

### DESIGN FOR HUB AND TIP RADII

#### A.1. Hub Radius Design ( $\sigma=1$ )

The design for the hub diameter with solidity  $\sigma=1$  is presented below. Note that following design is the finalized form of the iterative solution over the efficiency value.

- Calculate axial air velocity

$$V_a = \frac{Q}{\frac{\pi}{4}(D_{fan}^2 - D_{hub}^2)} = \frac{80m^3/s}{\frac{\pi}{4}(2.029^2 - 0.812^2)} = 29.5m/s$$

- Assume efficiency value

$$\eta_{BL} = 0.75$$

- Calculate theoretical nondimensional pressure rise coefficient

$$\Psi_{th} = \frac{H \times \rho_{air} \times g}{\eta_{BL} \times \frac{1}{2} \rho_{air} V_a^2} = \frac{50 \times 1.085 \times 9.81}{0.75 \times \frac{1}{2} (1.085)(29.5^2)} = 1.497$$

- Flow coefficient at the hub diameter is obtained

$$\phi_{hub} = \frac{V_a}{N \frac{2\pi}{60} \frac{D_{hub}}{2}} = \frac{29.5}{1000 \frac{2\pi}{60} \frac{0.812}{2}} = 0.693$$

- For a swirl free inlet,

$$\varepsilon_2 = \frac{\Psi_{th} \times \phi_{hub}}{2} = \frac{1.497 \times 0.693}{2} = 0.519$$

- Relative fluid angle at the inlet to the rotor

$$\beta_1 = \arctan\left(\frac{1}{\phi_{hub}}\right) = \arctan\left(\frac{1}{0.519}\right) = 55.3^\circ$$

- Relative fluid angle at the exit to the rotor

$$\beta_2 = \arctan\left(\frac{1 - \varepsilon_2 \phi_{hub}}{\phi_{hub}}\right) = \arctan\left(\frac{1 - 0.519 \times 0.693}{0.693}\right) = 42.7^\circ$$

- Mean fluid angle through the blade

$$\beta_m = \arctan\left(\frac{\tan \beta_1 + \tan \beta_2}{2}\right) = \arctan\left(\frac{\tan 55.3 + \tan 42.7}{2}\right) = 49.8^\circ$$

- Incidence can be first written as

$$i = \beta_1 - \beta_2 = 55.3^\circ - 42.7^\circ = 12.6^\circ$$

- The deviation angle can be acquired from two-dimensional cascade data. For the solidity that is being investigated and the above incidence, the deviation angle is negligible. The blade angles are constructed to give the desired deflection angle as follows:

$$\beta_{2k} = \beta_2 - \delta = 42.7^\circ - 0^\circ = 42.7^\circ$$

$$\beta_{1k} = \beta_{2k} = 42.7^\circ$$

$$i_{\text{mod}} = \beta_1 - \beta_{1k} = 55.3^\circ - 42.7^\circ = 12.6^\circ$$

- For the modified incidence, the aerodynamic coefficients are read from the related graphs.

$$C_L = 0.431 \quad \text{and} \quad C_{DP} = 0.049$$

- Secondary drag is obtained with information  $C_L$  and annulus drag is obtained with information of  $s$  and  $h$  from Eq(80) and Eq(81).

$$C_{DS} = 0.018C_L^2 = 0.018 \times 0.431^2 = 0.0033$$

$$C_{DA} = 0.02 \frac{s}{h} = 0.02 \frac{0.364}{0.609} = 0.012$$

- Total drag is calculated

$$C_D = C_{DP} + C_{DS} + C_{DA} = 0.049 + 0.0033 + 0.012 = 0.064$$

- Rotor loss is computed

$$\Psi_R = \Psi_{th} \frac{C_D}{C_L} \frac{\phi_{hub}}{\cos(\beta_m)^2} = 1.497 \frac{0.064}{0.431} \frac{0.693}{\cos(49.8)^2} = 0.372$$

- Efficiency is determined

$$\eta_{BL} = 1 - \frac{\Psi_R}{\Psi_{th}} = 1 - \frac{0.372}{1.497} = 0.75 \quad \text{The efficiency value is converged.}$$

- With solidity  $\sigma = 1$ , the blade chord is calculated at hub radius

$$c = \sigma \times s = 1 \times 0.364 = 0.364m = 36.4cm$$

## A.2. Tip Radius Design ( $\sigma=0.2$ )

The design for the tip diameter with solidity  $\sigma=0.2$  is presented below. Note that following design is the finalized form of the iterative solution over the efficiency value.

- Calculate axial air velocity

$$V_a = \frac{Q}{\frac{\pi}{4}(D_{fan}^2 - D_{hub}^2)} = \frac{80m^3/s}{\frac{\pi}{4}(2.029^2 - 0.812^2)} = 29.5m/s$$

- Assume efficiency value

$$\eta_{BL} = 0.29$$

- Calculate theoretical nondimensional pressure rise coefficient

$$\Psi_{th} = \frac{H \times \rho_{air} \times g}{\eta_{BL} \times \frac{1}{2} \rho_{air} V_a^2} = \frac{50 \times 1.085 \times 9.81}{0.29 \times \frac{1}{2} (1.085)(29.5^2)} = 3.898$$

- Flow coefficient at the tip diameter is obtained

$$\phi_{tip} = \frac{V_a}{N \frac{2\pi}{60} \frac{D_{tip}}{2}} = \frac{29.5}{1000 \frac{2\pi}{60} \frac{2.03}{2}} = 0.277$$

- For a swirl free inlet,

$$\varepsilon_2 = \frac{\Psi_{th} \times \phi_{tip}}{2} = \frac{3.898 \times 0.277}{2} = 0.54$$

- Relative fluid angle at the inlet to the rotor

$$\beta_1 = \text{arc tan} \left( \frac{1}{\phi_{tip}} \right) = \text{arc tan} \left( \frac{1}{0.277} \right) = 74.5^\circ$$

- Relative fluid angle at the exit to the rotor

$$\beta_2 = \text{arc tan} \left( \frac{1 - \varepsilon_2 \phi_{tip}}{\phi_{tip}} \right) = \text{arc tan} \left( \frac{1 - 0.54 \times 0.277}{0.277} \right) = 71.9^\circ$$

- Mean fluid angle through the blade

$$\beta_m = \text{arc tan} \left( \frac{\tan \beta_1 + \tan \beta_2}{2} \right) = \text{arc tan} \left( \frac{\tan 74.5 + \tan 71.9}{2} \right) = 73.3^\circ$$

- Incidence can be first written as

$$i = \beta_1 - \beta_2 = 74.5 - 71.9 = 2.6^\circ$$

- The deviation angle can be acquired from two-dimensional cascade data. For the solidity that is being investigated and the above incidence, the

deviation angle is  $\delta = 1.8^\circ$ . The blade angles are constructed to give the desired deflection angle as follows:

$$\beta_{2k} = \beta_2 - \delta = 71.9^\circ - 1.8^\circ = 70.1^\circ$$

$$\beta_{1k} = \beta_{2k} = 70.1^\circ$$

$$i_{\text{mod}} = \beta_1 - \beta_{1k} = 74.5^\circ - 70.1^\circ = 4.4^\circ$$

- For the modified incidence, the aerodynamic coefficients are read from the related graphs.

$$C_L = 0.335 \quad \text{and} \quad C_{DP} = 0.0395$$

- Secondary drag is obtained with information of  $C_L$  and annulus drag is obtained with the information of  $s$  and  $h$  from Eq(80) and Eq(81).

$$C_{DS} = 0.018C_L^2 = 0.018 \times 0.335^2 = 0.002$$

$$C_{DA} = 0.02 \frac{s}{h} = 0.02 \frac{0.911}{0.609} = 0.03$$

- Total drag is calculated

$$C_D = C_{DP} + C_{DS} + C_{DA} = 0.0395 + 0.002 + 0.03 = 0.072$$

- Rotor loss is computed

$$\Psi_R = \Psi_{th} \frac{C_D}{C_L} \frac{\phi_{tip}}{\cos(\beta_m)^2} = 3.898 \frac{0.072}{0.335} \frac{0.277}{\cos(73.3)^2} = 2.795$$

- Efficiency is determined

$$\eta_{BL} = 1 - \frac{\Psi_R}{\Psi_{th}} = 1 - \frac{2.795}{3.898} = 0.28 \quad \text{The efficiency value is converged.}$$

- With solidity  $\sigma = 0.2$ , the blade chord is calculated at tip radius

$$c = \sigma \times s = 0.2 \times 0.911 = 0.182m = 18.2cm$$

## APPENDIX B

### RESULTS FOR BLADE PERFORMANCE ANALYSIS

#### B.1. Solidity $\sigma=0.1$

**Table B1.1:** Aerodynamic Performance for  $V=10\text{m/s}$ ,  $\sigma=0.1$

	Angle of Attack	The Coefficients in X-Y direction		Measuring section parameters			Mean Velocity Properties		Projection of the coefficients on mean velocity direction		
		Lift Coeff.	Drag Coeff.	Y velocity (m/s)	X velocity (m/s)	Velocity Direction (°)	Direction (°)	Magnitude (m/s)	Lift Coeff.	Drag Coeff.	L/D
Velocity=10 m/s	0 degree	0,000	0,045	10,0	0,0	0,00	0,0	10,0	0,000	0,045	0,000
	5 degree	0,397	0,068	10,0	0,2	1,13	0,6	10,0	0,398	0,064	6,188
	10 degree	0,720	0,137	10,0	0,4	2,06	1,0	10,0	0,722	0,124	5,824
	15 degree	0,942	0,248	10,0	0,5	2,69	1,3	10,0	0,947	0,226	4,196
	20 degree	1,082	0,408	10,0	0,5	3,09	1,5	10,0	1,092	0,378	2,886
	25 degree	1,141	0,581	10,0	0,6	3,26	1,6	10,0	1,156	0,548	2,110
	30 degree	1,170	0,746	10,0	0,6	3,32	1,7	10,0	1,190	0,711	1,673

**Table B1.2:** Aerodynamic Performance for  $V=30\text{m/s}$ ,  $\sigma=0.1$

	Angle of Attack	The Coefficients in X-Y direction		Measuring section parameters			Mean Velocity Properties		Projection of the coefficients on mean velocity direction		
		Lift Coeff.	Drag Coeff.	Y velocity (m/s)	X velocity (m/s)	Velocity Direction (°)	Direction (°)	Magnitude (m/s)	Lift Coeff.	Drag Coeff.	L/D
Velocity=30 m/s	0 degree	0,000	0,035	30,0	0,0	0,00	0,0	30,0	0,000	0,035	0,000
	5 degree	0,409	0,060	30,0	0,6	1,16	0,6	30,0	0,410	0,056	7,335
	10 degree	0,709	0,129	30,0	1,1	2,02	1,0	30,0	0,711	0,116	6,107
	15 degree	0,924	0,242	30,0	1,4	2,63	1,3	30,0	0,929	0,221	4,211
	20 degree	1,070	0,407	30,0	1,6	3,05	1,5	30,0	1,080	0,378	2,856
	25 degree	1,131	0,578	30,0	1,7	3,22	1,6	30,0	1,146	0,545	2,101
	30 degree	1,162	0,740	30,0	1,7	3,28	1,6	30,0	1,182	0,706	1,674

**Table B1.3:** Aerodynamic Performance for  $V=50\text{m/s}$ ,  $\sigma=0.1$

	Angle of Attack	The Coefficients in X-Y direction		Measuring section parameters			Mean Velocity Properties		Projection of the coefficients on mean velocity direction		
		Lift Coeff.	Drag Coeff.	Y velocity (m/s)	X velocity (m/s)	Velocity Direction (°)	Direction (°)	Magnitude (m/s)	Lift Coeff.	Drag Coeff.	L/D
Velocity=50 m/s	0 degree	0,000	0,031	50,0	0,0	0,00	0,0	50,0	0,000	0,031	0,000
	5 degree	0,422	0,057	50,0	1,1	1,20	0,6	50,0	0,423	0,053	8,039
	10 degree	0,709	0,125	50,0	1,8	2,03	1,0	50,0	0,711	0,112	6,325
	15 degree	0,915	0,238	50,0	2,3	2,61	1,3	50,0	0,920	0,217	4,239
	20 degree	1,059	0,404	50,0	2,6	3,02	1,5	50,0	1,069	0,376	2,845
	25 degree	1,121	0,575	50,0	2,8	3,21	1,6	50,0	1,136	0,543	2,092
	30 degree	1,157	0,738	50,0	2,9	3,30	1,6	50,0	1,177	0,704	1,672

**Table B1.4:** Aerodynamic Performance for  $V=70\text{m/s}$ ,  $\sigma=0.1$

	Angle of Attack	The Coefficients in X-Y direction		Measuring section parameters			Mean Velocity Properties		Projection of the coefficients on mean velocity direction		
		Lift Coeff.	Drag Coeff.	Y velocity (m/s)	X velocity (m/s)	Velocity Direction (°)	Direction (°)	Magnitude (m/s)	Lift Coeff.	Drag Coeff.	L/D
Velocity=70 m/s	0 degree	0,000	0,029	70,0	0,0	0,00	0,0	70,0	0,000	0,029	0,000
	5 degree	0,410	0,054	70,0	1,4	1,16	0,6	70,0	0,410	0,050	8,237
	10 degree	0,692	0,120	70,0	2,4	1,97	1,0	70,0	0,694	0,108	6,421
	15 degree	0,908	0,235	70,0	3,2	2,59	1,3	70,0	0,913	0,214	4,259
	20 degree	1,050	0,402	70,0	3,7	3,00	1,5	70,0	1,059	0,374	2,832
	25 degree	1,119	0,574	70,0	3,9	3,19	1,6	70,0	1,134	0,542	2,091
	30 degree	1,155	0,735	70,0	4,0	3,29	1,6	70,0	1,175	0,701	1,676

**Table B1.5:** Aerodynamic Performance for  $V=100\text{m/s}$ ,  $\sigma=0.1$

	Angle of Attack	The Coefficients in X-Y direction		Measuring section parameters			Mean Velocity Properties		Projection of the coefficients on mean velocity direction		
		Lift Coeff.	Drag Coeff.	Y velocity (m/s)	X velocity (m/s)	Velocity Direction (°)	Direction (°)	Magnitude (m/s)	Lift Coeff.	Drag Coeff.	L/D
Velocity=100 m/s	0 degree	0,000	0,027	100,0	0,0	0,00	0,0	100,0	0,000	0,027	0,000
	5 degree	0,398	0,051	100,0	2,0	1,14	0,6	100,0	0,398	0,047	8,472
	10 degree	0,688	0,120	100,0	3,4	1,96	1,0	100,0	0,690	0,108	6,378
	15 degree	0,898	0,233	100,0	4,5	2,56	1,3	100,0	0,903	0,213	4,242
	20 degree	1,048	0,403	100,0	5,2	2,99	1,5	100,0	1,057	0,375	2,818
	25 degree	1,116	0,573	100,0	5,6	3,18	1,6	100,0	1,131	0,541	2,089
	30 degree	1,148	0,733	100,0	5,7	3,28	1,6	100,0	1,168	0,699	1,670

## B.2. Solidity $\sigma=0.2$

**Table B2.1:** Aerodynamic Performance for  $V=10\text{m/s}$ ,  $\sigma=0.2$

Velocity= 10 m/s	Angle of Attack	The Coefficients in X-Y direction		Measuring section parameters			Mean Velocity Properties		Projection of the coefficients on mean velocity direction		
		Lift Coeff.	Drag Coeff.	Y velocity (m/s)	X velocity (m/s)	Velocity Direction ( $^{\circ}$ )	Direction ( $^{\circ}$ )	Magnitude (m/s)	Lift Coeff.	Drag Coeff.	L/D
	0 degree	0,000	0,041	10,0	0,000	0,00	0,0	10,00	0,000	0,041	0,000
	5 degree	0,360	0,063	10,0	0,360	2,06	1,0	10,00	0,361	0,056	6,389
	10 degree	0,664	0,126	10,0	0,663	3,79	1,9	10,01	0,667	0,104	6,425
	15 degree	0,871	0,230	10,0	0,870	4,97	2,5	10,01	0,879	0,192	4,586
	20 degree	0,988	0,382	10,0	0,983	5,61	2,8	10,01	1,003	0,332	3,019
	25 degree	1,031	0,537	10,0	1,023	5,84	2,9	10,01	1,054	0,482	2,186
	30 degree	1,080	0,697	10,0	1,065	6,08	3,0	10,01	1,112	0,637	1,747

**Table B2.2:** Aerodynamic Performance for  $V=30\text{m/s}$ ,  $\sigma=0.2$

Velocity= 30 m/s	Angle of Attack	The Coefficients in X-Y direction		Measuring section parameters			Mean Velocity Properties		Projection of the coefficients on mean velocity direction		
		Lift Coeff.	Drag Coeff.	Y velocity (m/s)	X velocity (m/s)	Velocity Direction ( $^{\circ}$ )	Direction ( $^{\circ}$ )	Magnitude (m/s)	Lift Coeff.	Drag Coeff.	L/D
	0 degree	0,000	0,033	30,0	0,000	0,00	0,0	30,00	0,000	0,033	0,000
	5 degree	0,373	0,055	30,0	1,120	2,14	1,1	30,01	0,374	0,048	7,786
	10 degree	0,654	0,119	30,0	1,960	3,74	1,9	30,02	0,657	0,097	6,738
	15 degree	0,851	0,223	30,0	2,540	4,84	2,4	30,03	0,858	0,186	4,602
	20 degree	0,977	0,381	30,0	2,913	5,55	2,8	30,04	0,992	0,332	2,984
	25 degree	1,023	0,534	30,0	3,045	5,80	2,9	30,04	1,046	0,480	2,178
	30 degree	1,074	0,692	30,0	3,171	6,03	3,0	30,04	1,106	0,633	1,748

**Table B2.3:** Aerodynamic Performance for  $V=50\text{m/s}$ ,  $\sigma=0.2$

Velocity= 50 m/s	Angle of Attack	The Coefficients in X-Y direction		Measuring section parameters			Mean Velocity Properties		Projection of the coefficients on mean velocity direction		
		Lift Coeff.	Drag Coeff.	Y velocity (m/s)	X velocity (m/s)	Velocity Direction ( $^{\circ}$ )	Direction ( $^{\circ}$ )	Magnitude (m/s)	Lift Coeff.	Drag Coeff.	L/D
	0 degree	0,000	0,029	50,0	0,000	0,00	0,0	50,00	0,000	0,029	0,000
	5 degree	0,384	0,052	50,0	1,920	2,20	1,1	50,01	0,385	0,045	8,627
	10 degree	0,652	0,115	50,0	3,250	3,72	1,9	50,03	0,655	0,094	6,990
	15 degree	0,848	0,221	50,0	4,230	4,84	2,4	50,04	0,855	0,185	4,631
	20 degree	0,967	0,379	50,0	2,410	2,76	1,4	50,01	0,975	0,355	2,744
	25 degree	1,018	0,532	50,0	3,045	3,49	1,7	50,02	1,033	0,500	2,064
	30 degree	1,067	0,688	50,0	5,266	6,01	3,0	50,07	1,099	0,629	1,746

**Table B2.4:** Aerodynamic Performance for  $V=70\text{m/s}$ ,  $\sigma=0.2$

	The Coefficients in X-Y direction	Measuring section parameters			Mean Velocity Properties		Projection of the coefficients on mean velocity direction				
		Lift Coeff.	Drag Coeff.	Y velocity (m/s)	X velocity (m/s)	Velocity Direction (°)	Direction (°)	Magnitude (m/s)	Lift Coeff.	Drag Coeff.	L/D
Velocity=70 m/s	Angle of Attack										
	0 degree	0,000	0,027	70,0	0,000	0,00	0,0	70,00	0,000	0,027	0,000
	5 degree	0,376	0,050	70,0	2,710	2,22	1,1	70,01	0,377	0,043	8,824
	10 degree	0,640	0,111	70,0	4,463	3,65	1,8	70,04	0,643	0,090	7,103
	15 degree	0,839	0,218	70,0	5,860	4,79	2,4	70,06	0,846	0,182	4,638
	20 degree	0,964	0,378	70,0	6,710	5,48	2,7	70,08	0,979	0,331	2,960
	25 degree	1,013	0,529	70,0	7,040	5,74	2,9	70,09	1,036	0,476	2,175
30 degree	1,066	0,688	70,0	7,360	6,00	3,0	70,10	1,098	0,629	1,744	

**Table B2.5:** Aerodynamic Performance for  $V=100\text{m/s}$ ,  $\sigma=0.2$

	The Coefficients in X-Y direction	Measuring section parameters			Mean Velocity Properties		Projection of the coefficients on mean velocity direction				
		Lift Coeff.	Drag Coeff.	Y velocity (m/s)	X velocity (m/s)	Velocity Direction (°)	Direction (°)	Magnitude (m/s)	Lift Coeff.	Drag Coeff.	L/D
Velocity=100 m/s	Angle of Attack										
	0 degree	0,000	0,025	100,0	0,000	0,00	0,0	100,00	0,000	0,025	0,000
	5 degree	0,364	0,047	100,0	3,640	2,08	1,0	100,02	0,365	0,040	9,037
	10 degree	0,635	0,110	100,0	6,330	3,62	1,8	100,05	0,638	0,090	7,102
	15 degree	0,835	0,218	100,0	8,320	4,76	2,4	100,09	0,842	0,183	4,606
	20 degree	0,961	0,379	100,0	9,550	5,46	2,7	100,11	0,976	0,332	2,939
	25 degree	1,011	0,529	100,0	10,040	5,73	2,9	100,13	1,034	0,476	2,169
30 degree	1,059	0,684	100,0	10,450	5,97	3,0	100,14	1,090	0,626	1,741	

### B.3. Solidity $\sigma=0.5$

**Table B3.1:** Aerodynamic Performance for  $V=10\text{m/s}$ ,  $\sigma=0.5$

	The Coefficients in X-Y direction	Measuring section parameters			Mean Velocity Properties		Projection of the coefficients on mean velocity direction				
		Lift Coeff.	Drag Coeff.	Y velocity (m/s)	X velocity (m/s)	Velocity Direction (°)	Direction (°)	Magnitude (m/s)	Lift Coeff.	Drag Coeff.	L/D
Velocity=10 m/s	Angle of Attack										
	0 degree	0,000	0,039	10,0	0,000	0,00	0,0	10,00	0,000	0,039	0,000
	5 degree	0,261	0,054	10,0	0,650	3,72	1,9	10,01	0,262	0,045	5,773
	10 degree	0,515	0,102	10,0	1,290	7,35	3,7	10,02	0,518	0,068	7,583
	15 degree	0,737	0,187	10,0	1,840	10,43	5,3	10,04	0,745	0,118	6,327
	20 degree	0,917	0,331	10,0	2,280	12,84	6,5	10,06	0,936	0,222	4,216
	25 degree	1,059	0,542	10,0	2,620	14,68	7,5	10,09	1,102	0,393	2,802
30 degree	1,206	0,773	10,0	2,980	16,59	8,5	10,11	1,278	0,574	2,227	

**Table B3.2:** Aerodynamic Performance for  $V=30\text{m/s}$ ,  $\sigma=0.5$

	The Coefficients in X-Y direction	Measuring section parameters			Mean Velocity Properties		Projection of the coefficients on mean velocity direction				
		Lift Coeff.	Drag Coeff.	Y velocity (m/s)	X velocity (m/s)	Velocity Direction (°)	Direction (°)	Magnitude (m/s)	Lift Coeff.	Drag Coeff.	L/D
Velocity=30 m/s	Angle of Attack										
	0 degree	0,000	0,030	30,0	0,000	0,00	0,0	30,00	0,000	0,030	0,000
	5 degree	0,263	0,046	30,0	1,970	3,76	1,9	30,02	0,264	0,037	7,079
	10 degree	0,514	0,095	30,0	3,850	7,31	3,7	30,06	0,517	0,062	8,386
	15 degree	0,724	0,180	30,0	5,430	10,26	5,2	30,12	0,731	0,113	6,467
	20 degree	0,907	0,332	30,0	6,790	12,75	6,5	30,19	0,927	0,225	4,118
	25 degree	1,052	0,540	30,0	7,820	14,61	7,4	30,25	1,094	0,393	2,786
30 degree	1,198	0,768	30,0	8,860	16,45	8,4	30,33	1,270	0,572	2,219	

**Table B3.3:** Aerodynamic Performance for  $V=50\text{m/s}$ ,  $\sigma=0.5$

	The Coefficients in X-Y direction	Measuring section parameters			Mean Velocity Properties		Projection of the coefficients on mean velocity direction				
		Lift Coeff.	Drag Coeff.	Y velocity (m/s)	X velocity (m/s)	Velocity Direction (°)	Direction (°)	Magnitude (m/s)	Lift Coeff.	Drag Coeff.	L/D
Velocity=50 m/s	Angle of Attack										
	0 degree	0,000	0,027	50,0	0,000	0,00	0,0	50,00	0,000	0,027	0,000
	5 degree	0,269	0,043	50,0	3,360	3,84	1,9	50,03	0,270	0,034	7,963
	10 degree	0,523	0,092	50,0	6,530	7,44	3,7	50,11	0,526	0,057	9,145
	15 degree	0,729	0,178	50,0	9,100	10,31	5,2	50,21	0,736	0,110	6,674
	20 degree	0,901	0,330	50,0	11,220	12,65	6,4	50,31	0,921	0,225	4,098
	25 degree	1,040	0,536	50,0	12,930	14,50	7,4	50,42	1,082	0,392	2,763
30 degree	1,183	0,757	50,0	14,570	16,25	8,3	50,53	1,253	0,567	2,212	

**Table B3.4:** Aerodynamic Performance for  $V=70\text{m/s}$ ,  $\sigma=0.5$

	The Coefficients in X-Y direction	Measuring section parameters			Mean Velocity Properties		Projection of the coefficients on mean velocity direction				
		Lift Coeff.	Drag Coeff.	Y velocity (m/s)	X velocity (m/s)	Velocity Direction (°)	Direction (°)	Magnitude (m/s)	Lift Coeff.	Drag Coeff.	L/D
Velocity=70 m/s	Angle of Attack										
	0 degree	0,000	0,025	70,0	0,000	0,00	0,0	70,00	0,000	0,025	0,000
	5 degree	0,264	0,041	70,0	4,620	3,78	1,9	70,04	0,265	0,032	8,218
	10 degree	0,519	0,090	70,0	9,080	7,39	3,7	70,15	0,522	0,056	9,316
	15 degree	0,718	0,174	70,0	12,570	10,18	5,1	70,28	0,725	0,108	6,698
	20 degree	0,896	0,329	70,0	15,620	12,58	6,4	70,43	0,916	0,225	4,072
	25 degree	1,034	0,533	70,0	17,920	14,36	7,3	70,57	1,076	0,391	2,751
30 degree	1,180	0,756	70,0	20,390	16,24	8,3	70,74	1,250	0,566	2,209	

**Table B3.5:** Aerodynamic Performance for  $V=100\text{m/s}$ ,  $\sigma=0.5$

		The Coefficients in X-Y direction		Measuring section parameters			Mean Velocity Properties		Projection of the coefficients on mean velocity direction		
Velocity=100 m/s	Angle of Attack	Lift Coeff.	Drag Coeff.	Y velocity (m/s)	X velocity (m/s)	Velocity Direction (°)	Direction (°)	Magnitude (m/s)	Lift Coeff.	Drag Coeff.	L/D
	0 degree	0,000	0,022	100,0	0,000	0,00	0,0	100,00	0,000	0,022	0,000
	5 degree	0,258	0,038	100,0	6,410	3,67	1,8	100,05	0,259	0,030	8,719
	10 degree	0,510	0,087	100,0	12,720	7,25	3,6	100,20	0,512	0,054	9,448
	15 degree	0,712	0,171	100,0	17,780	10,08	5,1	100,39	0,719	0,106	6,752
	20 degree	0,886	0,327	100,0	22,060	12,44	6,3	100,61	0,905	0,225	4,022
	25 degree	1,029	0,532	100,0	25,540	14,33	7,3	100,81	1,071	0,391	2,738
	30 degree	1,163	0,749	100,0	28,680	16,00	8,2	101,02	1,232	0,565	2,182

**B.4. Solidity  $\sigma=1$**

**Table B4.1:** Aerodynamic Performance for  $V=10\text{m/s}$ ,  $\sigma=1$

		The Coefficients in X-Y direction		Measuring section parameters			Mean Velocity Properties		Projection of the coefficients on mean velocity direction		
Velocity=10 m/s	Angle of Attack	Lift Coeff.	Drag Coeff.	Y velocity (m/s)	X velocity (m/s)	Velocity Direction (°)	Direction (°)	Magnitude (m/s)	Lift Coeff.	Drag Coeff.	L/D
	0 degree	0,000	0,039	10,0	0,002	0,01	0,0	10,00	0,000	0,039	0,000
	5 degree	0,172	0,050	10,0	0,864	4,94	2,5	10,01	0,174	0,042	4,091
	10 degree	0,343	0,083	10,0	1,693	9,61	4,8	10,04	0,346	0,053	6,486
	15 degree	0,517	0,144	10,0	2,539	14,25	7,2	10,08	0,523	0,077	6,830
	20 degree	0,693	0,247	10,0	3,527	19,43	10,0	10,15	0,703	0,119	5,902
	25 degree	0,909	0,421	10,0	4,539	24,41	12,8	10,25	0,932	0,199	4,679
	30 degree	1,215	0,726	10,0	5,893	30,51	16,4	10,43	1,261	0,325	3,883

**Table B4.2:** Aerodynamic Performance for  $V=30\text{m/s}$ ,  $\sigma=1$

		The Coefficients in X-Y direction		Measuring section parameters			Mean Velocity Properties		Projection of the coefficients on mean velocity direction		
Velocity=30 m/s	Angle of Attack	Lift Coeff.	Drag Coeff.	Y velocity (m/s)	X velocity (m/s)	Velocity Direction (°)	Direction (°)	Magnitude (m/s)	Lift Coeff.	Drag Coeff.	L/D
	0 degree	0,000	0,300	30,0	0,002	0,00	0,0	30,00	0,000	0,300	0,000
	5 degree	0,173	0,042	30,0	2,623	5,00	2,5	30,03	0,174	0,034	5,077
	10 degree	0,337	0,073	30,0	5,130	9,70	4,9	30,11	0,340	0,044	7,768
	15 degree	0,506	0,133	30,0	7,710	14,41	7,3	30,25	0,510	0,066	7,695
	20 degree	0,673	0,236	30,0	10,180	18,74	9,6	30,43	0,683	0,117	5,854
	25 degree	0,892	0,416	30,0	13,360	24,00	12,6	30,73	0,916	0,202	4,529
	30 degree	1,215	0,731	30,0	18,240	31,30	16,9	31,36	1,259	0,317	3,974

**Table B4.3:** Aerodynamic Performance for  $V=50\text{m/s}$ ,  $\sigma=1$

	Angle of Attack	The Coefficients in X-Y direction		Measuring section parameters			Mean Velocity Properties		Projection of the coefficients on mean velocity direction		
		Lift Coeff.	Drag Coeff.	Y velocity (m/s)	X velocity (m/s)	Velocity Direction (°)	Direction (°)	Magnitude (m/s)	Lift Coeff.	Drag Coeff.	L/D
Velocity=50 m/s	0 degree	0,000	0,026	50,0	0,000	0,00	0,0	50,00	0,000	0,026	0,000
	5 degree	0,174	0,040	50,0	4,280	4,89	2,5	50,05	0,175	0,032	5,398
	10 degree	0,340	0,070	50,0	8,220	9,34	4,7	50,17	0,342	0,042	8,222
	15 degree	0,510	0,130	50,0	12,340	13,86	7,0	50,38	0,514	0,066	7,844
	20 degree	0,679	0,236	50,0	17,090	18,87	9,7	50,72	0,689	0,115	5,996
	25 degree	0,892	0,417	50,0	22,270	24,01	12,6	51,22	0,916	0,203	4,510
	30 degree	1,210	0,729	50,0	30,300	31,22	16,9	52,24	1,254	0,318	3,949

**Table B4.4:** Aerodynamic Performance for  $V=70\text{m/s}$ ,  $\sigma=1$

	Angle of Attack	The Coefficients in X-Y direction		Measuring section parameters			Mean Velocity Properties		Projection of the coefficients on mean velocity direction		
		Lift Coeff.	Drag Coeff.	Y velocity (m/s)	X velocity (m/s)	Velocity Direction (°)	Direction (°)	Magnitude (m/s)	Lift Coeff.	Drag Coeff.	L/D
Velocity=70 m/s	0 degree	0,001	0,025	70,0	0,002	0,00	0,0	70,00	0,001	0,024	0,023
	5 degree	0,176	0,037	70,0	5,910	4,83	2,4	70,06	0,177	0,029	6,005
	10 degree	0,344	0,068	70,0	11,510	9,34	4,7	70,24	0,346	0,039	8,802
	15 degree	0,510	0,128	70,0	17,230	13,83	7,0	70,53	0,514	0,064	8,060
	20 degree	0,669	0,229	70,0	23,240	18,37	9,4	70,96	0,679	0,113	5,994
	25 degree	0,885	0,412	70,0	30,890	23,81	12,4	71,68	0,909	0,202	4,503
	30 degree	1,210	0,725	70,0	42,520	31,28	16,9	73,16	1,253	0,313	4,000

**Table B4.5:** Aerodynamic Performance for  $V=100\text{m/s}$ ,  $\sigma=1$

	Angle of Attack	The Coefficients in X-Y direction		Measuring section parameters			Mean Velocity Properties		Projection of the coefficients on mean velocity direction		
		Lift Coeff.	Drag Coeff.	Y velocity (m/s)	X velocity (m/s)	Velocity Direction (°)	Direction (°)	Magnitude (m/s)	Lift Coeff.	Drag Coeff.	L/D
Velocity=100 m/s	0 degree	0,003	0,022	100,0	0,030	0,02	0,0	100,00	0,003	0,022	0,116
	5 degree	0,170	0,033	100,0	8,230	4,70	2,4	100,08	0,171	0,026	6,590
	10 degree	0,335	0,065	100,0	16,360	9,29	4,7	100,33	0,337	0,037	9,052
	15 degree	0,500	0,124	100,0	24,520	13,78	7,0	100,75	0,504	0,061	8,217
	20 degree	0,661	0,227	100,0	32,290	17,90	9,2	101,29	0,671	0,116	5,800
	25 degree	0,871	0,410	100,0	43,490	23,50	12,3	102,34	0,896	0,206	4,352
	30 degree	1,170	0,713	100,0	58,290	30,24	16,2	104,16	1,219	0,329	3,704

## B.5. Solidity $\sigma=1.5$

**Table B5.1:** Aerodynamic Performance for  $V=10\text{m/s}$ ,  $\sigma=1.5$

	The Coefficients in X-Y direction	Measuring section parameters			Mean Velocity Properties		Projection of the coefficients on mean velocity direction				
		Lift Coeff.	Drag Coeff.	Y velocity (m/s)	X velocity (m/s)	Velocity Direction (°)	Direction (°)	Magnitude (m/s)	Lift Coeff.	Drag Coeff.	L/D
Velocity=10 m/s	Angle of Attack										
	0 degree	0,001	0,031	10,0	0,010	0,06	0,0	10,0	0,001	0,031	0,033
	5 degree	0,124	0,049	10,0	0,930	5,31	2,7	10,0	0,126	0,043	2,921
	10 degree	0,247	0,075	10,0	1,850	10,48	5,3	10,0	0,251	0,051	4,869
	15 degree	0,377	0,124	10,0	2,820	15,75	8,0	10,1	0,383	0,069	5,568
	20 degree	0,513	0,202	10,0	3,850	21,06	10,9	10,2	0,523	0,098	5,345
	25 degree	0,668	0,315	10,0	5,000	26,56	14,0	10,3	0,682	0,135	5,046
30 degree	0,853	0,495	10,0	6,410	32,66	17,8	10,5	0,874	0,191	4,565	

**Table B5.2:** Aerodynamic Performance for  $V=30\text{m/s}$ ,  $\sigma=1.5$

	The Coefficients in X-Y direction	Measuring section parameters			Mean Velocity Properties		Projection of the coefficients on mean velocity direction				
		Lift Coeff.	Drag Coeff.	Y velocity (m/s)	X velocity (m/s)	Velocity Direction (°)	Direction (°)	Magnitude (m/s)	Lift Coeff.	Drag Coeff.	L/D
Velocity=30 m/s	Angle of Attack										
	0 degree	0,000	0,031	30,0	0,013	0,02	0,0	30,0	0,000	0,031	0,000
	5 degree	0,121	0,039	30,0	2,730	5,20	2,6	30,0	0,122	0,033	3,666
	10 degree	0,242	0,065	30,0	5,450	10,30	5,2	30,1	0,245	0,042	5,763
	15 degree	0,366	0,112	30,0	8,230	15,34	7,8	30,3	0,371	0,060	6,171
	20 degree	0,497	0,188	30,0	11,170	20,42	10,5	30,5	0,505	0,091	5,572
	25 degree	0,640	0,297	30,0	14,400	25,64	13,5	30,9	0,654	0,132	4,960
30 degree	0,819	0,472	30,0	18,440	31,58	17,1	31,4	0,842	0,192	4,376	

**Table B5.3:** Aerodynamic Performance for  $V=50\text{m/s}$ ,  $\sigma=1.5$

	The Coefficients in X-Y direction	Measuring section parameters			Mean Velocity Properties		Projection of the coefficients on mean velocity direction				
		Lift Coeff.	Drag Coeff.	Y velocity (m/s)	X velocity (m/s)	Velocity Direction (°)	Direction (°)	Magnitude (m/s)	Lift Coeff.	Drag Coeff.	L/D
Velocity=50 m/s	Angle of Attack										
	0 degree	0,000	0,027	50,0	0,019	0,02	0,0	50,0	0,000	0,027	0,000
	5 degree	0,121	0,035	50,0	4,560	5,21	2,6	50,1	0,122	0,029	4,158
	10 degree	0,243	0,061	50,0	9,100	10,31	5,2	50,2	0,245	0,038	6,392
	15 degree	0,368	0,109	50,0	13,780	15,41	7,8	50,5	0,372	0,057	6,571
	20 degree	0,500	0,186	50,0	18,750	20,56	10,6	50,9	0,508	0,088	5,798
	25 degree	0,650	0,298	50,0	24,350	25,97	13,7	51,5	0,663	0,128	5,171
30 degree	0,832	0,475	50,0	31,510	32,22	17,5	52,4	0,852	0,185	4,612	

**Table B5.4:** Aerodynamic Performance for  $V=70\text{m/s}$ ,  $\sigma=1.5$

		The Coefficients in X-Y direction		Measuring section parameters			Mean Velocity Properties		Projection of the coefficients on mean velocity direction		
Velocity=70 m/s	Angle of Attack	Lift Coeff.	Drag Coeff.	Y velocity (m/s)	X velocity (m/s)	Velocity Direction (°)	Direction (°)	Magnitude (m/s)	Lift Coeff.	Drag Coeff.	L/D
	0 degree	0,000	0,024	70,0	0,037	0,03	0,0	70,0	0,000	0,024	0,000
	5 degree	0,121	0,033	70,0	6,410	5,23	2,6	70,1	0,122	0,027	4,461
	10 degree	0,244	0,059	70,0	12,840	10,39	5,2	70,3	0,246	0,036	6,810
	15 degree	0,372	0,107	70,0	19,500	15,57	7,9	70,7	0,376	0,054	7,011
	20 degree	0,501	0,183	70,0	26,260	20,56	10,6	71,2	0,508	0,085	6,013
	25 degree	0,638	0,288	70,0	33,450	25,54	13,4	72,0	0,650	0,125	5,214
	30 degree	0,819	0,469	70,0	43,540	31,88	17,3	73,3	0,840	0,187	4,503

**Table B5.5:** Aerodynamic Performance for  $V=100\text{m/s}$ ,  $\sigma=1.5$

		The Coefficients in X-Y direction		Measuring section parameters			Mean Velocity Properties		Projection of the coefficients on mean velocity direction		
Velocity=100 m/s	Angle of Attack	Lift Coeff.	Drag Coeff.	Y velocity (m/s)	X velocity (m/s)	Velocity Direction (°)	Direction (°)	Magnitude (m/s)	Lift Coeff.	Drag Coeff.	L/D
	0 degree	0,001	0,022	100,0	0,040	0,02	0,0	100,0	0,001	0,022	0,046
	5 degree	0,122	0,030	100,0	9,190	5,25	2,6	100,1	0,123	0,024	5,058
	10 degree	0,244	0,057	100,0	18,320	10,38	5,2	100,4	0,246	0,034	7,193
	15 degree	0,367	0,104	100,0	27,550	15,40	7,8	100,9	0,371	0,052	7,135
	20 degree	0,492	0,179	100,0	36,900	20,25	10,5	101,7	0,499	0,084	5,951
	25 degree	0,639	0,290	100,0	47,900	25,59	13,5	102,8	0,652	0,126	5,173
	30 degree	0,821	0,471	100,0	61,100	31,42	17,0	104,6	0,844	0,193	4,382

**B.6. Solidity  $\sigma=2$**

**Table B6.1:** Aerodynamic Performance for  $V=10\text{m/s}$ ,  $\sigma=2$

		The Coefficients in X-Y direction		Measuring section parameters			Mean Velocity Properties		Projection of the coefficients on mean velocity direction		
Velocity=10 m/s	Angle of Attack	Lift Coeff.	Drag Coeff.	Y velocity (m/s)	X velocity (m/s)	Velocity Direction (°)	Direction (°)	Magnitude (m/s)	Lift Coeff.	Drag Coeff.	L/D
	0 degree	0,000	0,044	10,0	0,000	0,00	0,0	10,0	0,000	0,044	0,000
	5 degree	0,098	0,050	10,0	0,975	5,57	2,8	10,0	0,100	0,045	2,209
	10 degree	0,197	0,072	10,0	1,980	11,20	5,7	10,0	0,201	0,052	3,888
	15 degree	0,297	0,111	10,0	2,970	16,54	8,4	10,1	0,303	0,065	4,686
	20 degree	0,408	0,171	10,0	4,080	22,20	11,5	10,2	0,417	0,083	5,046
	25 degree	0,522	0,266	10,0	5,220	27,56	14,6	10,3	0,536	0,118	4,558

**Table B6.2:** Aerodynamic Performance for V=30m/s,  $\sigma=2$

Velocity=30 m/s	Angle of Attack	The Coefficients in X-Y direction		Measuring section parameters			Mean Velocity Properties		Projection of the coefficients on mean velocity direction		
		Lift Coeff.	Drag Coeff.	Y velocity (m/s)	X velocity (m/s)	Velocity Direction (°)	Direction (°)	Magnitude (m/s)	Lift Coeff.	Drag Coeff.	L/D
	0 degree	0,000	0,033	30,0	0,000	0,00	0,0	30,0	0,000	0,033	0,000
	5 degree	0,094	0,039	30,0	2,810	5,35	2,7	30,0	0,095	0,035	2,737
	10 degree	0,188	0,059	30,0	5,640	10,65	5,4	30,1	0,191	0,041	4,683
	15 degree	0,284	0,097	30,0	8,520	15,85	8,1	30,3	0,289	0,055	5,254
	20 degree	0,387	0,152	30,0	11,600	21,14	10,9	30,6	0,394	0,073	5,395
	25 degree	0,499	0,245	30,0	14,980	26,53	14,0	30,9	0,512	0,110	4,652

**Table B6.3:** Aerodynamic Performance for V=50m/s,  $\sigma=2$

Velocity=50 m/s	Angle of Attack	The Coefficients in X-Y direction		Measuring section parameters			Mean Velocity Properties		Projection of the coefficients on mean velocity direction		
		Lift Coeff.	Drag Coeff.	Y velocity (m/s)	X velocity (m/s)	Velocity Direction (°)	Direction (°)	Magnitude (m/s)	Lift Coeff.	Drag Coeff.	L/D
	0 degree	0,000	0,029	50,0	0,000	0,00	0,0	50,0	0,000	0,029	0,000
	5 degree	0,093	0,035	50,0	4,680	5,35	2,7	50,1	0,094	0,031	3,088
	10 degree	0,188	0,055	50,0	9,390	10,64	5,4	50,2	0,191	0,037	5,172
	15 degree	0,285	0,093	50,0	14,230	15,89	8,1	50,5	0,289	0,051	5,687
	20 degree	0,389	0,149	50,0	19,500	21,31	11,0	50,9	0,395	0,069	5,715
	25 degree	0,506	0,245	50,0	25,320	26,86	14,2	51,6	0,517	0,106	4,860

**Table B6.4:** Aerodynamic Performance for V=70m/s,  $\sigma=2$

Velocity=70 m/s	Angle of Attack	The Coefficients in X-Y direction		Measuring section parameters			Mean Velocity Properties		Projection of the coefficients on mean velocity direction		
		Lift Coeff.	Drag Coeff.	Y velocity (m/s)	X velocity (m/s)	Velocity Direction (°)	Direction (°)	Magnitude (m/s)	Lift Coeff.	Drag Coeff.	L/D
	0 degree	0,000	0,025	70,0	0,000	0,00	0,0	70,0	0,000	0,025	0,000
	5 degree	0,094	0,032	70,0	6,600	5,39	2,7	70,1	0,095	0,027	3,464
	10 degree	0,190	0,052	70,0	13,340	10,79	5,4	70,3	0,192	0,033	5,752
	15 degree	0,288	0,091	70,0	20,150	16,06	8,2	70,7	0,292	0,048	6,077
	20 degree	0,394	0,148	70,0	27,560	21,49	11,1	71,3	0,400	0,067	6,007
	25 degree	0,504	0,239	70,0	35,260	26,73	14,1	72,2	0,514	0,102	5,035

**Table B6.5:** Aerodynamic Performance for  $V=100\text{m/s}$ ,  $\sigma=2$

	The Coefficients in X-Y direction	Measuring section parameters			Mean Velocity Properties		Projection of the coefficients on mean velocity direction				
		Lift Coeff.	Drag Coeff.	Y velocity (m/s)	X velocity (m/s)	Velocity Direction (°)	Direction (°)	Magnitude (m/s)	Lift Coeff.	Drag Coeff.	L/D
Velocity=100 m/s	0 degree	0,000	0,023	100,0	0,028	0,02	0,0	100,0	0,000	0,023	0,000
	5 degree	0,094	0,030	100,0	9,380	5,36	2,7	100,1	0,095	0,025	3,787
	10 degree	0,190	0,050	100,0	19,030	10,77	5,4	100,5	0,192	0,031	6,101
	15 degree	0,285	0,088	100,0	28,620	15,97	8,1	101,0	0,289	0,046	6,303
	20 degree	0,388	0,143	100,0	38,810	21,21	11,0	101,9	0,393	0,064	6,140
	25 degree	0,499	0,237	100,0	49,900	26,52	14,0	103,1	0,510	0,103	4,961